HOT DEFORMATION OF ALUMINUM-COPPER-MAGNESIUM POWDER METALLURGY ALLOYS

by

Ryan E.D. Mann

Submitted in partial fulfilment of the requirements
for the degree of Master of Applied Science

at

Dalhousie University
Halifax, Nova Scotia
December 2010

DALHOUSIE UNIVERSITY

DEPARTMENT OF PROCESS ENGINEERING AND APPLIED SCIENCE

The undersigned hereby certify that they have read and recommend to the Faculty of Graduate Studies for acceptance a thesis entitled "HOT DEFORMATION OF ALUMINUM-COPPER-MAGNESIUM POWDER METALLURGY ALLOYS" by Ryan E.D. Mann in partial fulfillment of the requirements for the degree of Master of Applied Science.

Dated: 3, December, 2010

Supervisor: _____

Readers: _____

_____

_____

DALHOUSIE UNIVERSITY

DATE: December 3, 2010

AUTHOR: Ryan E.D. Mann

TITLE: HOT DEFORMATION OF ALUMINUM-COPPER-MAGNESIUM POWDER METALLURGY ALLOYS

DEPARTMENT OR SCHOOL: DEPARTMENT OF PROCESS ENGINEERING AND APPLIED SCIENCE

DEGREE: MASc CONVOCATION: May YEAR: 2011

_____

Signature of Author

Table of Contents

List of Tables

List of Figures

Abstract

The implementation of technologies such as aluminum powder metallurgy (P/M) can be used in the automobile industry to have potential economic and environmental advantages. This technology to produce vehicle components can offer the combination of weight savings due to the low density of aluminum and material and machining savings via near net shape processing attributes. In an effort to expand the scope of application for aluminum P/M, considerable research has emphasized the development of new alloys and composites. One such alloy is P/M 2324, an aluminum-copper-magnesium alloy developed to have increased mechanical properties over the standard aluminum P/M alloys of the AC2014 type.

The objective of this work was to undertake a comprehensive study on the effects of hot deformation on the emerging alloy P/M 2324 as well as the alloy with a SiC addition. Here, a forgeability study of these alloys and its wrought counterpart AA2024 was completed. To do so, peak flow stress data were acquired under different combinations of temperature and strain rate using a thermal-mechanical test frame. The Zener-Hollomon relationship was then used to model the peak flow stress behaviour of the two alloys. Finally, the impact of hot work in mechanical properties was quantified through hot swaging trials. The microstructures of the alloys in the various states were also qualified and compared using a variety of techniques.

It was confirmed that full density could be achieved in P/M 2324 by hot deformation at all of the strain rates and temperatures considered. However, P/M 2324 + 5 v/o SiC achieved a density of 2.77 g/cc, corresponding to 99.0% the full theoretical density of the alloy. Peak flow stress modelling of the P/M and wrought alloys yielded similar results, both adhering to a standard Zener-Hollomon curve fitting approach. The peak stress observed was found to increase with rising strain rate but decrease with rising temperature. Mechanical testing yielded improvements in all properties from the sintered to the sintered and swaged condition of the P/M alloys with a ~25% increase in UTS and YS and 3-fold increase in elongation. The YS and UTS of swaged P/M 2324 +5% SiC were higher than that of P/M 2324 although the elongation was inferior. The P/M alloys exhibited greater tensile strength and reduced ductility over the wrought alloy. The microstructure of P/M 2324 was quite similar to that of P/M 2324+5v/o SiC except for the presence of SiC, however they differed from the wrought AA2024. The major secondary phase in the P/M alloy was the precipitation hardening θ phase (Al_2Cu), while the major precipitation hardening phase in the wrought alloy was the S phase (Al_2MgCu). The wrought alloy also has a constituent phase Al_7Cu_2Fe with some iron replaced with manganese ($Al_7Cu_2(Fe,Mn)$).

List of Abbreviations and Symbols Used

$\dot{\varepsilon}$ = Strain rate (s^{-1}).

σ = Peak flow stress (MPa).

α = Stress multiplier (MPa^{-1}).

Q = Activation energy of deformation (kJ mol^{-1}).

R = Ideal gas constant (kJ mol^{-1} K^{-1}).

T = Deformation temperature (K).

Z = The Zener-Hollomon parameter.

A, n, s = Material constant.

Acknowledgements

The authors would like to acknowledge the technical support provided by Mr. Winston Mosher, Mr. Chris Boland, Mr. Dave Walker, and Mr. Dean Grijim. The Natural Sciences and Engineering Research Council of Canada (NSERC) is gratefully thanked for the provision of funding support via Strategic Grant 350505-07. Dr. Burnhard Mais and Mr. Johann Gradl at ECKA Granules are also thanked for the provision of all of the metal powders utilized.

Chapter 1.0 Introduction

Sintered aluminum P/M alloys are an attractive material for the automobile industry, given the low specific gravity and high strength/weight ratio of aluminum itself as well as fabrication advantages associated with the P/M process. For example, aluminum P/M is often used to produce the camshaft bearing caps or “cam caps” found in combustion engines. Such components, historically produced by die casting, are precision parts as they ensure proper alignment of a camshaft when bolted to the block. Die cast cam caps do not meet the required dimensional tolerances and must be heavily machined prior to use. Conversely, P/M production methods offer tighter dimensional tolerances to avoid the majority of expensive machining operations.

In an effort to expand the scope of application for aluminum P/M, considerable research has emphasized the development of new alloys and composites. In one of the more recent programs, Boland et. al. have devised a P/M equivalent to wrought 2324 [1]. P/M 2324 is an aluminum-copper-magnesium alloy developed to have increased mechanical properties over the standard aluminum P/M alloys of the AC2014 type. The improvement of P/M 2324 comes from the ability to achieve an exceptionally high sinter density and the formation of S-type intermetallic precipitates [2].

With regards to composites, the use of aluminum based metal matrix composites (MMCs) is increasing in automotive and aerospace applications due to their high specific strength, stiffness and high hardness. The combination of weight reduction and improved properties can result in lower fuel consumption, reduced emissions and improved performance with the use of these materials [3].

Although the newer alloys offer major strength improvements, the presence of a small amount of residual porosity in the sintered product remains as a hurdle to overcome. In ferrous products, this feature can be eliminated by forging the as-sintered materials [4]. This is known to increase all mechanical properties significantly with the most prominent gains realized in yield strength, ductility, and fatigue life. P/M forging is now a widely used method of producing steel parts of high density for the automotive industry [5]. However, it remains an unexploited technology in the production of aluminum components.

Chapter 2.0 Research Objectives

The objective of this work was to undertake a comprehensive study on the effects of hot deformation on the emerging alloy P/M 2324. Here, a forgeability study of it and its wrought counterpart AA2024 was completed. To do so, peak flow stress data were acquired under different combinations of temperature and strain rate using a thermal-mechanical test frame. The Zener-Hollomon relationship was then used to model the peak flow stress behaviour of the two alloys. Finally, the impact of hot work in mechanical properties was quantified through hot swaging trials. The same tests were then completed to assess the effects of a five volume percent silicon carbide addition on the P/M alloy. The microstructures of the alloys in the various states were also qualified and compared using a variety of techniques.

Chapter 3.0 Fundamentals of Powder Metallurgy

3.1 Powder Production: Atomization

In all powder fabrication techniques, energy is consumed to create surface area. Most powder techniques are low in efficiency as they require more energy to form the powder than the newly generated surface energy. Some of the main metal powder generation techniques include mechanical comminution, chemical reactions, electrolytic deposition, atomization, and vapour condensation. Common Aluminum powder production techniques include, air atomization, gas atomization, and milling [6].

Atomization is the disintegration of a melt into droplets that freeze into particles. The three principal types of atomization include gas atomization, water atomization, and centrifugal atomization [6]. Gas atomization is the use of air, nitrogen, helium, or argon gas to break up a molten stream. In this technique the liquid metal is disintegrated by rapid gas expansion out of a nozzle. The formation of metal powder by gas atomization involves the break-up of the liquid stream by the rapidly expanding gas. The metal stream first forms into a thin hollow sheet, then ligaments, ellipsoids, and eventually, spheres as shown in Figure 1. The size and shape of the resulting powder is determined by the temperatures of the gas and melt, the type of gas employed, the angle in which the gas contacts the melt, and the velocity of the gas and melt.

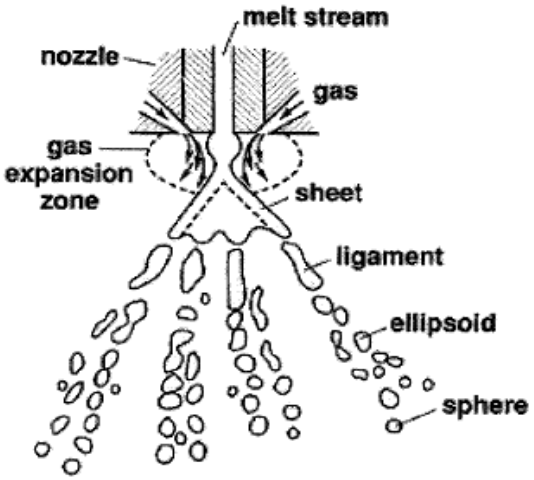

Figure 1 – Schematic of a typical air atomization process [7].

Water atomization uses high pressure jets directed against the melt stream, forcing disintegration and rapid solidification. Water atomization is the most common technique for producing elemental and alloy powders from metals which melt below approximately 1600°C provided that no hazardous reactions are apt to occur [6]. A typical water atomization process is shown Figure 2 where a molten metal stream is disintegrated by multiple water jets at an angle α which determines the atomization efficiency.

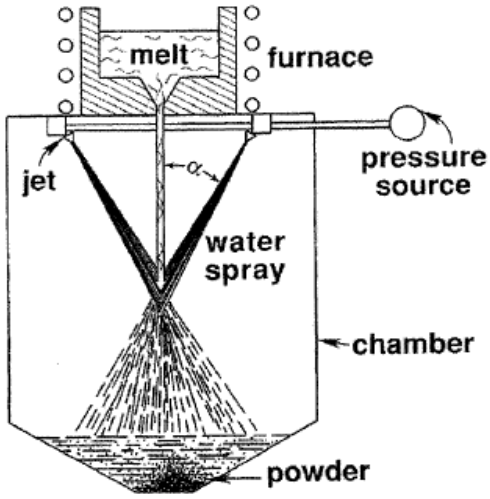

Figure 2 – Schematic of a typical water atomization apparatus [7].

There are four common particle generation mechanisms associated with water atomization as demonstrated in Figure 3 [6]. The first is cratering, where a water droplet impacts the melt and causes a melt droplet to project away from the melt. Splashing is the projecting of small melt droplets from the melt stream after water droplets hit the melt. Stripping is the projection of a water droplet onto an uneven section of a melt, stripping a portion of the melt into a droplet. Bursting is the action associated with a water droplet hitting a melt droplet, prompting it to burst into a multitude of smaller melt droplets.

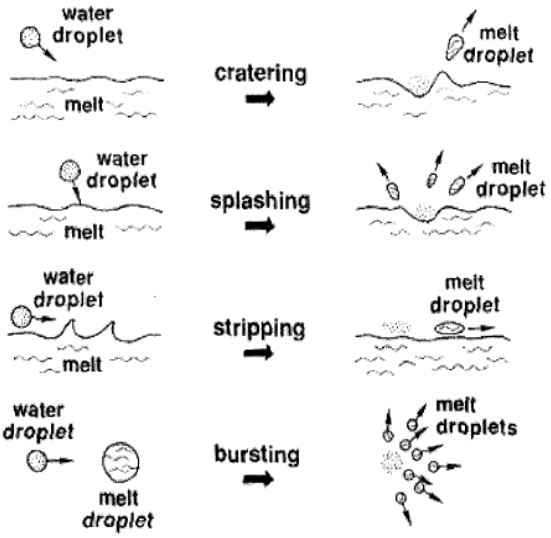

Figure 3 – Powder production mechanisms typically found in water atomization [6].

Another form of atomization is centrifugal atomization, this technique relies on mechanical force realized by spinning the melt to form droplets that solidify into particles. Centrifugal atomization is a very useful when dealing with high-temperature or reactive materials where contact with a crucible is a difficulty [6]. Many variations of this technology exist, such as the rotating electrode process, disk, cup, wheel, and mesh atomization. The rotating electrode process is shown in Figure 4.

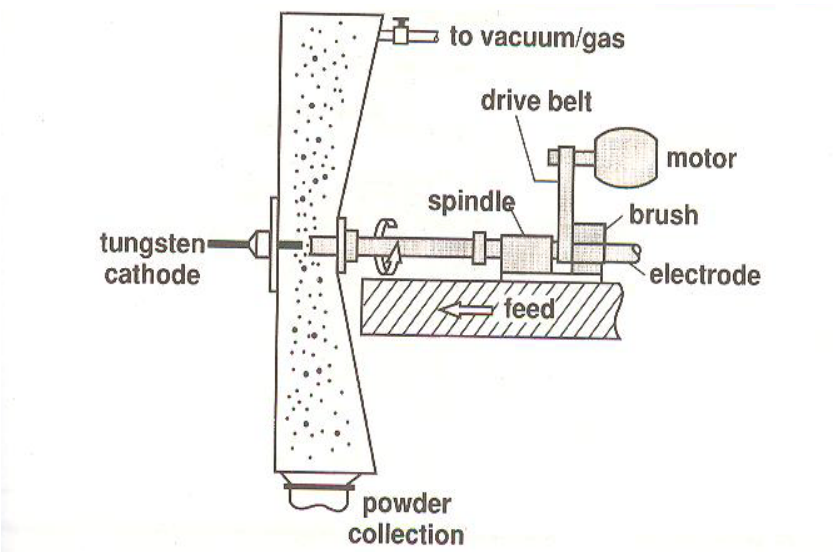

Figure 4 – Schematic of a typical rotating electrode centrifugal atomization apparatus [6].

The rotating electrode process uses an electrode of the desired material which is rotated by an external motor. The electrode is melted at one end by an electrical arc created between it and a tungsten cathode. The centrifugal force from rotation then causes the melt to be thrown off as droplets that solidify into powder. A sketch of the liquid film break-up and formation into spherical particles is shown in Figure 5 [6].

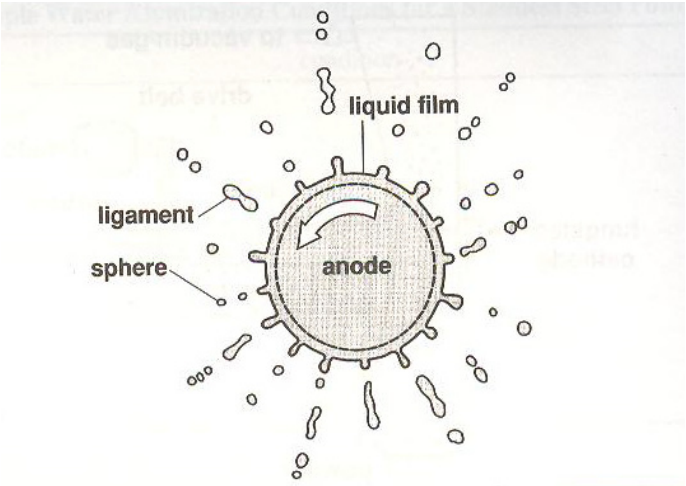

Figure 5 – Schematic of the liquid film break-up from a rotating electrode atomization apparatus [6].

There are several other forms of centrifugal atomization as shown in Figure 6 [6]. These methods rely on a melt being directed onto a spinning disk, cup, wheel, or mesh, where the centrifugal force throws the melt outward causing it to disintegrate into droplets that eventually solidify into powder particles.

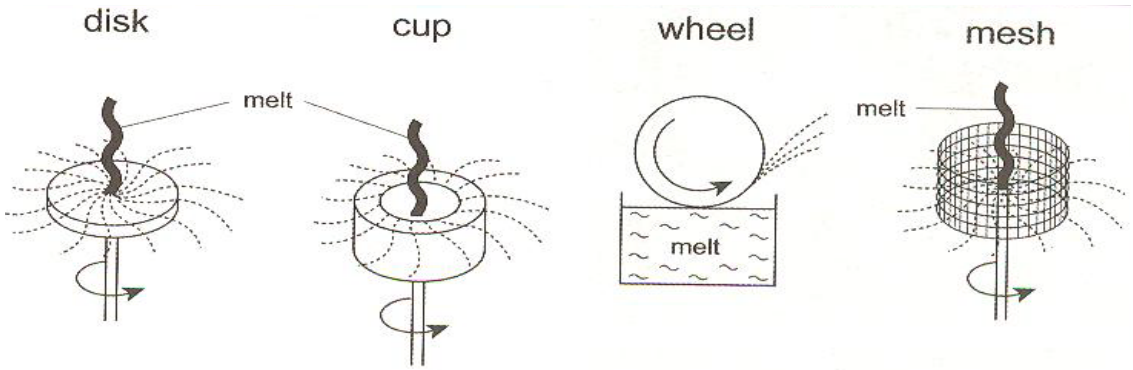

Figure 6 – Schematics of various centrifugal atomization methods [6].

Overall, there are a variety of atomization techniques used to form metal powders. The technique employed in a given production scenario is determined by the metal, the desired particle size, shape, and size distribution as well as cost. A summary of these attributes for several of the more common production techniques is given in Table I.

Table I – Comparison of various atomization techniques [6].

Process	Range, µm	Particle shape	Distribution	Cost
Rotating electrode	200-600	spherical	Bimodal	High
Water atomization	5-800	Irregular, nodular	Wide	Low
Gas atomization	15-300	spherical	Moderate	Moderate

3.2 Powder Blending

Blending is necessary to prepare unique particle size distributions, combine powders to generate new alloys, add lubricants for compaction, and to prepare a powder-binder mixture for shaping. In P/M, blending is principally done to mix all of the alloying constituents to achieve a homogeneous composition and alleviate segregation in pre-mixed blends. Failure to do so could result in pour results in the final product.

3.2.1 Segregation

Segregation is defined as a de-mixing of particles due to differences in physical or mechanical properties [7]. Factors such as particle size, weight, density, surface texture, inter-particle forces of attraction, etc. can lead to varying degrees of particle segregation. Mechanisms of segregation include percolation, surface effect segregation, and air current segregation.

Percolation is known as the preferential movement of small particles past larger particles. The severity of the problem is determined by the particle size range within the overall powder mass. The presence of percolation is often manifested as fines enrichment in the discharge stream when draining down the last of the inventory within a core flow vessel [8]. Figure 7 shows the separation of the particles by size during vibration.

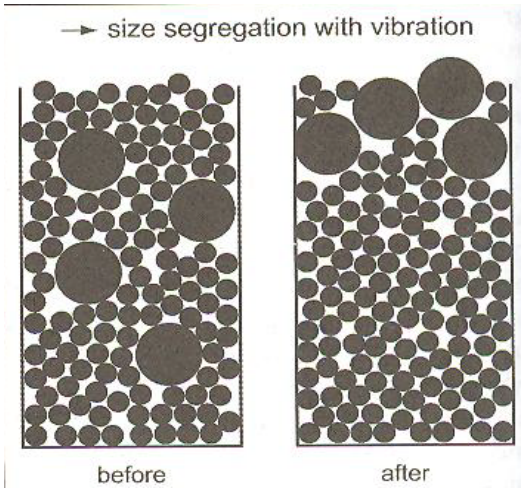

Figure 7 – Schematic of vibration induced segregation with larger particles moving to the top [7].

Surface effect segregation is caused by the difference in the inertia of particles. When particles of a bulk solid are in contact with a surface, finer and irregular shaped particles develop more frictional force than larger particles [8]. Such particles tend to decelerate or become immobile more rapidly than the larger, smoother, and consequently, more free-flowing particles. Air current segregation occurs as fine particles typically exhibit lower settling velocities than larger particles, and will not only remain suspended in air longer, but are also more susceptible to re-entrainment in the presence of air flows [8]. Larger particles tend to settle more rapidly, leading to coarse enrichment in the lower or more quickly filled regions of the vessel/equipment while the upper regions exhibit fines enrichment.

The Degree of segregation can be calculated by Equation 1 [7] where C_S is the segregation coefficient, X_T is the fraction of large particles in the top half of the container and X_B is the fraction of large particles in the bottom half of the container.

$$C_S = \frac{X_T - X_B}{X_T + X_B} \qquad \textbf{Equation 1}$$

3.2.2 Blending of Dry Powders

When dry powders are blended into a homogeneous mixture, three modes of powder mixing can transpire. These include, diffusion, convection, and shear as demonstrated in Figure 8 [7]. Diffusion is the motion of individual powders within a powder lot, which is demonstrated in a rotating drum. Convection is the transfer of adjacent powder groups from one location to another, which occurs in a screw mixer. Shear is the continual division and flow of the powder over slip planes, which is the predominant mechanism in a blade mixer.

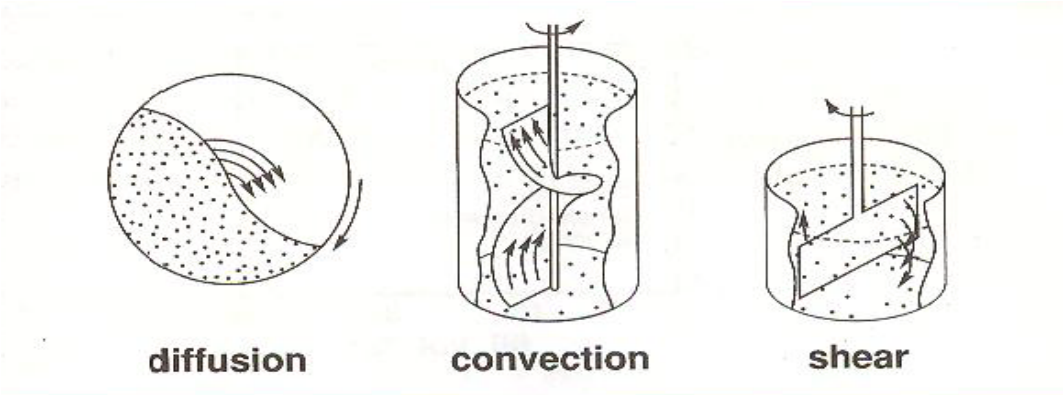

Figure 8 – Schematic of three blending mechanisms; diffusion, convection, and shear [7].

Typically, optimal mixing occurs when the centrifugal forces are small, but not so small that turbulence does not occur [6]. The optimal rotational speed N_O is calculated as per Equation 2, where the gravitational and centrifugal forces are balanced, and where d is the outer arc distance of the container.

$$N_O = \frac{32}{\sqrt{d}} \qquad \textbf{Equation 2}$$

3.2.3 Blending with Binders and Lubricants

Binders are used in processes such as die compaction, injection molding, tape casting, and slip casting. Binders provide strength to the green body whereas lubricants help to reduce die wall friction during powder compaction [6]. In P/M, waxes are used for lubrication as they are inexpensive and can be removed via thermal pyrolysis. For aluminum sinter mixes, Licowax C is commonly added in the range of 0.5 – 2.0 w/o so as to reduce friction between the powder and the forming tool and to ease ejection of the powder compact from the die. They are also used to extend tool life and to prevent powder blends from cold welding to the metal dies during compaction [6].

The common mixers for dry powders are generally not useful in the preparation of powder-binder mixtures. Here, high shear is required to cause molecular scale dispersion of binder between the particles [7]. Two geometries of batch mixers used to combine binders with powder are double planetary and sigma-blade (Figure 9).

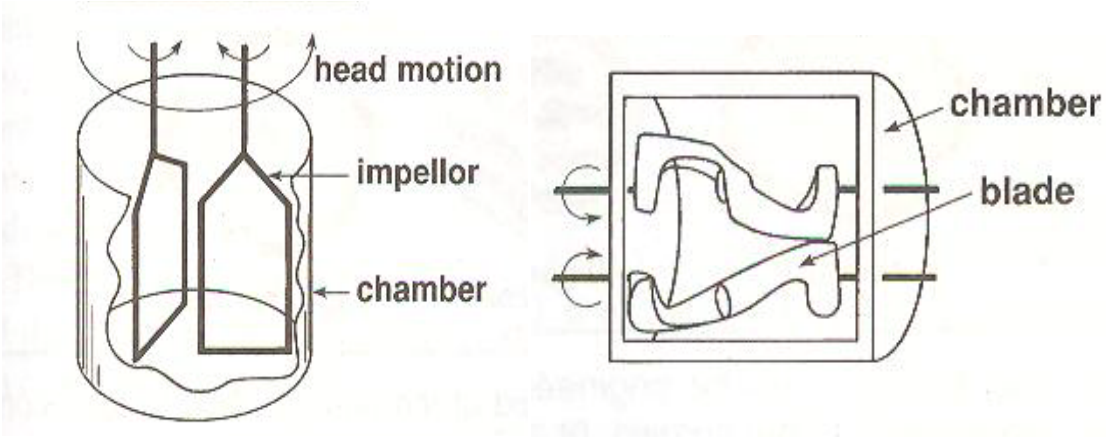

Figure 9 – Double planetary and sigma-blade mixers geometries used to mix binders with powders [7].

3.3 Powder Compaction

In most P/M applications, it is desired to produce components with high densities. To achieve this goal, the compaction of powders to high green densities is typically required. This can be accomplished by several means including isostatic compaction and die compaction. Isostatic compaction can either be done hot or cold. This technique, as described in Figure 10, uses a flexible die, with isotropic pressurization to evenly distribute density within the sample. Vacuum degassing of the container is an important step to ensure densification of the workpiece [7].

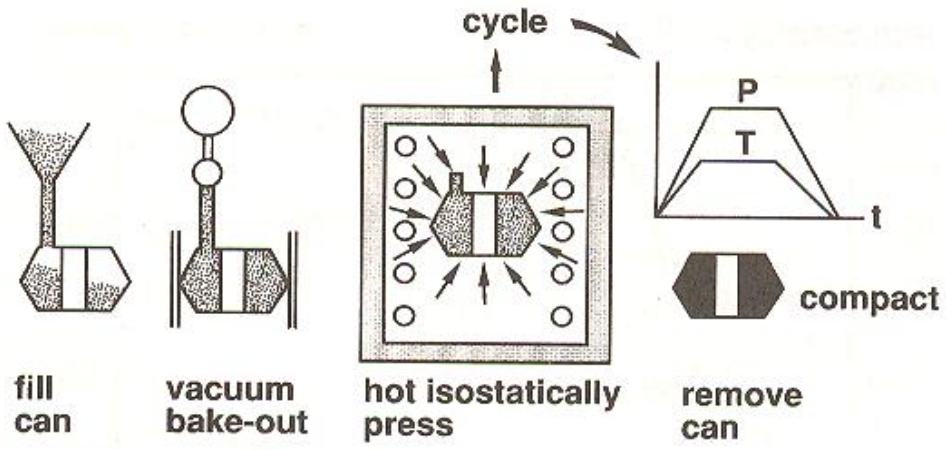

Figure 10 – Typical hot isostatic compression process [7].

Die compaction is the preferred method of compacting metal powder in high volume production scenarios. It involves the loading of powder into a hard die and uni-axially pressing. There are three main types of die compaction; single action, double action, and floating die [6]. Single action pressing is when pressure is transmitted from one punch (i.e. one direction only). Double action pressing is when pressure is simultaneously transmitted from both bottom and top punches. Floating die is one where the relative punch and die motions are such that both punches work against the die center simultaneously. A typical uni-axial die compaction cycle is shown in Figure 11.

As metal powders are compacted, four key stages transpire – rearrangement, localized deformation, homogeneous deformation, and bulk compression [9]. These concepts are illustrated in Figure 12. The rearrangement phase refers to the movement of powder particles to fill the larger voids. This is then followed by localized deformation wherein simple point contacts between particles deform into flattened surfaces. Homogeneous deformation is where the pores begin to collapse and the powders are work hardened. The final stage is bulk compression. Here, powders are heavily work hardened and effectively act as a solid, incompressible body. Figure 13 shows the different stages in compaction related to compaction

pressure and green density attained [7]. The amount of extra energy required to attain a small density increase from the fourth stage is generally deemed unnecessary for industrial operations.

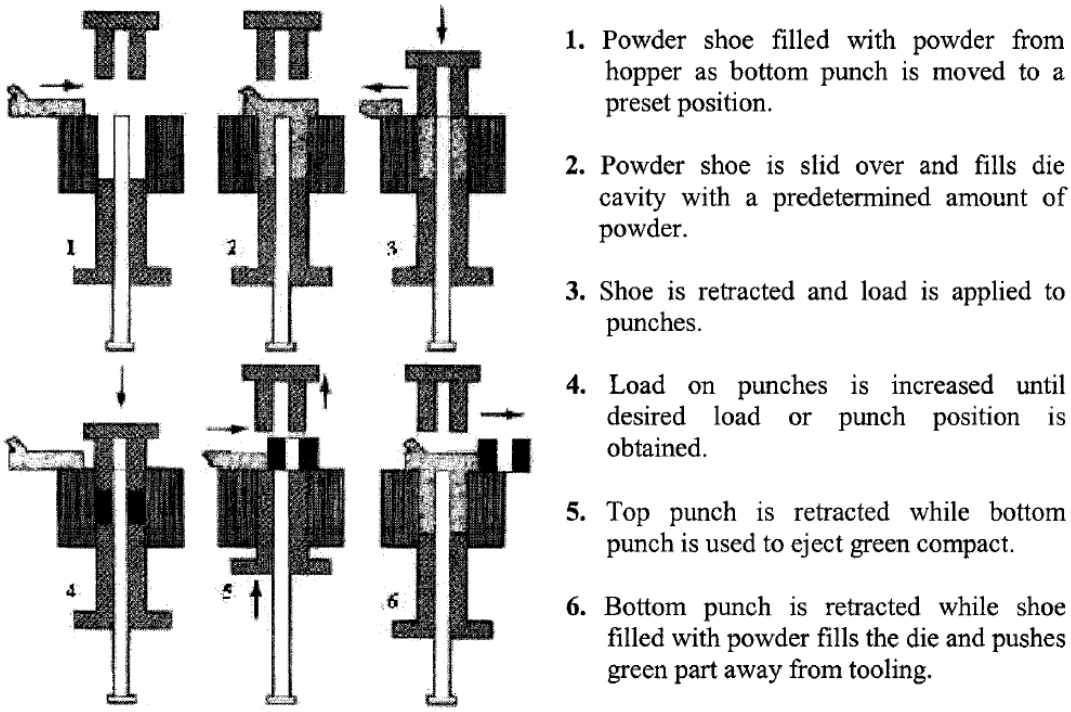

Figure 11 – Typical die compaction process [10].

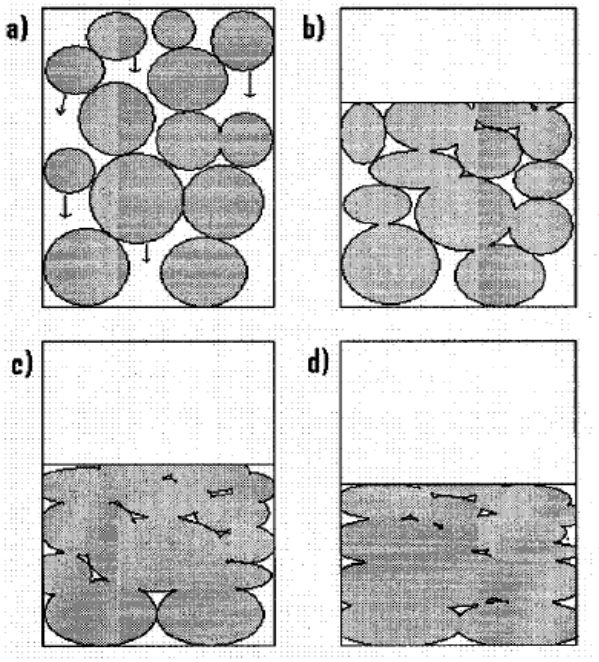

Figure 12 – Compaction stages in die compaction, a) rearrangement, b) localized deformation, c) homogeneous deformation, d) bulk compression [7].

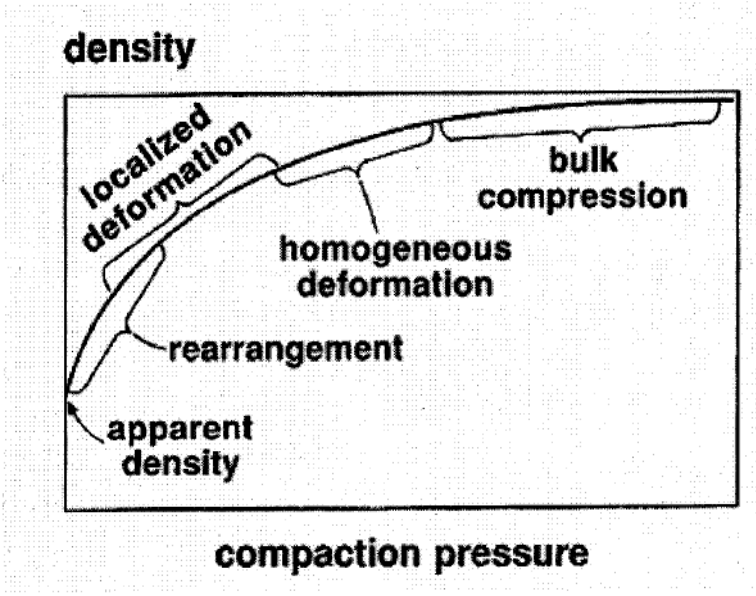

Figure 13 – Conceptual relationship between the stages of powder compaction and a typical compressibility curve [7].

3.3.1 Die wall friction

The largest concern with uni-axial die compression is the presence of die wall friction. This phenomenon can cause density gradients within the sample and inhibit compact ejection [6]. With regards to the former, powders close to the punch experience denser compaction, while powders far from the punch will remain less affected. The pressure decay with distance is because the powder spreads the load to the die wall in the form of friction. Such density gradients in samples can be a problem as they will produce sections in the sample with different sintered densities, and in turn mechanical properties than others. To minimize this problem, lubricants are used. The effect of die wall friction on the density gradients is shown in Figure 14 for both single action and double action uni-axial pressed powders.

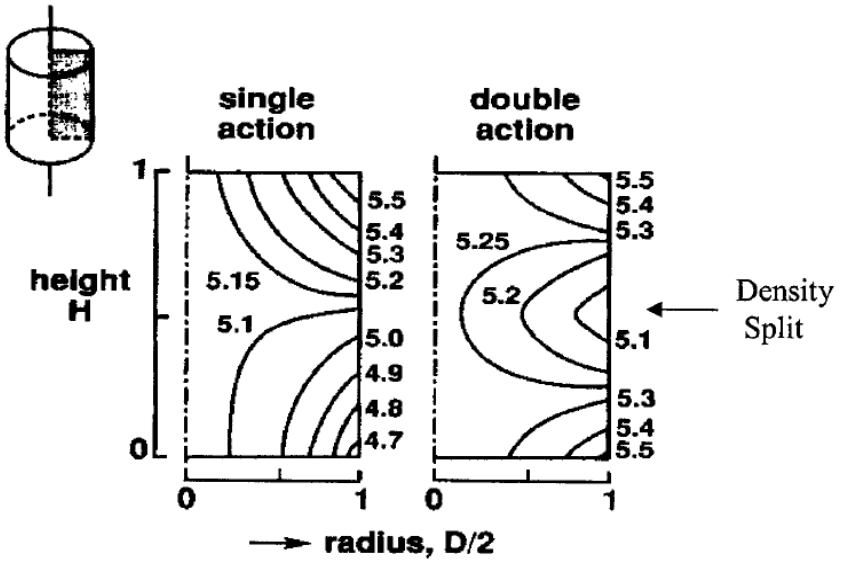

Figure 14 – Density gradients observed in single action and double action die compaction [7].

3.3.2 Compaction of Aluminum P/M alloys

The compressibility of aluminum P/M alloys is generally acceptable for uni-axial die compaction as a broad range of densities and strengths can be achieved during this stage. Figure 15 shows data on the green density and green strength of three commercial variants of the aluminum

P/M alloy AC2014 [11]. It is noted the densities in excess of 90% of theoretical and strengths >8MPa are readily achieved.

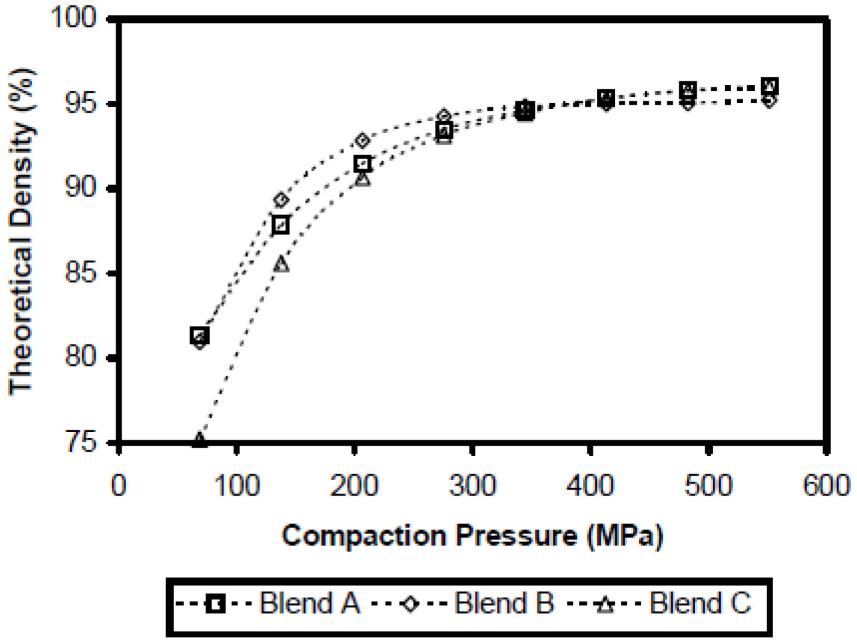

(a)

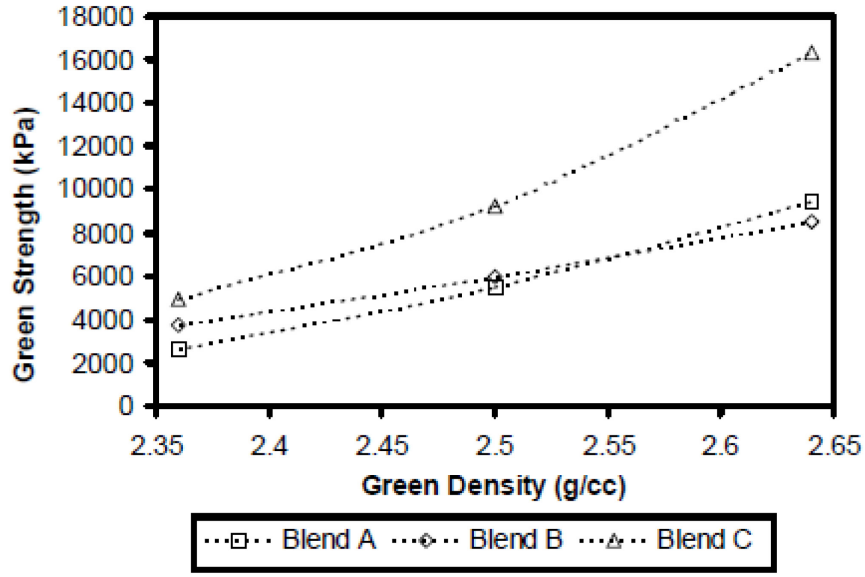

(b)

Figure 15 – General compaction attributes of three commercial variants of AC2014. (a) Green density and (b) green strength as functions of compaction pressure [11].

3.4 Sintering

Once powders are compacted, they are then sintered to enhance mechanical properties. Sintering involves the heating of green compacts to temperatures that are typically at or above half the melting point of the material [6]. Green compacts have a high energy state given the massive amount of surface area. As such, the system will attempt to lower its surface energy by mass transport on the atomic level when sintered. Sintering itself is defined as a thermal treatment for bonding particles into a coherent, predominantly solid structure via mass transport events that occur at the atomic level. Such bonding leads to improved strength and lower system energy [7]. The two main types of pressureless sintering processes are solid-state and liquid phase sintering. As aluminum P/M alloys are sintered exclusively through the latter approach, this will be the only method described.

3.4.1 Liquid Phase Sintering

Liquid phase sintering (LPS) is sintering in the presence of a small amount of a liquid phase. The quantity is controlled by temperature and alloy composition. Diffusion rates (mass transport) are much faster in a liquid than a solid, therefore LPS is used to produce dense materials from powders with desirable mechanical properties in a much shorter amount of time than solid state sintering. Figure 16 shows a phase diagram of a typical composition and temperature where LPS would occur. As shown in the diagram, the alloy would be sintered in a region where solid and liquid phases would co-exist.

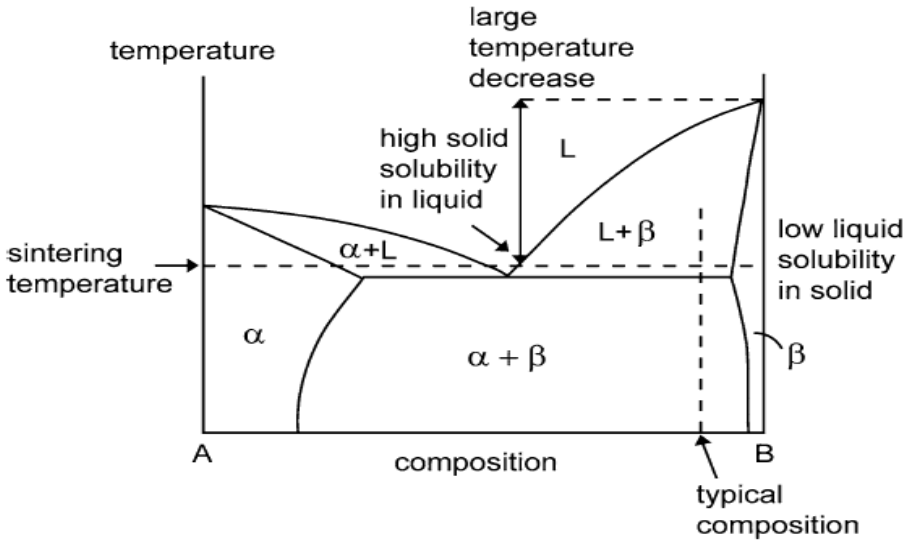

Figure 16 – Phase diagram demonstrating a composition and temperature where LPS would occur [12].

During LPS, the material is consolidated through four stages as illustrated in Figure 17 [12]. The first stage is the heating of the initially mixed and compacted powders. This is when the grains bond slightly by solid-state sintering at the contact points between the powders. Next is the rearrangement stage where the liquid first forms. The liquid is drawn into the inter-particle regions through capillary action. This allows the particles to rearrange by slipping past each other, resulting in rapid densification. The next stage is solution re-precipitation, where small grains dissolve in the liquid and re-precipitate on larger grains. This stage results in grain growth through the mass transport in the liquid phase. The material then experiences final stage sintering, where the compact attains a condition of solid contacting grains. This final stage is essentially a solid-state sintering situation.

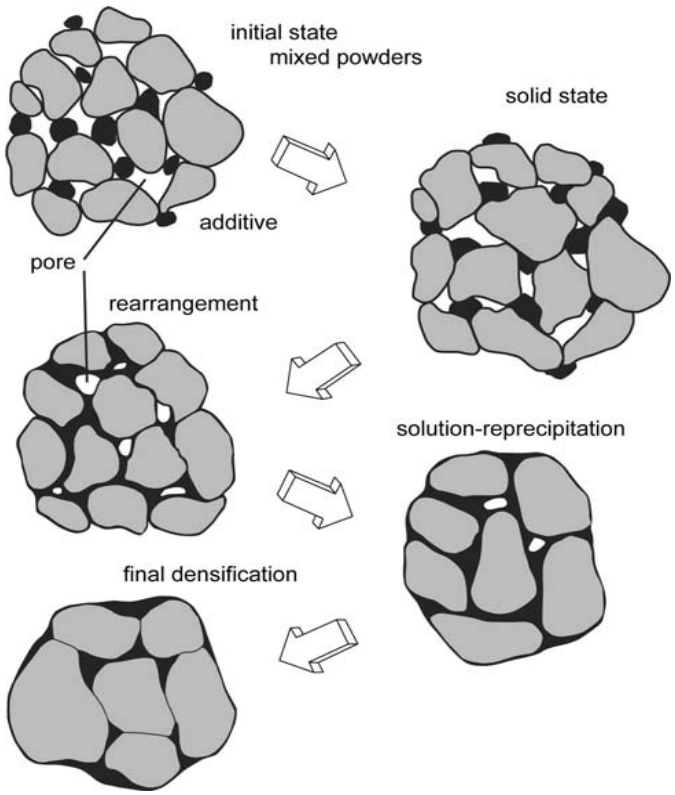

Figure 17 – Schematic demonstrating the mechanisms of liquid phase sintering [12].

Two of the key requirements for LPS to occur are to have high solubility of solid in liquid and low solubility of liquid in solid [12]. In a system with low liquid solubility in the solid and low solid solubility in the liquid, there will be densification limited to rearrangement. Conversely, in one with high liquid solubility in the solid and low solid solubility in the liquid, then there will be swelling in the material due to the highly transient nature of the liquid being absorbed in the solid. Finally, a system with high solid solubility in the liquid and a high liquid solubility in the solid will exhibit a mixed effect with both swelling and densification occurring at the same time.

Another important factor in LPS is the wetting of the liquid on the solid grains. Wetting is the ability of a liquid to spread over a solid. The contact angle must be less than 90° for wetting to occur, although a contact angle of less than 45° will result in good wetting (Figure 18) [12]. With good wetting, a capillary force is applied on the solid grains pulling them together so as to invoke rapid densification of the material.

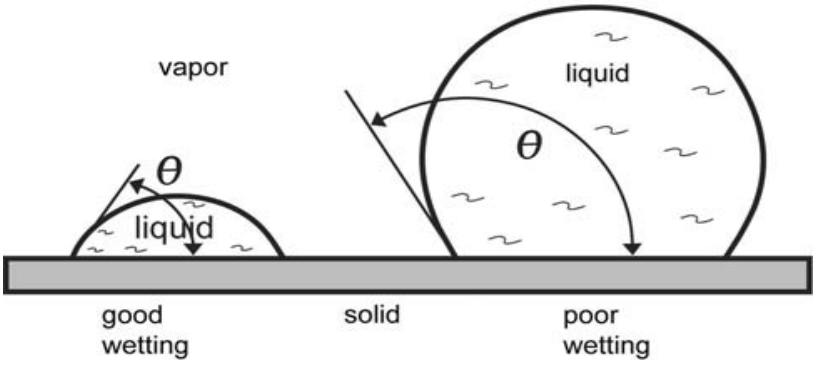

Figure 18 – Diagram showing wetting with respect to the contact angle [12].

Different types of LPS include supersolidus and transient sintering [6]. Supersolidus LPS relies on pre-alloyed powders instead of mixed powders. The type of sintering involves the heating of the alloyed powders to a temperature between the liquidus and solidus to nucleate a liquid within each particle. The semisolid particles become soft and densify rapidly by capillary induced rearrangement. Transient LPS is where the liquid is totally soluble in the solid. During heating, a liquid forms and then disappears over time as it forms an alloy. This type of sintering is sensitive to process conditions as swelling can occur due to the liquid alloying with the solid before rearrangement of the solid particles transpires.

3.4.2 Sintering with an Oxide Film

Aluminum powder is always covered by an oxide film formed during the atomization process. The thickness of this layer is dependent on the temperature at which it was formed and the atmosphere in which it is stored, particularly the humidity. This film can be problematic from a sintering standpoint due to its refractory nature and high thermodynamic stability. However, trace additions of magnesium are known to be an effective means of mitigating this problem. Magnesium is highly reactive and the free energy of formation of its oxide is more negative than that of the oxides of aluminum. Magnesium therefore has the potential reduce the oxide layer and form a spinel as shown in Equation 3 [13].

$$3\,Mg + 4Al_2O_3 \leftrightarrow 3MgAl_2O_4 + 2Al \qquad \textbf{Equation 3}$$

This reaction prompts an appreciable volume change. This creates a shear stress which breaks up the oxide layer ultimately allowing diffusion, wetting and sintering to take place on the surface of the aluminum powders [13].

3.4.3 Industrial Sintering

Laboratory sintering practices are generally done in a batch operation, although this is typically not economical for high volume industrial scale sintering. For this reason, sintering is preferably completed on a continuous basis using mesh belt furnaces. A schematic illustration of one such furnace is shown in Figure 19 with the time temperature graph below [6]. The sketch shows the preheat zone where delubrication of the compacts occurs. The compacts then move into the hot zone where sintering is completed for the required time period. The sintered materials are then brought through a cooling process and (in some cases) heat treatment before exiting the furnace.

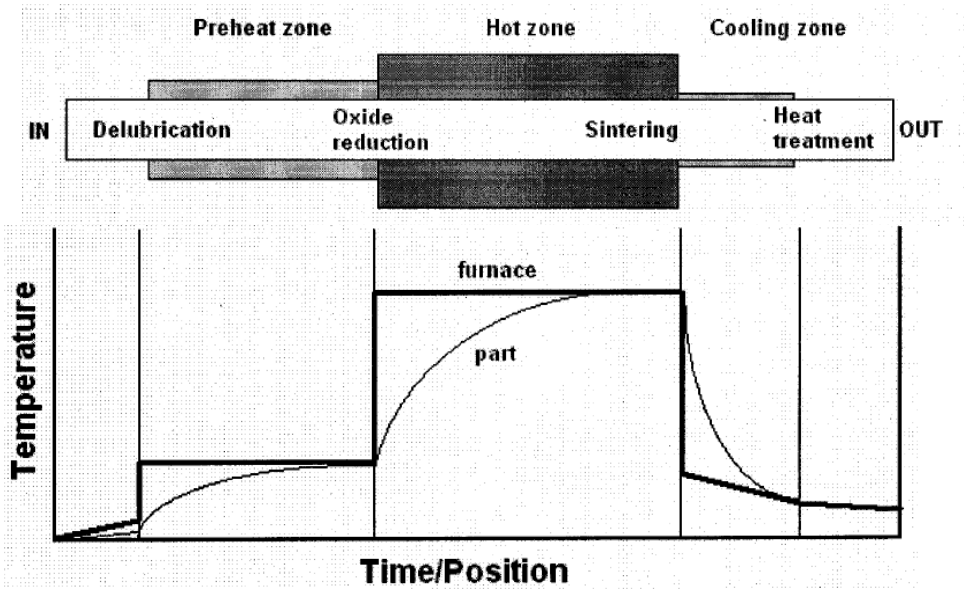

Figure 19 – Schematic of and industrial mesh belt furnace and the time-temperature graph [6].

3.4.4 Sintering Atmosphere

A very important process parameter in all sintering operations is the atmosphere at which sintering is completed. Aluminum P/M parts can be sintered in a controlled, inert atmosphere or in vacuum. Nitrogen, dissociated ammonia, hydrogen, argon, and vacuum have been used for sintering aluminum. However, nitrogen is preferred because it results in high as-sintered mechanical properties and is also an economical option [14]. Inert atmospheres are used to ensure that oxidation of the materials is kept to a minimum. When using such protective atmospheres, the dew point of the gas is recommended to be kept at or below -40 °C with an oxygen content <5 ppm [14].

3.4.5 Sintering of P/M Aluminum Alloys

Sintering is considered the most critical step in aluminum P/M processing. Aluminum reacts readily with oxygen and moisture to form oxides and hydroxides. These compounds are thermodynamically stable and cannot be reduced by hydrogen at practical operating temperatures. Therefore, an inert atmosphere of dry nitrogen is required to keep these compounds from forming. P/M aluminum alloys also contain magnesium to break up the oxide layer present on the aluminum powders to facilitate sintering.

Aluminum P/M alloys are also sintered at a composition and temperature where liquid phase sintering can occur. A general rule of thumb is to have sintering parameters where by 10 to 20 weight percent liquid is formed to maximize the sintered density but avoid extensive distortion. Figure 20 shows the effects of a variation of copper content in AC2014 on the dimensional change and sintered density [15]. The modest increase in copper content resulted in a greater amount of liquid phase forming and a significant variation in sintered density and dimensional change. This acute behaviour highlights the need for careful control over sintering temperature and alloy chemistry that is inherent in aluminum P/M processing.

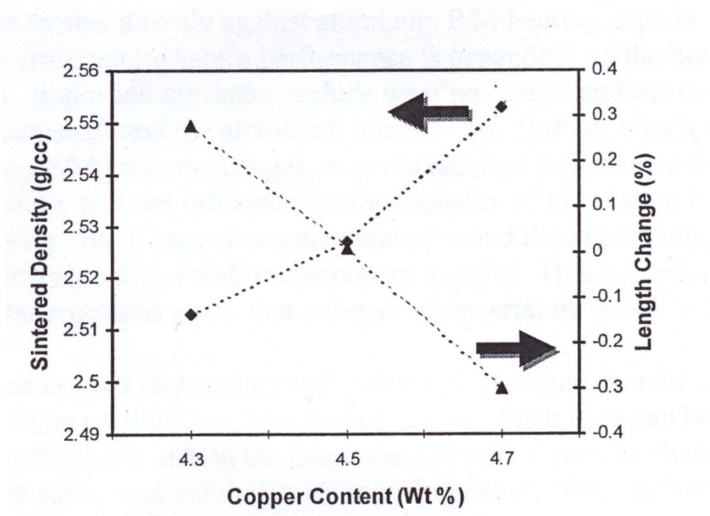

Figure 20 – Dimensional change and sintered density as functions of copper content of AC2014 [15].

3.5 Aluminum Alloys

3.5.1 Classification of Wrought Aluminum Alloys

To classify wrought aluminum and wrought aluminum alloys, a four digit system is used. In this, the first digit indicates the alloy group and the last two identify the aluminum alloy. The second digit indicates the modifications or impurity limits of the original alloy. A list of the wrought aluminum alloy groups is as shown in Table II [13]. Alloys are designed to serve a particular purpose, with alloying elements used to achieve the desired properties. The alloying elements typically used in aluminum alloys and their effects are described in Table III [16].

Table II – Wrought aluminum alloy groups [13].

Aluminum Alloy Grouped by Major Alloying Element(s)	Designation
Al, 99.00% minimum or greater	1XXX
Copper (Cu)	2XXX
Manganese (Mn)	3XXX
Silicon (Si)	4XXX
Magnesium (Mg)	5XXX
Magnesium (Mg) and silicon (Si)	6XXX
Zinc (Zn)	7XXX
Other elements	8XXX
Unused series	9XXX

Table III – Effects of alloying elements in aluminum alloys [16].

Alloying Element	Principal Effects
Cu	Substantial increase in strength, permits precipitation hardening, reduces corrosion resistance and ductility.
Mn	Increases strength through solid-solution strengthening and improves work hardening ability.
Si	Increases strength and wear resistance while reducing CTE, in combination with magnesium produces precipitation hardening.
Mg	Increases strength through solid-solution strengthening and improves work hardening ability.
Zn	Substantial increase in strength, permits precipitation hardening, can promote susceptibility to stress corrosion cracking.
Sn	Enhances tribological performance.
Fe	Increases strength (at ambient and elevated temperatures) of pure aluminum, generally a residual element.
Cr	Increases stress corrosion cracking resistance.
Ni	Improves elevated temperature strength.
Ti,Zr	Grain refiners, particularly in filler metals.
Li	Substantially increases strength and Young's modulus, provides precipitation hardening and decreased density.
Sc	Substantially increases strength through age hardening, grain refining element particularly in weld metal.
Pb, Bi	Assist chip formation in free machining alloys

3.5.2 Temper Designations of Aluminum Alloys

Many alloying systems are subjected to secondary processing. Aluminum alloys are no different and often involve heat treatments and/or mechanical working of the alloys to achieve the desired mechanical properties of the finished product. These secondary treatments are termed tempers and are indicated as a hyphenated code adjacent to the alloy designation followed by a numerical temper subdivision [13].

There are four temper categories [13]. The first is 'F' which denotes as fabricated. There are no mechanical properties specified for this condition and no secondary processing is applied to the material. 'O' refers to the annealed condition. These alloys have the lowest strength and highest ductility. 'H' refers to strain hardened (cold worked) materials. The letter 'H' is always followed by at least two digits to identify the amount of cold work and any heat treatments done as described below.

H1 strain hardened only.

H2 strain hardened and partially annealed.
Alloys are hardened more than is required and then annealed at a low temperature to soften them to the required degree of hardness and strength.

H3 Strain hardened and stabilized. Stabilization is a low-temperature heat treatment applied during or on completion of fabrication to improve ductility and stabilize the properties.

H4 Strain hardened and painted. Alloys that may be subjected to low-temperature heat treatment as part of a paint baking or adhesive curing operation.

'T' refers to thermally treated. This identifies the alloys that are aged to produce a stable condition. The 'T' is always followed by one or more numbers to identify the specific heat treatment as shown below [13].

T1 cooled from fabrication temperature and naturally aged

T2 cooled from fabrication temperature, cold worked and naturally aged

T3 solution treated, cold worked and naturally aged

T4 solution treated and naturally aged

T5 cooled from fabrication temperature and artificially aged

T6 solution treated and artificially aged

T7 solution treated and stabilized by overaging

T8 solution treated, cold worked and artificially aged

T9 solution treated, artificially aged and cold worked

T10 cooled from fabrication temperature, cold worked and artificially aged

3.6 2XXX series aluminum alloys

The 2XXX series of wrought aluminum alloys can be classified into two different groups, namely, aluminum-copper and aluminum-copper-magnesium. Both groups are strengthened by the formation of a precipitate phase. The division is due to the type of precipitate that is formed. In aluminum copper alloys, the main precipitate that is formed is θ ($CuAl_2$) and the precipitation

sequence is as shown below. The GP1 zones are formed at temperatures below 130°C by copper atoms segregating in the supersaturated solid solution. GP2 zones have a tetragonal structure and have a higher copper content than GP1 zones. When the Al-Cu alloys are overaged, the θ' phase is formed. This phase is completely incoherent with the α matrix and has a tetragonal structure. Aging at temperatures of about 190°C for long periods of time allows the formation of the θ phase which has a BCT structure and is a highly overaged condition. [13] Compositions and applications of select aluminum-copper alloys premised on this strengthening effect are shown in Table IV.

Supersaturated Solid Solution → GP1 zones → GP2 zones (θ" phase) → θ' → θ ($CuAl_2$)

Table IV – Composition (w/o) and applications of 2xxx series aluminum-copper alloys [13].

Alloy	% Cu	% Mn	% Other	Applications
2011	4.4	0.8	0.4 Bi, 0.4 Pb	Screw-machine products
2025	4.0	0.7	0.8 Si	Forgings, aircraft products
2219	4.0		0.06 Ti, 0.10 V, 0.18 Zr	Structural use to 660°f, high-strength weldments for cryogenic and aircraft parts

The addition of magnesium to aluminum-copper alloys is found to accelerate and intensify precipitation hardening. Magnesium also alters the type of precipitates formed from Cu_2Al (θ) to Al_2CuMg (S). The principal precipitation sequence of Al-Cu-Mg alloys is shown below. GP zones are formed in the early stages of aging at low temperatures and their exact crystalline structure has not been firmly established. S' is a metastable phase that is incoherent. [13] Compositions and applications of select aluminum-copper-magnesium alloys are shown in Table V.

Supersaturated Solid Solution → GP zones → S' (Al_2CuMg) → S (Al_2CuMg)

Table V – Composition (w/o) and applications of select 2XXX series aluminum-copper-magnesium alloys [13].

Alloy	% Cu	% Mg	% Mn	% Si	% Ni	% Other	Applications
2014	4.4	0.5	0.8	0.8			Truck frames, aircraft structures
2017	4.0	0.6	0.7	0.5			Screw-machine products, fittings
2018	4.0	0.7			2.0		Aircraft engine cylinder heads and pistons
2024	4.4	1.5	0.6				Truck wheels, screw-machine products, aircraft structures
2218	4.0	1.5			2.0		Jet engine impellers and compressor rings, aircraft engine cylinder heads and pistons
2618	2.3	1.6				0.18 Si, 1.0 Ni, 1.1 Fe, 0.07 Ti	Aircraft engines, temperatures to 238°C

Some mechanical properties of select aluminum-copper and aluminum-copper-magnesium alloys are shown Table VI. It can be seen that the tensile strengths of aluminum-copper-magnesium alloys are greater than that of the aluminum-copper alloys in the T6 condition, although the ductility is not as great.

Table VI – Mechanical Properties of select 2XXX series aluminum alloys [13].

Alloy	Temper	UTS (MPa)	Yield Strength (MPa)	% Elongation
Aluminum-copper alloys				
2011	**T6**	393	269	15
2025	**T6**	400	255	19
2219	**T6**	413	289	10
Aluminum-copper-magnesium alloys				
2014	**T6**	482	413	13
2024	**T6**	475	393	10

3.7 Commercial P/M Aluminum Alloys

When designing a new alloy, the mechanical properties and the processing technique must be considered. P/M alloys generally differ slightly in chemistry from the wrought and cast counterparts to optimize the press and sinter abilities of the alloy. There are only a few P/M aluminum alloys produced on an industrial scale; comparatively, cast and wrought approaches have over 100 different alloys available for use. These alloys are produced by several major suppliers, such as Ampal and Ecka-Granules. The compositions of those available from Ecka-Granules are shown in Table VII with typical mechanical properties provided in Table VIII [8].

Table VII – Compositions of Ecka-Granules Alumix P/M Aluminum Alloys [8].

ECKA Alumix	Alloy	Cu %	Mg %	Si %	Zn %	Wax Lubricant	Aluminum
Alumix 13	AlCuMg	4.5	0.5	-	-	1.5	remainder
Alumix 123	AlCuSiMg	4.5	0.5	0.7	-	1.5	remainder
Alumix 231	AlSiCuMg	2.5	0.5	14	-	1.5	remainder
Alumix 321	AlMgSiCu	0.2	1	0.5	-	1.5	remainder
Alumix 431	AlZnMgCu	1.5	2.5	-	5.5	1.2	remainder

Table VIII – Mechanical Properties of Ecka-Granules Alumix P/M Aluminum Alloys [8].

Alloy	Sintered Density (g/cm^3)	Tensile Strength (N/mm^2)	Hardness (HB)	Elongation (%)
Alumix 13*	2.50	160 T1	55	5
Alumix 123*	2.50	190 T1	60	4
Alumix 231**	2.67	240 T1	100	1-2
Alumix 321*	2.47	120 T1	40	5
Alumix 431***	2.55	400 T76	150	2

*350 MPa compaction pressure ** 620 MPa *** 400 MPa

Chapter 4.0 Hot Deformation

Hot deformation of metals is the process of deforming a workpiece to achieve the desired shape and/or mechanical properties. Hot deformation can be accomplished by a number of techniques including forging, swaging, or extrusion. These processes are described below as well as how they affect P/M alloys.

4.1 Forgeability

The forgeability of a metal may be defined as its capability to be shaped without cracking [17]. Impurities in the metal or small changes in composition can have significant effects on this attribute. As such, there are a number of tests used to measure forgeability. Two of those more commonly encountered are the upsetting test and the hot-twist test. The upsetting test uses a solid cylindrical specimen between two flat dies. During the compression of the specimen (upsetting) observations are made regarding any cracking on the barreled surfaces. It is said that the higher the reduction in height prior to cracking, the greater the forgeability of the metal [17]. Friction at the die/workpiece interfaces has a large effect on cracking. With increased friction, the specimen will fracture at a lower reduction in height. Upsetting tests can be performed at various temperatures and strain rates. Due to the fact that there are a large number of variables involved in this test, standard values on the forgeability of materials cannot be determined, but qualitative remarks can be made.

The hot-twist test is a torsion test in which a long, round specimen is twisted continuously until it fails [17]. The test is performed at various temperatures and the number of turns that each specimen undergoes before failure is observed. From this, the optimal forging temperature can then be determined.

4.1.1 Forgeability of Aluminum Alloys

Aluminum alloys can be forged into a variety of shapes using many different forging technologies. Closed-die forgings of aluminum alloys are usually produced to more highly refined final forging configurations than hot-forged carbon and alloy steels. For a given aluminum alloy forging shape, the pressure requirements vary widely, depending primarily on the composition of the alloy being forged, the forging process being employed, strain rate, the lubrication conditions, and the forging preform/tooling temperatures.

As a class of alloys, aluminum alloys are generally considered to be more difficult to forge than carbon steels and many alloy steels. When compared to nickel and titanium based alloys, aluminum alloys are considerably more forgeable, particularly in conventional forging process technology, in which dies are heated to 540 °C or less [18]. The relative forgeability of ten commonly forged aluminum alloys is illustrated in Figure 21 [18]. The relative forgeability is based on the amount of energy required to deform the alloy for the typical forging temperature of the alloy, as well as the difficulty in achieving a specific degree of deformation and the cracking tendency of the alloy under forging process conditions. Wrought aluminum alloys such as 1100 and 3003, would be rated significantly more forgeable than the alloys in Figure 21. However, these alloys have limited applications in forging because they cannot be strengthened by heat treatment.

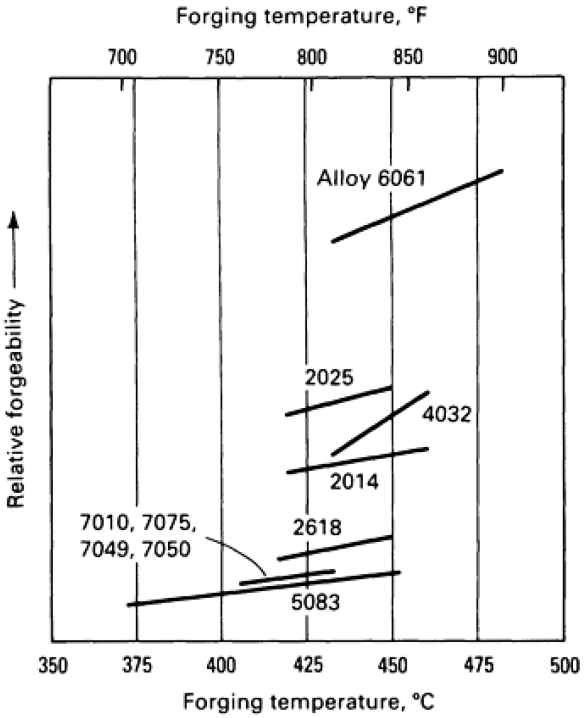

Figure 21 – Relative forgeability of select aluminum alloys [18].

4.1.2 Forging Temperature

Forging can be carried out cold (room temperature), warm or hot. The corresponding temperature range for each is determined by the homologous temperature T/Tm as shown in Table IX [17]. It is also important to note that recrystallization occurs at a homologous temperature of around 0.5. This plays a role in increasing the amount that a material can be deformed before cracking in that new stress free grains will be continuously formed.

Table IX – Homologous temperature ranges for deformation processes [17].

Process	T/T_m
Cold Working	<0.3
Warm Working	0.3 to 0.5
Hot Working	>0.6

The relative forgeability of aluminum alloys improves with increasing metal temperature as shown in Figure 21. However, there is considerable variation in the effect of temperature for the

alloys plotted. The high silicon alloy 4032 shows the greatest effect, while the high-strength Al-Zn-Mg-Cu 7XXX alloys display the least.

The effect of temperature on flow stress of aluminum alloy 6061 (a highly forgeable aluminum system) is shown in Figure 22 [18]. There is nearly a fifty percent increase in flow stress between the highest temperature (480 °C) and the minimum temperature (370 °C) recommended for 6061. For other, more difficult-to-forge alloys, such as the 2XXX and 7XXX series, the change in flow stress with temperature is even greater which gives significantly narrower temperature ranges for forging.

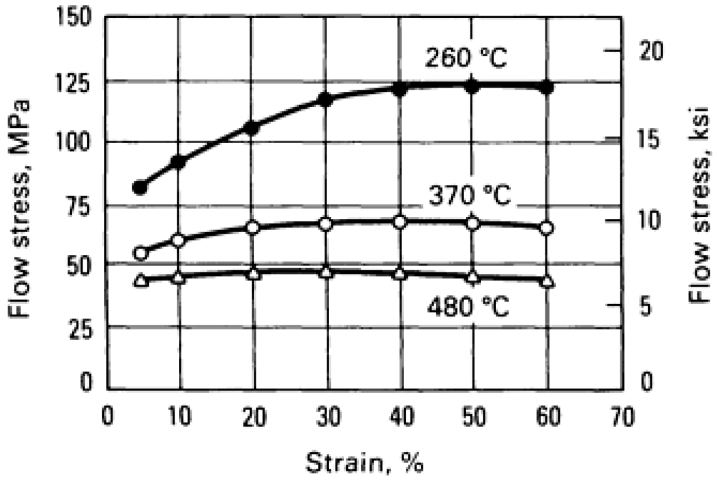

Figure 22 – Effect of temperature on flow stress for 6061 specimens strained at a rate of $10s^{-1}$ [18].

The forging temperature ranges for the most commonly forged aluminum alloys are listed in Table X [18]. The total temperature spread for most alloys is relatively narrow. Obtaining and maintaining of the proper metal temperatures in the forging of aluminum alloys is critical to the success of the forging process. The temperature of the dies and deformation rates play key roles in the actual forging temperature achieved. Hence, the dies in all forging processes for aluminum alloys are heated to maintain the temperature of the metal during forging. The die temperature for various forging processes of aluminum alloys is shown in Table XI [18]. The

required die temperatures for processes with high deformation rates such as hammers are much lower than processes with slow deformation rates such as hydraulic forging. The forging of aluminum alloys using hydraulic presses are essentially isothermally forged as the die and metal temperatures are the same. Here, the hot dies are needed to maintain the required metal temperature during the relatively long period over which deformation transpires.

Table X – Recommended forging temperature ranges for select aluminum alloys [18].

Aluminum alloy	Forging temperature range °C
1100	315-405
2014	420-460
2025	420-450
2219	425-470
2618	410-455
3003	315-405
4032	415-460
5083	405-460
6061	430-480
7010	370-440
7039	380-440
7049	360-440
7050	360-440
7075	380-440

Table XI – Recommended forging die temperatures when processing aluminum alloys [18].

Forging process/equipment	**Die temperature** °C
Open-die forging	
Ring rolling	95-205
Mandrel forging	95-205
Closed-die forging	
Hammers	95-150
Upsetters	150-260
Mechanical presses	150-260
Screw presses	150-260
Orbital (rotary) forging	150-260
Spin forging	150-315
Roll forging	95-205
Hydraulic presses	315-430

4.2 Forging Equipment

Aluminum alloy forgings are produced on the full spectrum of forging equipment, including hammers, hydraulic presses, mechanical and screw presses. Selection of forging equipment for a given forging shape and type is based on the capabilities of the equipment, forging design sophistication, desired forging process, and cost. Hydraulic presses are load-restricted machines as their capability for carrying out a forming operation is limited mainly by the maximum available load [18]. The ram operates at a constant low speed that can be varied continuously. There are two main types of hydraulic presses, direct-driven and accumulator-driven (Figure 23). Direct-driven presses employ an oil or water emulsion as the working medium and the maximum press load is available at any point during the ram stroke. Accumulator-driven presses also employ a water-oil emulsion as the working medium but also include nitrogen, steam, or air loaded accumulators to keep the medium under pressure. Here, the available load decreases slightly depending on the length of the stroke.

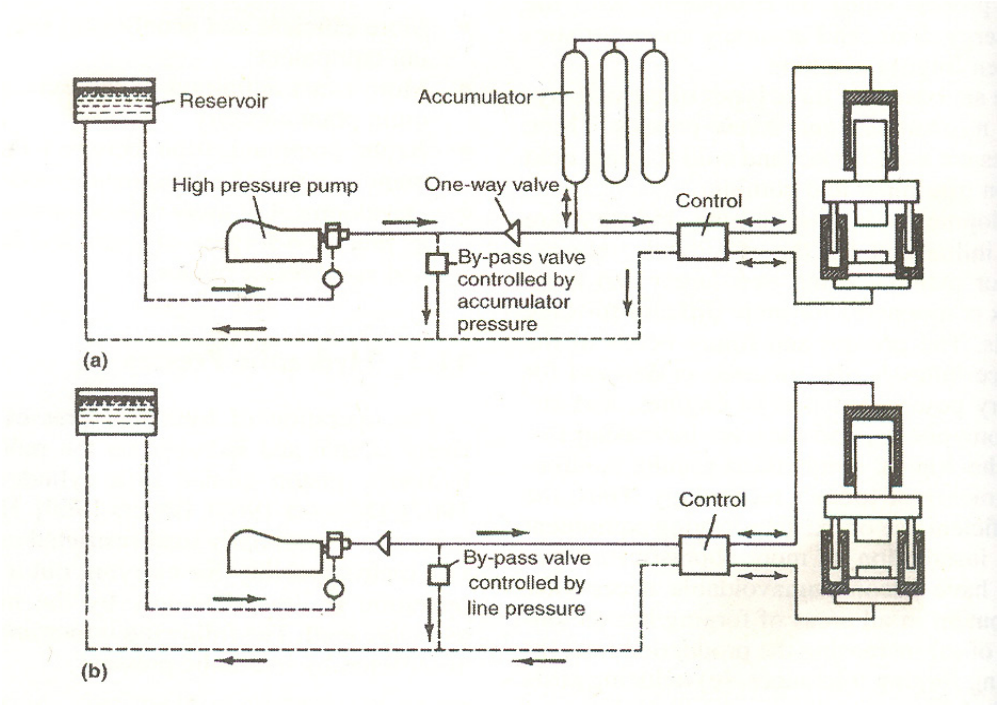

Figure 23 – Diagrams of (a) accumulator drive and (b) direct drive hydraulic presses [17].

Even though the fastest hydraulic presses are slower acting than mechanical or screw presses, hydraulic presses are frequently used for producing large closed die forgings or very intricate forgings. The deformation achieved using a hydraulic press is more controlled than the typical mechanical or screw presses, or hammers. The slow controlled strain rates minimize the resistance of the aluminum alloy to deformation, reduce pressure requirements, and facilitate the ability to achieve the desired shape. Collectively, these attributes make hydraulic forging a very useful process for aluminum alloys [17].

A mechanical press derives its energy from a flywheel, which is transferred to the workpiece by a network of gears, cranks, eccentrics, or levers [18]. The length of the stroke and the available force at various stroke positions are factors that determine the ability of mechanical presses to deform the workpiece. The two main types of mechanical presses are crank drive and cam drive. Screw presses use a friction, gear, electric, or hydraulic drive to accelerate a flywheel and the screw assembly [18]. The angular kinetic energy of the screw is then converted into linear energy of the slide or ram. Both mechanical and screw presses are extensively used for the closed-die forging of aluminum alloys.

The hammer press is the least expensive and most versatile type of equipment for compression. Hammers are energy limited mechanisms which derive energy from the potential energy of the ram [18]. Gravity and power-drop hammers are used for both the open-die and closed-die forging of aluminum alloys [17]. Hammers deform the metal with very high strain rates. Control of the stroke length, force, and the speed of the hammer is very important to the forging of aluminum alloys due to their acute sensitivity to strain rate.

4.3 Forging Processes

There are several factors that play a role in the selection as to which forging method should be employed in a given scenario. These factors include the desired forged shape, the sophistication of the forged shape design, and cost. It is not uncommon for multiple forging methods to be combined to achieve a particular forging shape and metallurgical structure. An example of this is that open-die forging often precedes closed-die forging to preshape the metal so that it conforms better to subsequent closed die operations.

Collectively, there are a large number of forging processes [18]:

- Closed/impression die forging with flash
- Closed/impression die forging without flash
- Electro-upsetting, Forward extrusion
- Backward extrusion
- Radial forging
- Hobbing
- Isothermal forging
- Open-die foging
- Orbital forging
- Powder metal (P/M) forging
- Upsetting
- Nosing
- Coining

Open-die forging (Figure 24) typically involves placing a solid cylindrical workpiece between two flat dies (platens) and reducing its height by compressing it; an operation that is also known as upsetting [18]. Typically, a specimen will develop a barrel shape during this process. Open-die forging is often used to produce small quantities of aluminum alloy forgings to avoid the costs associated with the construction of expensive closed dies. Open-die forgings of aluminum alloys can be produced to a wide variety of shapes such as simple cylinders or rectangles or very complex contoured forgings. The complexity and tolerances achievable in open-die forging

depend on the skill of the press operator or the computer control program. Open-die forging of aluminum alloys are also frequently used to produce performs for closed-die forgings [18]. The use of precise perform shapes can ultimately improve the dimensional consistency and tolerances of the resulting closed-die forging. There is also a potential cost savings through material conservation.

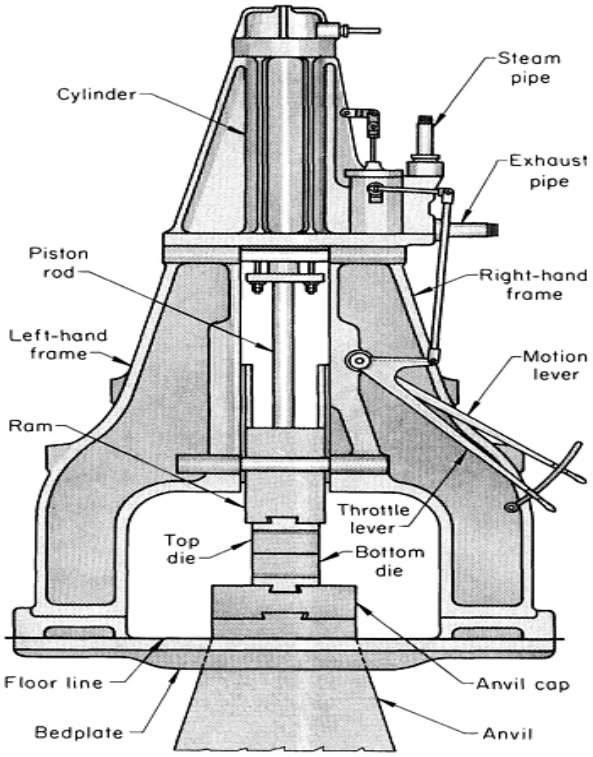

Figure 24 – Schematic of a typical open die forging operation [17].

Closed die forging, or impression-die forging, is the shaping of hot metal completely within the walls or cavities of two dies that come together to enclose the workpiece on all sides [18]. The forging stock, generally round or square bar, is cut to length to provide the volume of metal needed to fill the die cavities. To allow for the displacement of excess material a flash cavity is present. The flash allowance is, in effect, a relief valve for the extreme pressure produced in

closed dies. Flash also acts as a brake to slow the outward flow of metal in order to permit complete filling of the desired configuration. The energy required for metal to fill the flash cavity greatly increases the total forging pressure required as shown in Figure 25 [17].

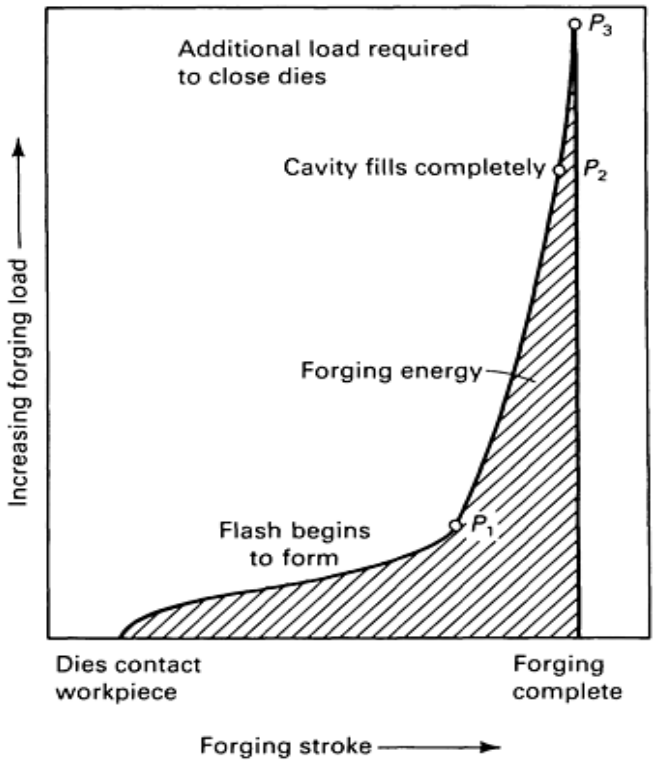

Figure 25 – Load requirements during the stroke of a typical closed die forging with flash [17].

The majority of aluminum alloy forgings are produced using closed dies as more precise geometries can be produced. There are four main types of closed die configuration, blocker-type, conventional, high-definition, and precision. These dies types are illustrated in Figure 26 [17]. Blocker-type forgings are produced using relatively inexpensive dies resulting in less refined dimensions. These forgings are cheaper to produce, although they require more machining. Conventional closed-die forgings are the most common type for aluminum forging. They have tighter tolerances than blocker-type forgings, although they are more expensive to produce. High-definition forgings are used to produce near-net shape products. These forgings require the use of precise forging equipment and process control to achieve tighter tolerances

which reduce machining costs. Precision forgings are the most sophisticated aluminum forging design. These forgings often require no post-forge machining and can be very cost effective.

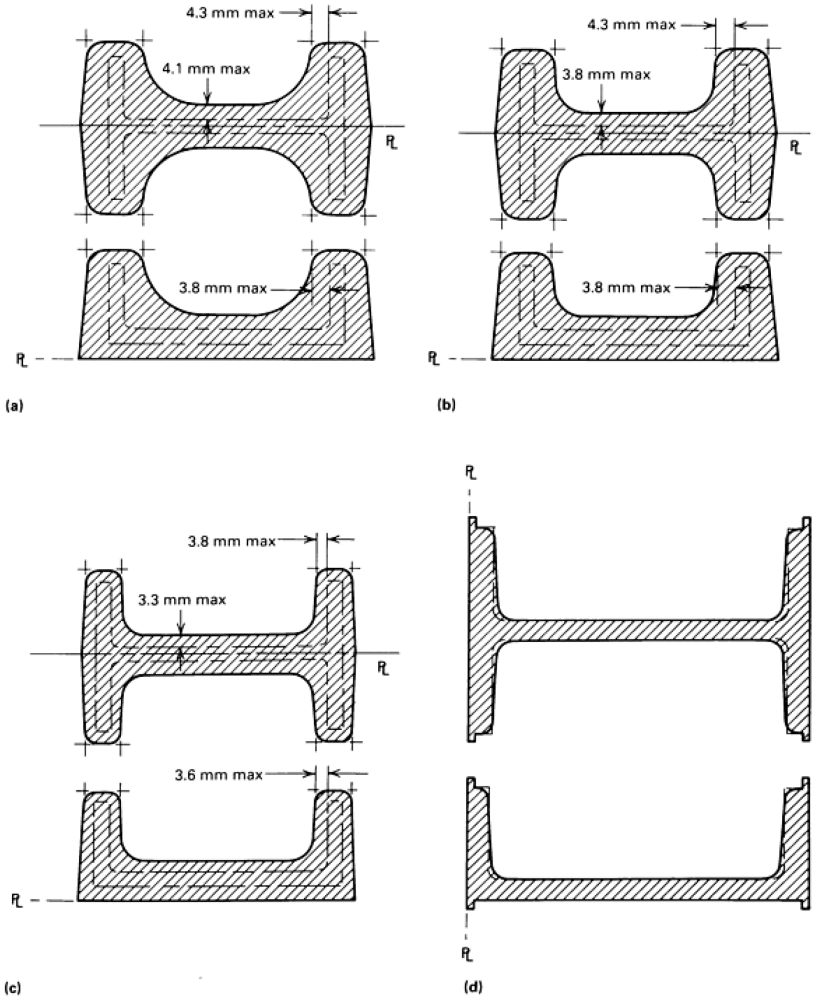

Figure 26 - Types of aluminum closed-die forgings (a) blocker-type, (b) conventional, (c) high-definition, and (d) precision [17].

In all of the aforementioned forging processes, the frictional conditions at the die/workpiece interface greatly influence metal flow. This effect is moderated through the use of lubricants that are sprayed on the tooling and/or applied as a coating to the perform.

A quality lubricant must be able to effectively reduce the friction between the die surface and the workpiece, be able to handle the high temperatures and pressures, and leave the metal

unaffected [17]. Although the compositions of commercially used lubricants for the forging of aluminum alloys are generally highly proprietary, the active element is generally graphite. The graphite is generally used in a colloidal suspension in mineral oils, mineral spirits, or water [17]. Other compounds are also added to the colloidal suspensions to achieve the desired properties for the specific application.

4.4 Forging of P/M Aluminum Alloys

Powder forging (P/F) involves the hot deformation of a sintered preformed part in a closed die. P/F is similar to forging of conventional materials, except for the presence of preexisting voids. These voids change the mechanical properties of the alloy as pores act as fracture initiation sites. The principal aim of P/F is to eliminate these pores. A compressive axial strain is required for this purpose. The compressive strain and lateral flow lead to the refinement of the microstructure. The presence of porosity also causes a volume change during forging. The properties of the alloy are similar to the properties of conventional aluminum forgings, which is in part a consequence of the relatively high density of the sintered preform.

P/F is generally carried out in heated closed dies with little or no flash. There are two basic forms – hot re-pressing and hot upsetting, as shown in Figure 27 [19]. Hot re-pressing is the forging of a material in a tight fitting die to densify it but maintain close tolerances of the final product. Material flow during densification is mainly in the direction of pressing. Densification is achieved due to the hydrostatic nature of the forces in the closed die, which causes the pores to flatten [19]. In hot upsetting, the preform experiences a significant amount of lateral material flow. The die used is larger than the preform and initially the material undergoes upsetting to fill the die cavity then collapses pores by re-pressing. This type of forging gives greater mechanical properties as the shear stresses in the workpiece promotes the break-up of the remaining interparticle oxide films from the powders [19]. This leads to strong metallurgical bonding across

the collapsed pores, which gives the material enhanced fracture toughness and fatigue strength. This method also requires less forging pressure than hot re-pressing although it does not give the same close geometrical tolerances achieved in re-pressing [19].

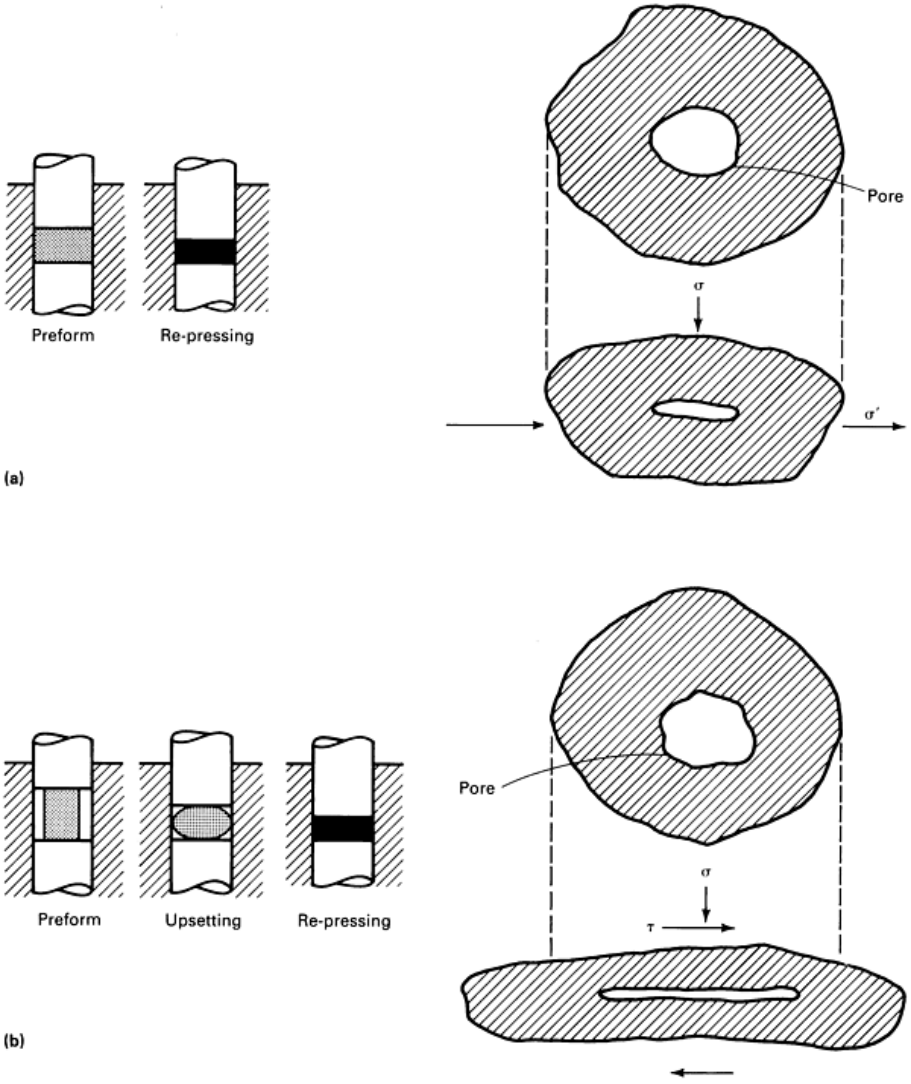

Figure 27 – Types of powder forgings and stress conditions on pores (a) re-pressing, and (b) upsetting [19].

4.5 Rotary Swaging

Rotary swaging is a process for reducing the cross-sectional area of bars, tubes, or wires by repeated radial blows with two or more dies [20]. In this process, the workpiece is elongated while the cross-sectional area is reduced. Most swaged workpieces are round as the simplest form of reduction is the reduction in diameter. For applications that require more complex shapes, swaging can also be applied to produce straight and compound tapers. Contours on the inside diameter of tubing, and swaging can also be done to change round workpieces to square or other shapes. Swaging can be done hot or cold, depending on the ductility of the material, and the amount of reduction desired.

4.5.1 Swaging machines

There are a variety of different swaging machine configurations available. The simplest is the standard rotary swager. This type of swager involves the use of a two die system that oscillates between an open and closed position rapidly to provide the impact action that shapes the workpiece [20]. It consists of a head and a base. The head contains the swaging components and the base supports the head and houses the motor. A hardened steel ring slightly larger in diameter than the bore of the head is pressed into the head so that the ring is in compression. The centrally located spindle within the ring is slotted to hold the backers and dies and is mounted in a tapered-roller bearing. Flat steel shims are placed between the dies and backers. A roll rack containing a set of rolls is located between the press-fitted ring and the backers (Figure 28 (a)). The spindle is rotated by a motor-driven flywheel. During rotation of the spindle, the dies move outward by centrifugal force and inward by the action of the backers striking the rolls. The number of blows (impacts) produced by the dies is 1000 to 5000 per minute, depending on the size of the swager [20].

The amount of die opening can be changed to some extent during operation by a mechanical device that restricts the amount that the dies and backers can move under centrifugal force. However, the closed position of the dies cannot be changed during operation as the swager must be stopped and shims inserted between the dies and the backers. The severity of the blow can be varied by using shims of different thicknesses. The dies should be shimmed tight enough to obtain a reasonable amount of interference between the backers and the rolls when the dies are in the closed position.

Other types of rotary swaging machines include the stationary-spindle swager, creeping spindle swager, alternate-blow swager, and the die-closing swager as shown in Figure 28. The stationary-spindle swager uses dies that oscillate inward at the same time. The creeping spindle swager is one in which the dies rotate in order to help eliminate flash formation. The alternate blow swager uses four dies where the blows alternate in the impact direction. Finally, the die closing swager is used for swaging only a section of the workpiece at a time.

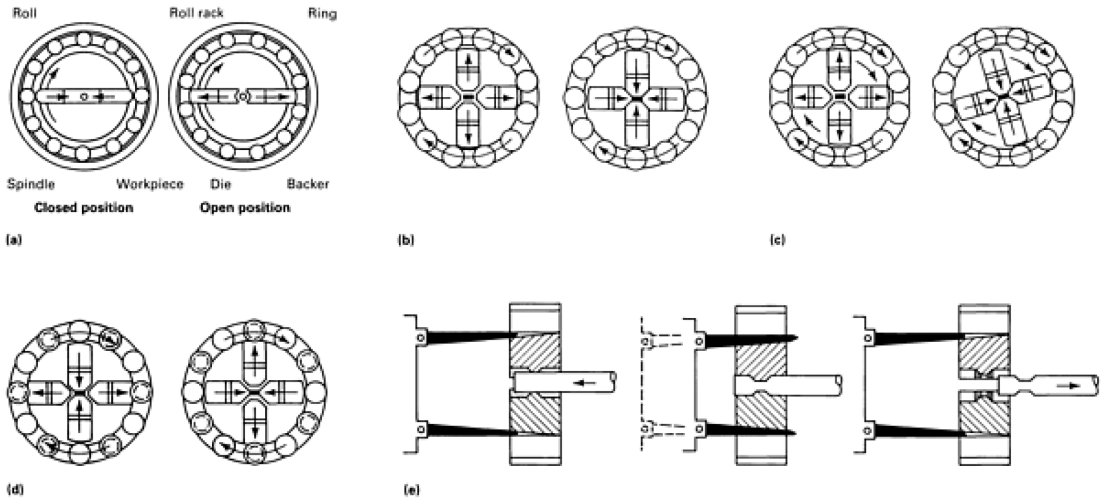

Figure 28 - Rotary Swaging machines (a) standard rotary swager, (b) stationary-spindle swager, (c) creeping-spindle swager, (d) alternate-blow swager, and (e) die-closing swager [20].

4.5.2 Swaging Dies

The main areas of concern for the swaging die material used is the resistance to shock and wear. It is necessary in some cases to sacrifice wear resistance in order to prevent die breakage due to lack of shock resistance. Some typical tool steels for cold swaging include A8, D2, S3, S7, and M2. M2 and H13 are frequently used for hot swaging [20]. For high-production applications, shock-resistant grades of carbide are used for the added wear resistance. A drawback of using carbide dies, however, is increased backer and roll wear.

There are many swaging die shapes available. Nine typical die shapes are, standard single taper, double taper, taper point with cross stop, chopper, piloted, long taper, single extension, and contour as demonstrated in Figure 29 [20]. The type of die used depends on the shape, size, and material of the workpiece.

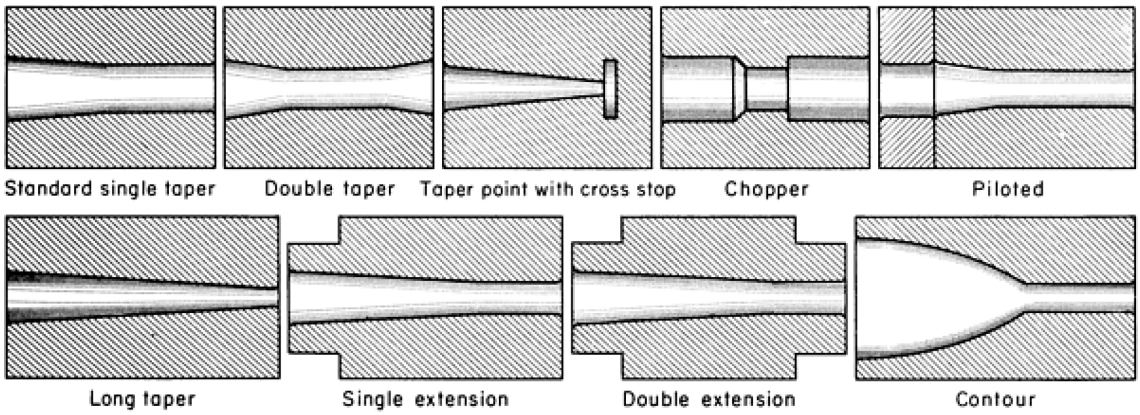

Figure 29 – Typical die shapes used in rotary swaging [20].

4.5.3 Metal Flow in Swaging

The metal flow during rotary swaging is depicted in Figure 30 [20]. The metal flow is not confined to one direction. As the workpiece is fed into the swaging machine, the metal flows out of the taper in a direction opposite to the feed. There is actually a minimal amount of metal flow through the straight portion, known as the blade. Some metal flow also occurs in the transverse

direction, towards the space between the dies so as to form a flash. Caused by overfeeding in the swaging machine, the amount of flash can be limited by using more complex swaging machine orientations, such as creeping spindle swaging. Otherwise the flash will have to be machined off as part of a secondary operation.

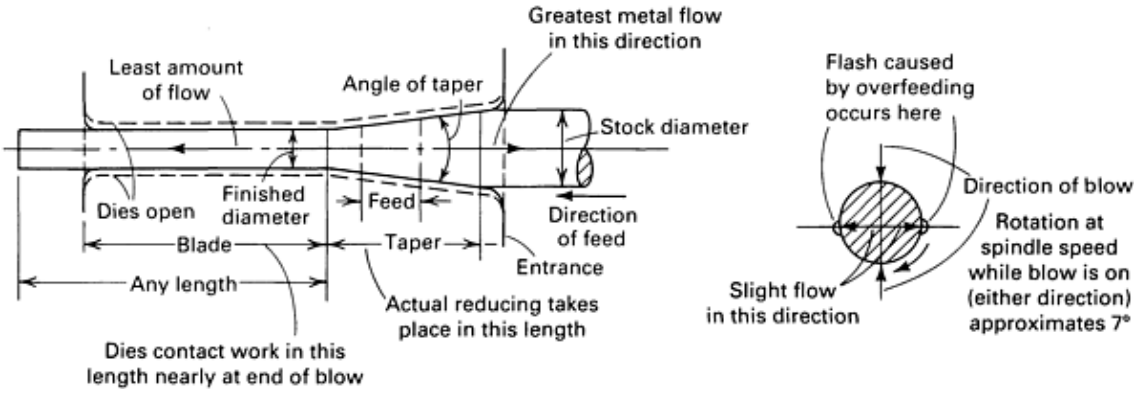

Figure 30 – Metal flow in rotary swaging [20].

4.5.4 P/M Swaging

P/M materials are generally compacted, and then sintered. These materials differ from their wrought counterparts as they generally contain a certain amount of porosity. This porosity greatly affects the mechanical properties of the material, thus limiting its selection in many highly demanding applications. There are secondary operations, however, that can be employed to increase the density of press and sinter P/M materials. Some of these include applying an impact load to effectively close the pores. One way this can be done is to forge the material. Another method is the swaging of P/M alloys, which follows the same general function to close the pores, and end up with a fully dense material with exceptional mechanical properties.

The swaging of P/M materials is a process that has not been extensively researched. One of the few studies on the swaging effects of P/M aluminum alloys was a study on an aluminum silicon

alloy with an equivalent composition to the wrought alloy AA4032 [21]. It was found that swaging was very effective at increasing the density of the alloy. Swaging increased the density from ~92% of the theoretical density to ~98%. This increase in density also meant that the mechanical properties were increased. For example, the yield strength and UTS of the as sintered state were increased by ~50% while the ductility was doubled.

A study was also done by MacAskill et. al. where the P/M alloy Alumix 431D (equivalent to wrought 7075) was hot swaged to achieve properties comparable to the wrought alloy [22]. Measured values of yield and UTS in the swaged PM product were superior by 14 and 4% respectively although ductility remained inferior. The fatigue properties were also found to be greatly increased after hot swaging, with a fatigue life of approximately 250 MPa at 10^7 cycles, which surpassed that of wrought 7075-T6 (~210 MPa at 10^7 cycles).

Chapter 5.0 Metal Matrix Composites

The use of aluminum based metal matrix composites (MMCs) is increasing in automotive and aerospace applications due to their high specific strength, stiffness and high hardness. The combination of weight reduction and improved properties can result in lower fuel consumption, reduced emissions and improved performance with the use of these composites [23]. MMCs, like all composites, consist of at least two chemically and physically distinct phases, suitably distributed to provide properties not obtainable with either of the individual phases. There are generally two phases present – a fibrous or particulate ceramic phase distributed in a metallic matrix. By blending the alloy powder with a strengthening phase, discontinuously reinforced aluminum-matrix composites containing insoluble particulates, whiskers, or fibers are produced for high-performance structural applications. Some of the advantages of MMCs with respect to unreinforced metals are [24]:

- Weight savings due to higher strength-to-weight ratio
- Exceptional dimensional stability (compare, for example, SiC/Al to Al)
- Higher elevated temperature stability, i.e., creep resistance
- Significantly improved cyclic fatigue characteristics
- MMC's manufactured by the powder metallurgical route (PM-MMC) offer economical solutions for the production of high performance materials.

Aluminum MMCs have been studied worldwide. They are generally isotropic and less costly in comparison with continuous-fiber-reinforced composites [14]. The discontinuously reinforced aluminum (DRA) composites are attractive for near-term commercial applications. Silicon carbide (SiC) or alumina (Al_20_3) particle reinforced aluminum composites have higher stiffness and, in general, high wear resistance in comparison with unreinforced aluminum alloys. Silicon carbide whisker, however, is currently the most widely utilized reinforcement for the DRA composites for obtaining high resistance to creep and higher use temperatures. Selection of

suitable composition of the matrix material is important to meet mechanical and physical property requirements. Minor alloying additions in the wrought alloys are generally detrimental to the mechanical properties of the composites because of undesirable interfacial reaction during the P/M consolidation [14].

In general, MMCs have a metal or alloy as the matrix and a ceramic as the reinforcement. There are three kinds of MMCs subdivided in accordance with the nature of the reinforcement – particle reinforced, fiber or whisker reinforced, and continuous fiber or sheet reinforced MMCs [24]. These different types of composites are illustrated in Figure 31 [25]. Some examples of the commonly used reinforcements are shown in Table XII [24].

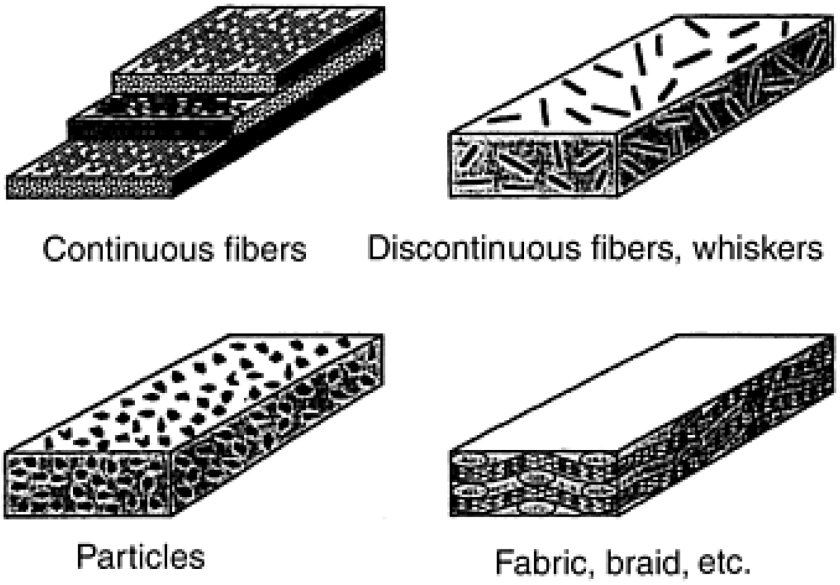

Figure 31 – Common forms of fiber reinforcement [25].

Table XII – Typical reinforcements used in MMCs [24].

Type	Aspect Ratio	Diameter µm	Examples
Particle	1-4	1-25	SiC, Al_2O_3, BN, B_4C, WC
Short fiber or whisker	10-10000	1-5	C, SiC, Al_2O_3, Al_2O_3+SiO_2
Continuous fiber	>1000	3-150	SiC, Al_2O_3, C, B, W, Nb-Ti, Nb_3Sn

DRA materials have several advantages over continuously reinforced composites. For one, they are less expensive to fabricate, and the performance increase comes at lower additional costs when compared to aligned reinforcements. Another advantage is the isotropic nature of the properties achieved. In applications requiring isotropic properties, DRAs outperform continuously reinforced composites [25]. Ceramics and graphitic materials are typically used as reinforcement phases in DRAs. Properties of the most common phases used as the reinforcement for DRAs are listed in Table XIII [14].

Table XIII – Properties of the most common reinforcement materials used for DRAs [14].

Reinforcement	Modulus of elasticity (GPa)	Poisson's ratio	Specific heat (J/g·°C)	Thermal conductivity (W/m·K)	Coefficient of thermal expansion (10^{-6}/K)	Density (g/cm^3)
SiC	400	0.20	0.67	52	4.3	3.20
Al_2O_3	393	0.25	0.71	30	7.0	3.96
B_4C	445	0.21	0.84	26	4.78	2.51
Graphite[(a)]	8-15		0.71-0.83	25-450	1.2-8.2	2.4-2.2

(a)The properties of graphite are dependent on the grade

One of the most important factors in achieving a homogeneous distribution of particles in the matrix is the ratio of the reinforcement particle size to matrix particle size [25]. With a larger Al particle size, the SiC particles are forced between the Al particles, resulting in a clustered microstructure. Conversely, a particle size ratio closer to one yields a more homogeneous microstructure. Figure 32 shows effect of particle size distributions of SiC and Aluminum powders on the microstructure.

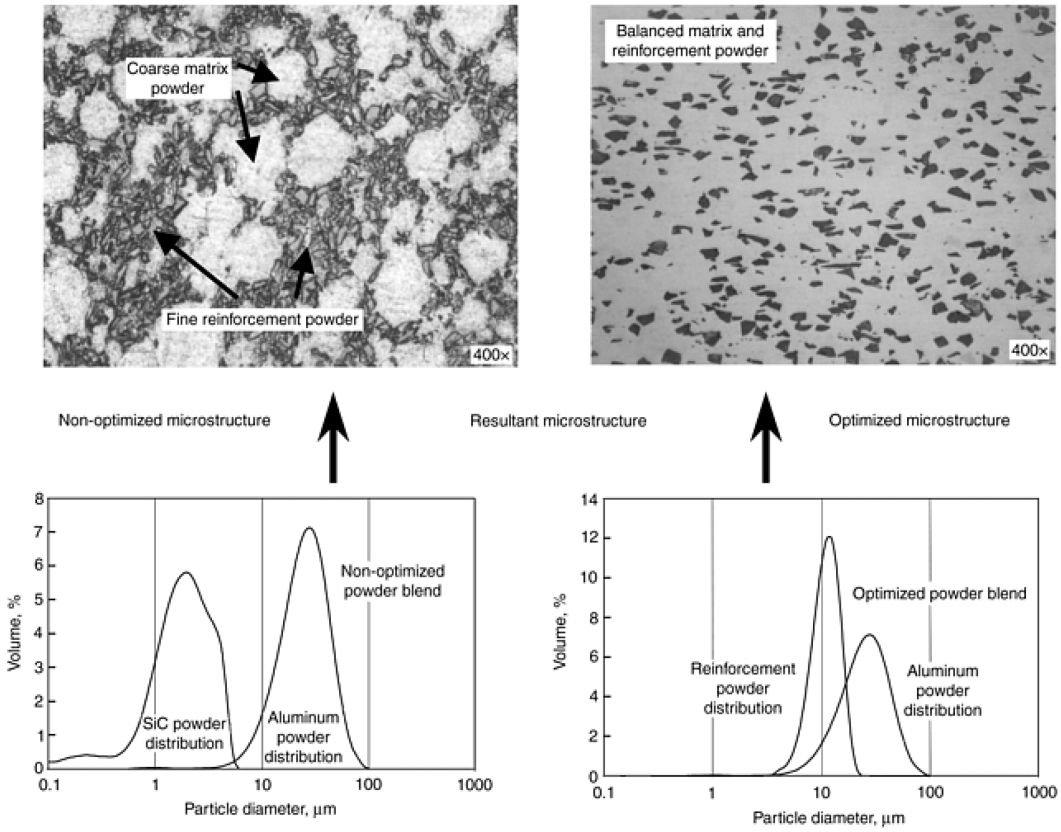

Figure 32 – Effect of particle size distributions of SiC and Al Powders on the microstructure of a 20 vol% SiC DRA [25].

Particle size and shape of the reinforcement are important factors in determining overall material properties. For instance, fatigue strength is greatly improved with the use of fine particles, and the uniform distribution of reinforcement is improved by matching the size of the reinforcement to the size of the matrix particles. The effects of particle size on other mechanical attributes are summarized in Figure 33.

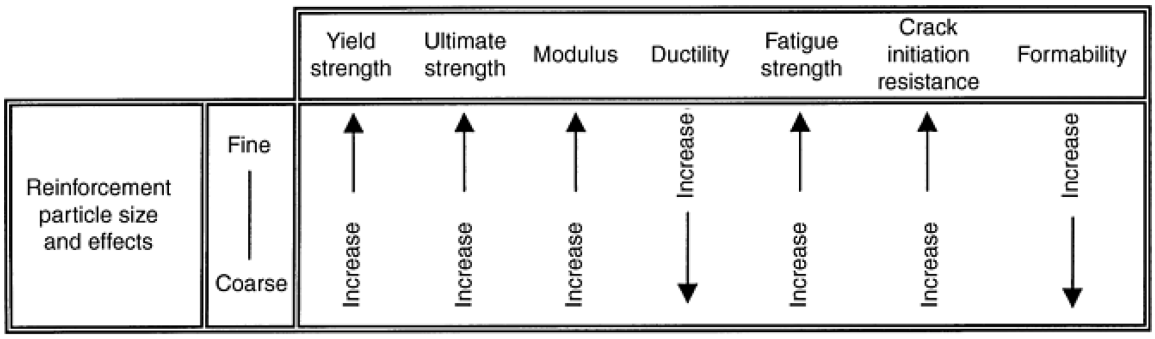

Figure 33 – Materials properties and formability as a function of reinforcement particle size [25].

5.1 Reinforcing Materials

The viability of a particular material as reinforcement for MMCs is contigent upon a number of factors. Some of the more common requirements are [26]:

- Low density
- Mechanical compatibility
- Chemical compatibility
- Thermal stability
- High Young's modulus
- High compression and tensile strength
- Good processability
- Economic efficiency

These demands can be achieved by using non-metal inorganic reinforcements. As such, ceramic particles or fibers, or carbon fibers are often used to reinforce metals. The ultimate selection of the reinforcement depends on the matrix chemistry and on the demands of the intended application. The most common DRA systems are based on SiC as the reinforcement. There are many benefits to the use of SiC, including improved stiffness, strength, thermal conductivity, wear resistance, fatigue resistance, and reduced thermal expansion. SiC powder is also low cost and low density [25]. However, the overall effects are largely dependent on the size and morphology of the reinforcement. The general effects are summarized in Table XIV [25].

Table XIV – Characteristics of commonly used reinforcements [25].

Relative size	Particle diameter (d50) μm	Advantages	Limitations
Particle reinforcements			
Fine	1.7	Greatest strength and stiffness contribution	Tendency to agglomerate
	6.5	Highest fatigue resistance Lowest resultant coefficient of thermal expansion	Blending difficulty (powder/casting) Lowered ductility High cost
Medium	9.3	Excellent balance between properties (elevated strength and good ductility) and ease of manufacturing	Necessary for high-volume reinforcement systems
	22.8		Good balance between properties and raw material costs Good balance between manufacturing ease and resultant ductility
Coarse	1700	Good wear resistance High ductility and ease of manufacturing Great for armor applications	Lowest benefit to resultant properties
Whisker reinforcements			
Fine (submicron)		Highest resultant properties in the fiber direction	Highly anisotropic resultant properties
Coarse			Greatly affected by damage (fracture during processing High cost Difficult to process

5.2 Reinforcement/Matrix interface

The interface in MMCs refers to the surface between the reinforcement and matrix across which there is a discontinuity in chemical composition, elastic modulus, coefficient of thermal expansion, and/or thermodynamic properties such as chemical potential [27]. The interface is very important in all kinds of composites as the interfacial area per unit volume is very large. The reinforcement and the matrix in most systems are also generally not in thermodynamic equilibrium, meaning that there may be an interfacial reaction to reduce the energy of the system.

The interface between two crystalline phases can be described as coherent, semi-coherent, or incoherent. A coherent interface is one where there is a one-to-one correspondence between lattice planes on the two sides of the interface. There are generally strains associated with a coherent interface due to slight differences in the lattice constants. An incoherent interface is where there is severe atomic disorder and no matching of lattice planes across the boundary. An incoherent boundary will have no coherency strains although there will be increased energy associated with the interface due to severe atomic disorder. The intermediate stage between coherent and incoherent is known as a semi-coherent interface, where some lattice mismatch between the phases exists [24]. Most of the interfaces in fiber, whisker, or particle reinforced MMCs are incoherent. These can act as efficient vacancy sinks, and provide sites for rapid diffusion, segregation, heterogeneous precipitation, and the localized formation of precipitation-free zones [24].

The most important interfacial concept in MMCs is the bonding between the reinforcement and the matrix. This is generally categorized as a mechanical or chemical bond. A mechanical bond occurs from the physical interlocking of reinforcement in the metallic matrix. Most fibers have a surface roughness or texture resulting from the fabrication process [27]. Surface roughness can

contribute to bonding only if the liquid matrix wets the reinforcement surface. Here, the matrix penetrating the crevices on the fibre surface, by liquid flow or high temperature diffusion can lead to mechanical bonding. Chemical bonding includes solid solution and/or chemical compound formation at the interface and typically leads to the formation of an interfacial reaction zone [24].

Another factor of relevance is thermal expansion given that metals generally have a higher coefficient of thermal expansion than ceramics. In this sense, the metallic matrix in the composite will shrink more than the ceramic fibre on cooling from a high temperature. This can lead to mechanical gripping of the fibre by the matrix even in the absence of any chemical bonding.

Finally, interfaces between ceramics and metals in MMCs are generally formed at high temperatures. Thus, knowledge of the chemical reaction products and, if possible, their properties are needed. It is necessary to understand the thermodynamics and kinetics of reactions such that processing can be controlled and optimum properties obtained. Chemical bonding in MMCs involves atomic transport by diffusion.

5.3 MMC Processing via P/M

MMCs can be produced by liquid, solid, or gaseous state processes. Liquid state processing techniques, such as casting and infiltration, incorporate the combination of a liquid metal matrix with the reinforcement [28]. The main drawback associated with liquid phase techniques is the difficulty in controlling reinforcement distribution and obtaining a uniform matrix microstructure. There may also be unwanted interfacial reactions between the matrix and the reinforcement that can occur at the high temperatures involved in liquid processing [24]. To avoid such drawbacks, solid phase processing techniques such as P/M are used. There exist

many variations on the processing MMCs by the P/M route. This can involve cold isostatic pressing and sintering, hot pressing, or cold uniaxial pressing plus sintering. These steps can then be followed by extrusion or forging techniques [28].

Conventional powder processing involves the cold uniaxial pressing and sintering to fabricate particle or whisker reinforced MMCs. The first step to produce MMCs by this method is to blend the matrix and the reinforcement powders to produce a homogeneous distribution. The blending stage is followed by cold pressing to produce what is called a green compact, which is about 80% dense and can be easily handled [24]. The green compacts are then sintered to produce a high density material with a homogeneous distribution of the reinforcement in the metal matrix. Although this process is relatively simple, one of the problems with bonding metallic powder particles, such as Al, to ceramic particles is the oxide layer present on the Al particle surface. This layer can prevent direct metal to ceramic contact and diminish bond quality. However, this issue is often resolved by the inclusion of forging or extrusion processes to break up the oxide layer and facilitate improved bonding [16].

Chapter 6.0 Hot Deformation of an Al-Cu-Mg Powder Metallurgy Alloy

R.E.D. Mann[1], R.L. Hexemer Jr.[2], I.W. Donaldson[2], and D.P. Bishop[1]

1 – Department of Process Engineering and Applied Science, Dalhousie University, 1360 Barrington St., Halifax, Nova Scotia, Canada, B3J 2X4

2 – GKN Sinter Metals LLC, 3300 University Drive, Auburn Hills, USA, 48326

Status: Submitted to *Material Science and Engineering A*

The following experimental procedures, analysis and discussions were completed by R.E.D. Mann, with reviewer and editorial roles played by the subsequent authors.

Abstract

The effort to improve automobile efficiency has potential economic and environmental advantages. The field of aluminum powder metallurgy (P/M) is of particular interest as the implementation of such technologies to produce parts can offer the combination of a weight savings and the economic advantages of near net shape processing. However, one of the hurdles to overcome in the field of P/M is the presence of porosity in the sintered product. To reduce the presence of this attribute, sintered materials can be hot forged to full density. In this study, the forging response of a novel aluminum-copper-magnesium P/M alloy, P/M 2324, was studied in comparison to its wrought counterpart AA2024. Modelling of the peak flow stress required in the P/M and wrought alloys yielded very similar results with both materials adhering to a standard Zener-Hollomon curve fitting approach. Rotary swaging was also completed to assess the impact of hot work on the P/M material. These findings confirmed that full density could be achieved in P/M 2324 and that the concomitant tensile properties were significantly higher for the swaged P/M system. Microstructurally, it appeared that the principal secondary phase in P/M 2324 was θ (Al_2Cu) whereas the S phase (Al_2MgCu) was pronounced in the wrought system.

6.1 Introduction

Sintered aluminum P/M alloys are an attractive material for the production of vehicle components in the automobile industry. They offer potential economic and environmental advantages due to the low specific gravity and high strength/weight ratio of aluminum, as well as fabrication advantages associated with the P/M process. For example, aluminum P/M is often used to produce the camshaft bearing caps or “cam caps” found in combustion engines. Such components, historically produced by die casting, are precision parts as they ensure proper alignment of a camshaft when bolted to the block. Die cast cam caps do not meet the required dimensional tolerances and must be heavily machined prior to use. Conversely, P/M production methods offer tighter dimensional tolerances to avoid the majority of expensive machining operations.

To date, the vast majority of aluminum P/M products have been produced from a singular alloy system – AC2014 [15]. The frequent use of this alloy is driven by availability rather than exemplary mechanical performance. An expansion in the number of commercially available aluminum P/M alloys has recently emerged as a core thrust of study for many researchers. This has led to the development of new alloys in the 7xxx [29, 30], 4xxx [21, 31], and most recently 2xxx [6] series. In the latter, a new alloy designated as P/M 2324 was developed. This alloy has nominal chemistry of Al-4.4%Cu-1.5%Mg-0.2%Sn and is known to have improved mechanical properties when compared to AC2014. Such gains come from the ability to achieve an exceptionally high sinter density and the use of a bulk chemistry that favours the formation of S-type precipitates [2].

Although the newer alloys offer major strength improvements, the presence of a small amount of residual porosity in the sintered product remains a hurdle to overcome for many applications. In ferrous products, this feature is often eliminated by forging the as-sintered materials [4]. This

is known to increase all mechanical properties significantly with the most prominent gains realized in yield strength, ductility, and fatigue life. Hence, P/M forging is now a widely used method of producing steel parts of high density for the automotive industry for high stress applications such as connecting rods and clutch races [5]. It is now known that hot forging of sintered aluminum preforms can also impart significant mechanical gains. For example, LaDelpha et. al. showed a 50% increase in tensile properties from the sintered to the hot deformed condition in a P/M alloy with a composition similar to AA4032 [21]. The properties of this alloy in the press/sinter/swage condition effectively matched those of its wrought counterpart. In other works, MacAskill et. al. have demonstrated that the fatigue performance of the aluminum P/M alloy Alumix 431D (chemically equivalent to wrought AA7075) was improved dramatically after hot working [22]. Tangible gains have also been realized in Al-Si-Cu-Mg systems [31].

The objective of this work was to undertake a comprehensive study on the effects of hot deformation on the emerging alloy P/M 2324. Here, a forgeability study of it and its wrought counterpart AA2024 was completed. Peak flow stress data were acquired under different combinations of temperature and strain rate using a thermal-mechanical test frame. The Zener-Hollomon relationship was then used to model the peak flow stress behaviour of the two alloys. Finally, the impact of hot work in mechanical properties was quantified through hot swaging trials.

6.2 Materials

In this study two materials were utilized – sintered billets of P/M 2324 and wrought counterpart AA2024 in the form of an extruded rod. The nominal and measured compositions of these alloys are shown in Table XV. P/M 2324 was a blend of several powders including air atomized aluminum, a 50/50 weight percent aluminum-copper master alloy, atomized magnesium, and atomized tin [2]. These powders were blended in-house to attain the required chemistry. Licowax C was also added to the blend to provide lubrication during the compaction process. The composition of P/M 2324 was largely comparable to the wrought counterpart with two notable exceptions – the addition of tin and omission of manganese. Tin was added as it is known to improve the density and mechanical properties of the alloy [1]. Manganese was omitted as it is known to have a negative impact on powder compaction.

Table XV – Comparison of the nominal and measured compositions of the alloys studied.

		Al	Cu	Mg	Mn	Sn	Fe
AA2024	nominal [32]	Bal.	4.4	1.5	0.6	--	0.5
	measured	Bal.	4.53	1.48	0.64	--	0.27
P/M 2324	nominal	Bal.	4.4	1.5	--	0.2	--
	measured	Bal.	4.30	1.39	--	0.19	0.09

6.3 Methodology

To study the forging response of P/M 2324 and the wrought counterpart AA2024, a combination of experimental and modeling work was completed. Specific details on these techniques are provided below.

6.3.1 Experimental Techniques

Initially, P/M samples of several geometries were fabricated. This included cylindrical specimens for hot compression tests, charpy bars for hot swaging trials, and dog bones for tensile tests. [33] The latter were used exclusively to assess the tensile properties of P/M 2324 in the as-

sintered (pre-forged) condition. All bars were fabricated through a press and sinter approach. In the first step, raw powder was uni-axially die compacted at 400 MPa using a Satec Systems Model 5594 -200HVL 1000kN load frame with a floating die tooling arrangement. The resulting green bodies were then sintered industrially in a continuous mesh belt furnace at 610°C for 20 minutes under an atmosphere of flowing nitrogen. Sintered cylinders were then fully machined to achieve the required dimensional tolerances (25mm tall, 12 mm diameter). Identical cylinders of wrought 2024-T3 were machined from extruded rod stock.

Hot compression tests were completed on a Gleeble® 1500D thermal-mechanical testing apparatus manufactured by Dynamic Systems Incorporated. This machine allowed for accurate temperature and strain rate control throughout compression tests conducted in accordance with ASTM E209 [34]. In all tests a thermocouple was welded to the cylindrical specimen for temperature control purposes and a C-gauge diametrical extensometer was used to measure the true strain. Tests were completed at true strain rates of $0.005s^{-1}$, $0.05s^{-1}$, $0.5s^{-1}$, and $5s^{-1}$ to a maximum true strain of 75%. The alloys were tested at a number of temperatures from 350°C to 500°C.

Next, rotary swaging of P/M 2324 was completed in effort to simulate the effects of hot forging. This process used an alternating blow swager with a four die arrangement. Swaging was performed on sintered charpy bars that were machined round to a starting diameter of 12 mm. Machined bars were then preheated to 490°C for 20min prior to swaging through three sets of dies (10.92mm, 9.65mm, and 8.64mm). Swaged rods were then heat treated to the T6 condition (solutionize 495°C, water quench, age 10hr 190°C) and machined into tensile bars. Extruded rods of wrought AA2024 were subjected to the same heat treatment and machining procedure. Tensile testing was then completed on specimens with the same frame employed

for powder compaction but when equipped with a 50kN load cell. All bars were loaded at a rate of 2 MPa/s. An epsilon model 3542 extensometer remained attached to the specimen through the point of fracture.

Microstructural analyses were premised on a combination of optical metallography, scanning electron microscopy (SEM), and x-ray diffraction (XRD). All samples prepared for optical metallography were vacuum cold mounted in Buehler® Epo-Thin® low viscosity two part epoxy, ground, and polished. The samples were first planed using a 240 grit silicon carbide. Following this, they were polished in stages using cloth pads and diamond suspensions (9 um, 3 um, 1 um) and finished with a colloidal silica polish. Optical metallography was done using a Unitron optical microscope equipped with a micrometrics digital camera. A Hitachi S-4700 cold field emission SEM was used to assess the fracture surfaces of the tensile specimens as well the polished microstructure of the materials studied. An Oxford Inca Energy-dispersive X-ray spectroscopy (EDS) system was used to assess the chemical composition of select phases of interest. The SEM was operated with an accelerating voltage of 20 kV and a beam current of 10 mA. A Bruker AXS D8 Advance XRD unit equipped with a copper x-ray source was used to identify the principal phases present in the materials. The system was operated with a tube voltage and current of 40 kV and 40 mA respectively. The resultant diffraction patterns were analyzed using EVA™ analytical software and compared with established diffraction patterns based on peak positions and relative intensities.

6.3.2 Zener-Hollomon Modeling

One of the main process parameters for any forging operation is knowledge of the flow stress required to deform the material. Although this is largely based on the product geometry and the effects of lubricants, information on the peak compressive flow stress can be valuable as it is important to understanding the stress required to successfully forge a given component. Given

that peak flow stress is dependent on strain rate and temperature, the semi-empirical Zener-Hollomon relationship, Equation 4, is often used to model any given combination of these test parameters [35].

$$Z = Asinh(\alpha\sigma)^n = \dot{\varepsilon}e^{Q/RT} \quad \textbf{Equation 4}$$

Where,

Z	= The Zener-Hollomon parameter
A, n	= Material constants
σ	= Peak flow stress (MPa)
α	= Stress multiplier (MPa^{-1})
έ	= Strain rate (s^{-1})
Q	= Activation energy of deformation ($kJ\ mol^{-1}$)
R	= Ideal gas constant ($kJ\ mol^{-1}\ K^{-1}$)
T	= Deformation temperature (K)

For this equation to be effectively used, the variables α, Q, A, and n must first be solved from experimental data on hot compression. The first variable solved for is the stress multiplier α. Using a computer program, a long string of possible values for α was inserted into the log(sinh(ασ)) term of the equation. Slopes of log(*έ*) versus log(sinh(ασ)) were then compared. In accordance with the work of McQueen et al., Bardi et al., and Zhang et al. [35-37] the value that produced the most parallel trends for each material was taken to be the stress multiplier α. The average value of the slopes at their most parallel orientation was then taken as the numerical value n. Plots of log(sinh(ασ)) versus T^{-1} were then constructed and the average slope of these trends was termed s. Following from the Zener-Hollomon equation, the activation energy of hot working (Q) was then approximated by the product of n, s, and the ideal gas constant R as per Equation 5.

$$Q = nRs$$ **Equation 5**

Where;

Q = Activation energy of deformation (kJ mol^{-1})
R = Ideal gas constant (kJ mol^{-1} K^{-1})
n,s = Material constants

With the acquisition of the constants Q, α, and n for each alloy, the values were then substituted into Equation 4 to yield an average value for A. Having solved for all the necessary variables, the application of the Zener-Hollomon approach could then be realized by solving for the approximate peak flow stress for the alloys for any combination of temperature and strain rate both within and beyond the matrix of combinations assessed experimentally [31].

6.4 Results and Discussion

Hot compression testing was conducted so as to acquire true compressive stress versus true strain data. Such tests were completed at a variety of strain rates and temperatures. The densities and microstructures of the samples were analyzed and compared to those in the non-deformed state. A model was then constructed for determining the peak flow stresses as functions of temperature and strain rate. Finally, tensile properties of wrought AA2024 T6 as well as P/M 2324-T6 in the as-sintered and hot swaged conditions were determined.

6.4.1 P/M Processing

To verify that P/M processed bars were sintered in a manner consistent with prior findings, the sintered density, dimensional change and microstructure of the as-sintered materials were assessed. The resultant cylinders achieved a sintered density of 2.75 g/cc (99.5% of the full theoretical) and experienced dimensional changes in the height and diametrical dimensions as shown in Table XXIII. The appreciable shrinkage of the specimens was consistent with the high sintered density observed in prior findings [1].

Table XVI – Average dimensional change in sintered cylinders of P/M 2324.

Height %	Diameter %
-1.78 +/- 0.13	-2.16 +/- 0.28

The as-sintered microstructure of P/M 2324 is shown in Figure 34, as well as the microstructure for wrought AA2024 T6. The presence of porosity in the sintered alloy is shown in the micrograph by the black regions. Although the alloy was very dense, it is known that even a small amount of porosity can have negative effects [38]. The complete elimination of this attribute is central to all P/M forging processes, and likewise, critical to this study as well. The optical microstructure of the wrought alloy differed considerably. For one, there was no observable amount of porosity present. Another was the presence of a dispersoid phase in the wrought alloy seemingly absent from the P/M system. Further details on these observations are provided later in this study.

6.4.2 Hot Compression Tests

Hot compression tests were performed on P/M 2324 and AA2024 for numerous combinations of temperature and strain rate. Examples of the resultant plots are shown in Figure 35 for the alloys upset forged at a temperature of 450°C. These data show that during compression, both materials exhibited a maximum true compressive stress at a low strain followed by dynamic flow softening. Flow softening is a common characteristic of true stress–true strain curves for many hot deformed alloys. Causes for this can be deformation heating and microstructural instabilities in the material, such as dynamic recrystallization, texture formation, dynamic precipitation, and precipitate dissolution [39].

The peak flow stresses measured for all temperature/strain rate combinations are summarized in Table XXIV and Table XVIII. The flow stress data of the two alloys was found to be similar and

common trends in the data also persisted. In this sense, the peak stress was found to increase with rising strain rate but decrease with rising temperature. The peak flow stress for P/M 2324 was greater for the higher temperatures (450°C) than those for AA2024 but the reverse was observed for the lowest temperature considered (350°C).

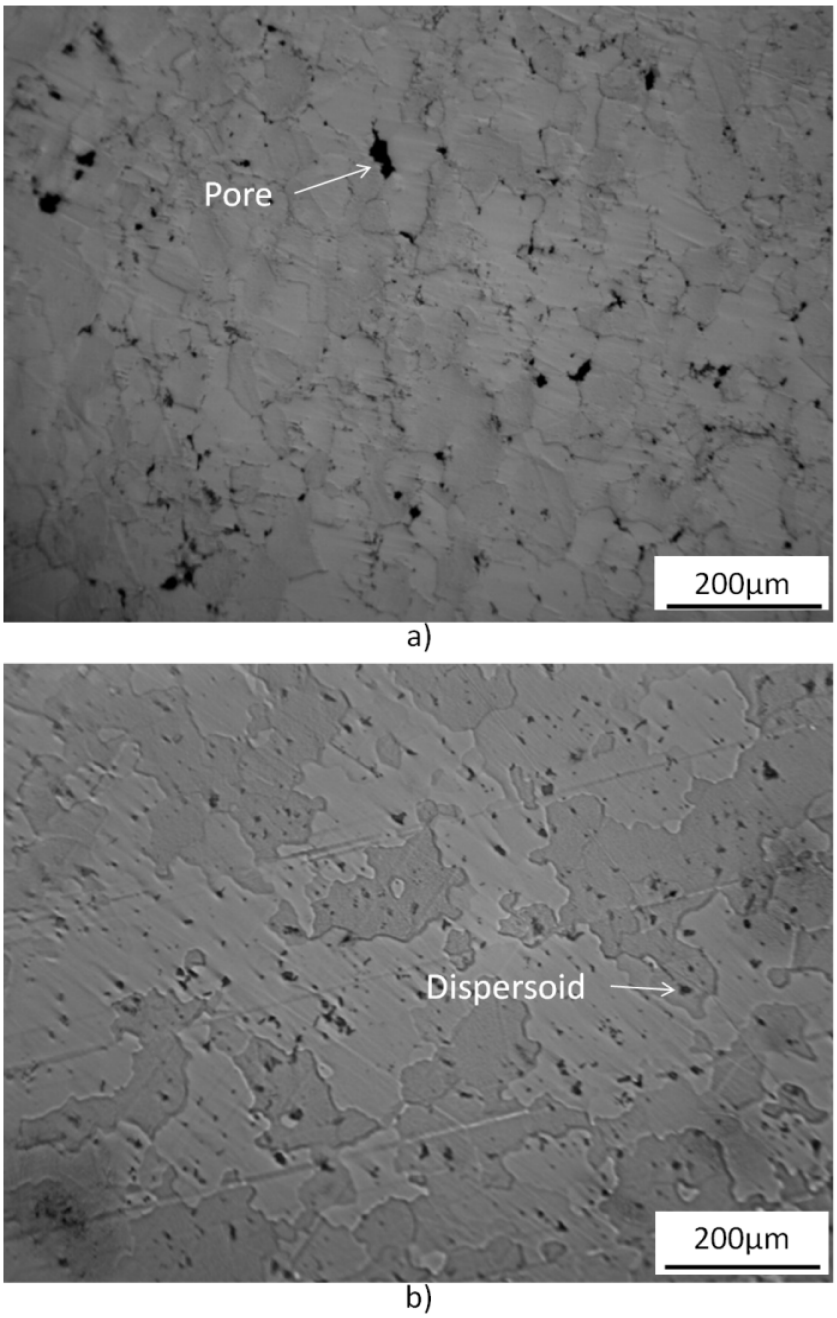

Figure 34 – Optical micrographs of (a) P/M 2324 T6 as sintered and (b) wrought AA2024 T6.

Hot deformation studies have previously been completed on the wrought alloy AA2024 by Charpentier and Dwivedi [40, 41]. Comparing their data to the values for peak compressive flow stress in this study gives very similar results. Exact experimental values were not able to be compared as different strain rates and temperatures were used in the studies but were quite similar when approximated.

As noted in section 4.1, the elimination of residual porosity in P/M 2324 was a key goal of this forging study. As such, the densities of forged P/M cylinders were measured. In all cases, it was found that a density of 2.77 g/cc was achieved, corresponding to the full theoretical density of the alloy. This was a promising result as it showed that full density could be achieved upon hot compression of the P/M alloy at all of the strain rates and temperatures considered.

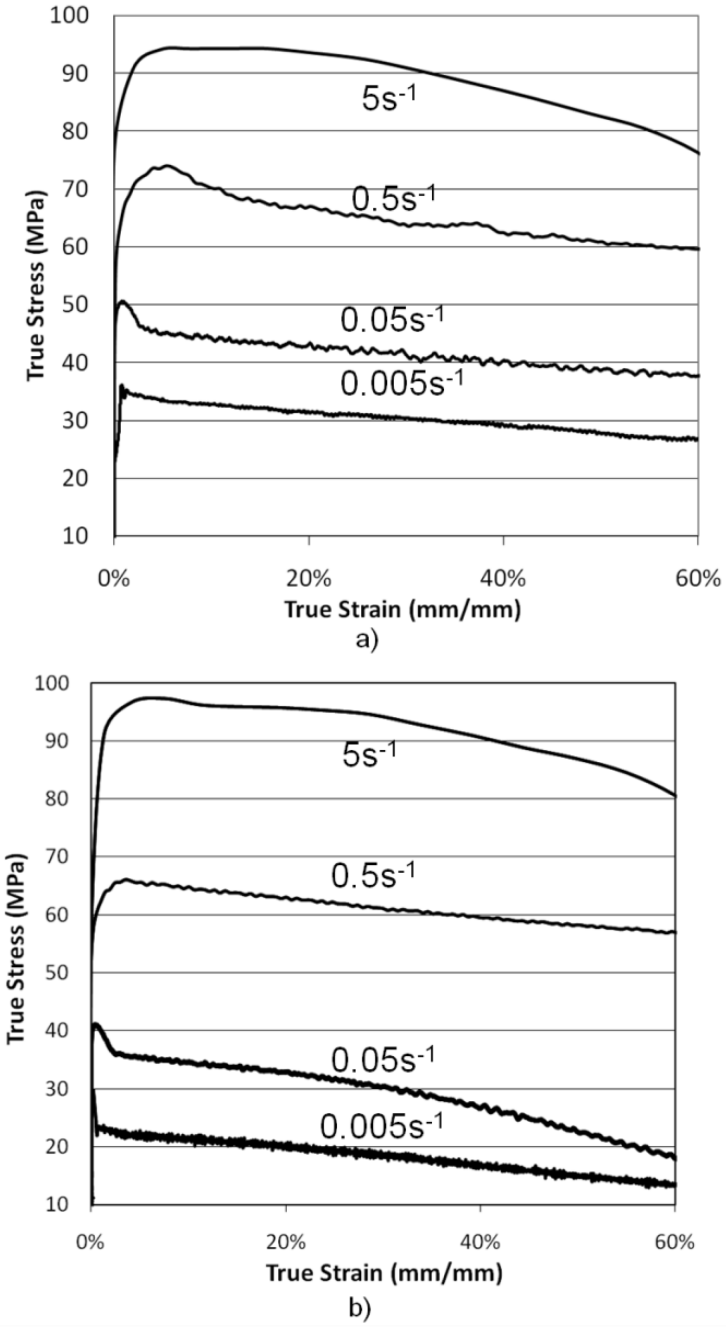

Figure 35 – True compressive stress/strain curves completed at 450°C (a) P/M 2324 and (b) wrought AA2024.

Table XVII – Peak flow stress (MPa) data for P/M 2324 as related to deformation temperature and strain rate.

	True strain rate (s^{-1})			
Temperature (°C)	0.005	0.05	0.5	5
350	111.3	126.0	145.6	175.1
400	82.0	82.4	106.1	120.1
425	69.1	70.6	86.3	110.6
450	44.8	50.7	74.1	94.3
475	38.5	44.2	54.4	76.5

Table XVIII – Peak flow stress (MPa) data for AA2024 as related to deformation temperature and strain rate.

	True Strain Rate (s^{-1})			
Temperature (°C)	0.005	0.05	0.5	5
350	122.7	131.1	162.7	190.6
400	60.6	74.9	91.7	125.0
450	33.2	45.0	66.1	97.3
500	29.8	41.1	53.5	66.5

6.4.3 Flow Stress Analysis (Zener-Hollomon)

In the next phase of work experimental data were used to model the peak flow stress as a function of strain rate and temperature. Initially, values of α were solved for using a computer program. The average slope of the trend lines for log(ε̇) vs. log(sinh(ασ)) was then taken as the material constant *n* while the average slope of the trend lines in log(sinh(ασ)) vs. T^{-1} was taken as the numeric value of *s*. Next, the activation energy of deformation, *Q*, was solved for using Equation 5. With values for *Q*, α, s, and *n* identified for each alloy, an average value for ln(A)was determined using Equation 4. Finalized values for the wrought and P/M alloys are shown in Table XXV. Important values to compare are α, n, and ln(A). The smaller these values, the larger the peak flow stress for a given temperature and strain rate. All of the values were slightly higher for P/M 2324. However, the opposite holds true for the activation energy (Q) in that a larger value will give a larger peak flow stress. In this case, all values were larger for P/M 2324;

this invoked an offsetting effect of such that similar trends in peak flow stress were achieved for both materials.

Table XIX – Comparison of the Zener-Hollomon parameters calculated for P/M 2324 wrought and AA2024.

	P/M 2324	AA2024
α	0.0165	0.0125
n	7.28	6.75
S	6030	5412
Q	365	304
ln(A)	57.0	49.7

Having identified suitable values for all constants, these data were then inserted into Equation 4 enabling a direct comparison between calculated and experimental findings as shown in Figure 36, with the points representing experimental points and the lines corresponding to the calculated values. It was noted that the values fit the modeled plots well validating the approach. Although peak flow stress functions were comparable between the materials, certain differences persevered. For instance, the peak flow stresses for P/M 2324 were higher than the wrought counterpart at elevated temperatures (t=400°C, 450°C), yet this situation was then reversed at the lowest temperature considered (350°C).

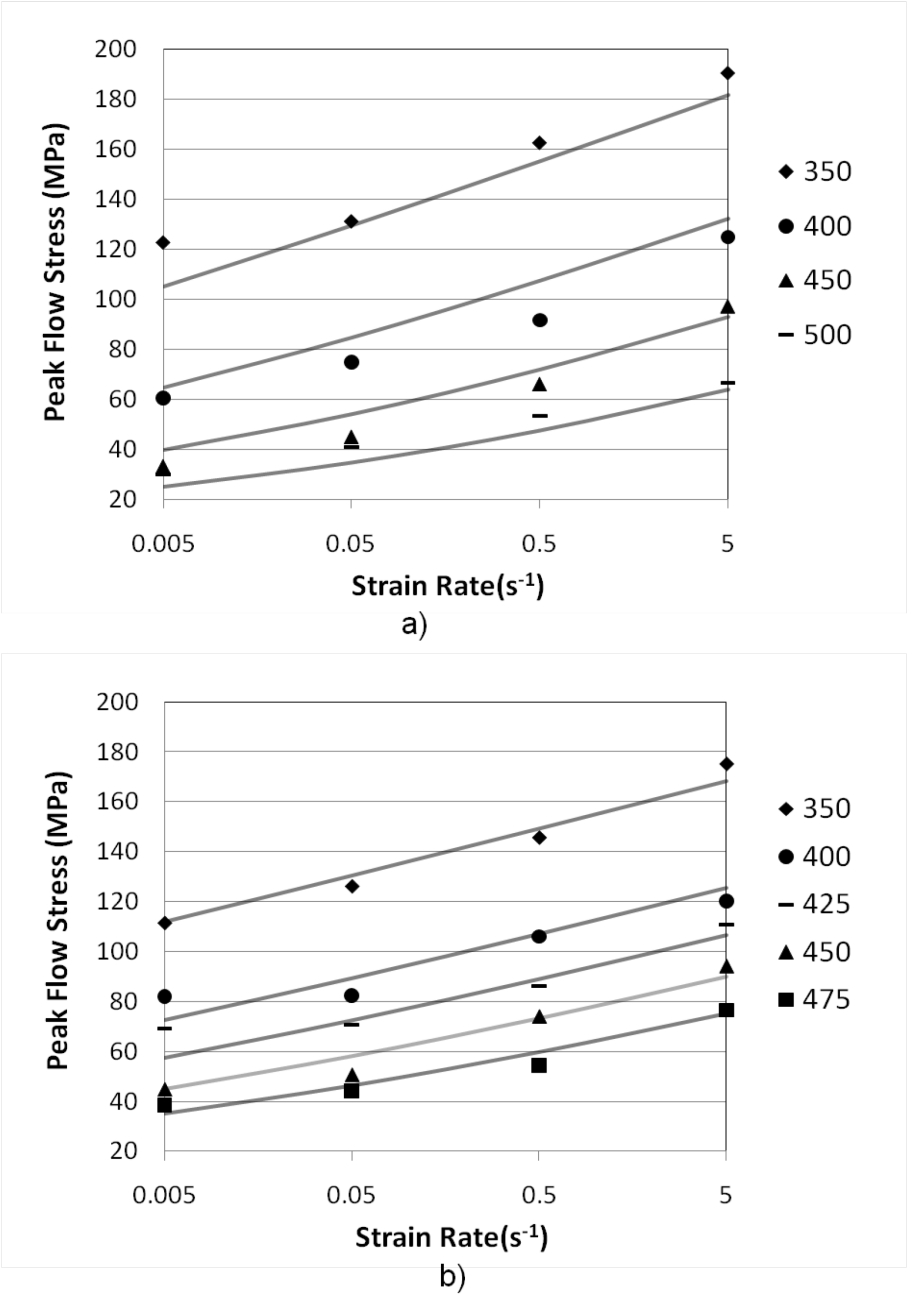

Figure 36 – Comparison of experimental and calculated peak flow stress data for (a) wrought AA2024 and (b) P/M 2324.

6.4.4 Effects of Hot Deformation

Rotary Swaging of P/M 2324 was then performed to simulate hot forging procedures on bars large enough to extract tensile specimens. Based on the thermal mechanical data, temperature and strain rate did not have a significant effect on densification. Conversely, these parameters had an acute affect on peak flow stress with higher temperatures and lower strain rates favouring a reduced value. In this sense, it was desirable to swage bars at the highest temperature possible but avoid the formation of a liquid phase. This is a key concern given that the propensity for cracking increases significantly if even a small fraction of liquid phase exists. Hence, swaging was completed at the solutionizing temperature of the alloy (495°C) in the hopes of achieving the best results. This temperature was chosen as minimal force would be required to deform the material and liquid phase formation would be avoided. Under these conditions fully dense materials were realized consistent with prior measurements on the test cylinders upset forged in the gleeble.

Tensile test results between the alloys in various stages of processing are shown in Figure 37. Improvements in all properties were shown from the as-sintered to the sintered and swaged conditions of P/M 2324 heat treated to the T6 condition. For example, a ~25% increase in UTS and YS was observed as well as a 3-fold increase in elongation. These gains occurred to a level whereby hot worked P/M 2324 exhibited superior UTS and YS relative to wrought 2024 but continued to offer reduced ductility. All of these trends in mechanical properties could be explained by a combination of factors. One was the obvious removal of residual porosity given that this feature is known to have a damaging effect on all tensile properties [4, 21, 22, 31]. The second factor pertained to the breakup of the semi-continuous oxide network that would have been present in the as-sintered product. The origins of this feature stemmed from the use of air atomized aluminum powder on which a thin oxide shell would have existed [42]. When

sintered, this oxide shell would have reacted with magnesium to form spinel ($MgAl_2O_3$) and persevered in the final sintered product as a semi-continuous network [43]. Like porosity, this attribute is also known to invoke reduced tensile ductility. However, as a form of ceramic addition, it can also impart a mild strengthening effect so as to increase YS and UTS once broken up into fine discrete particles. Hot swaging eliminated residual porosity and should have disrupted the spinel network as well. The fully dense product would have then performed as a metal matrix composite material of sorts so as to offer an advantageous YS and UTS over both of the other materials in combination with an intermediate ductility.

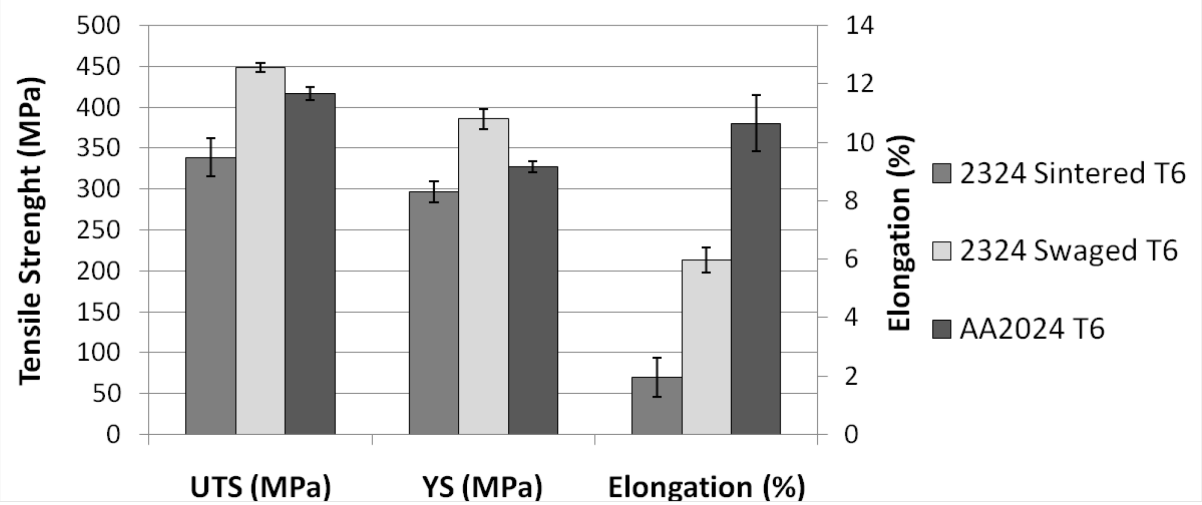

Figure 37 – Tensile data of P/M 2324 in the sintered and swaged conditions as well as wrought 2024. All materials heat treated to the T6 temper.

The fracture surfaces of the tensile tests are shown in Figure 38. The differing amounts of ductility are clearly evident in the micrographs. Ductility is generally demonstrated in the form of micro-void coalescence in the fracture surface, whereas a brittle fracture will have more angular, flat facets. The progressive increase in ductility can be seen in the micrographs. In this sense, the fracture surface of as-sintered P/M 2324 contains relatively few microvoids yet this feature was far more pronounced in the hot swaged version wherein tensile ductility had tripled

(Figure 37). The wrought alloy had even larger and more numerous microvoids with a reduced presence of flat facets. This too was consistent with ductility measurements given that it exhibited the highest average value (~11%).

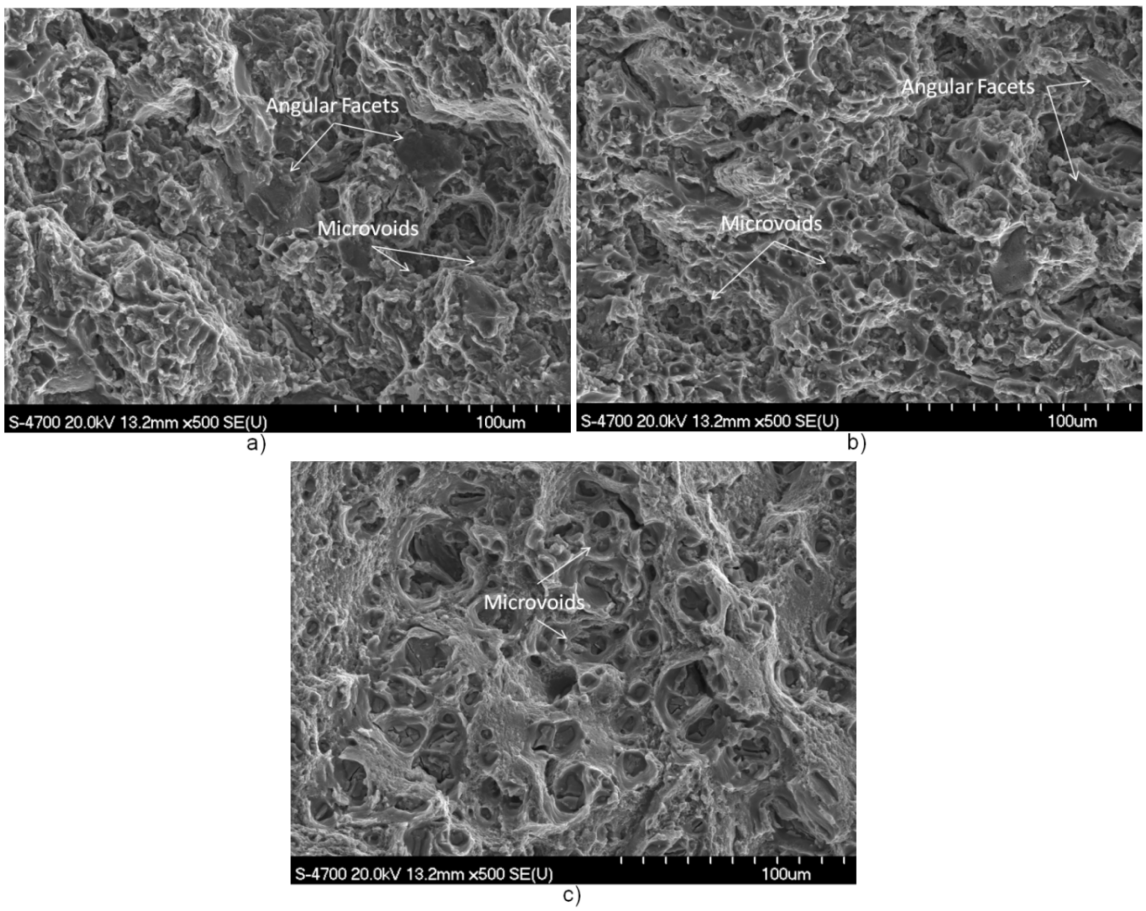

Figure 38 – Fracture surfaces (a) as-sintered P/M 2324 T6, (b) sintered and swaged P/M 2324 T6, and (c) wrought AA2024 T6.

6.4.5 Microstructure Characterization

In the final phase of research, detailed microstructural analyses were completed on the materials of interest. An SEM micrograph of 2324 T6 in the as sintered condition is shown in Figure 39. The chemical compositions of the marked points on the image as measured by EDS techniques are presented in Table XX. There was found to be an aluminum rich matrix and a secondary phase(s) present at the aluminum grain boundaries. From EDS, the latter was found to contain high concentrations of aluminum and copper with smaller amounts of magnesium and tin. From XRD (Figure 40) it was confirmed that α-aluminum and θ ($CuAl_2$) were present in the alloy. XRD also implied that tin had likely reacted with magnesium to form Mg_2Sn although the match was not as definitive as that for θ.

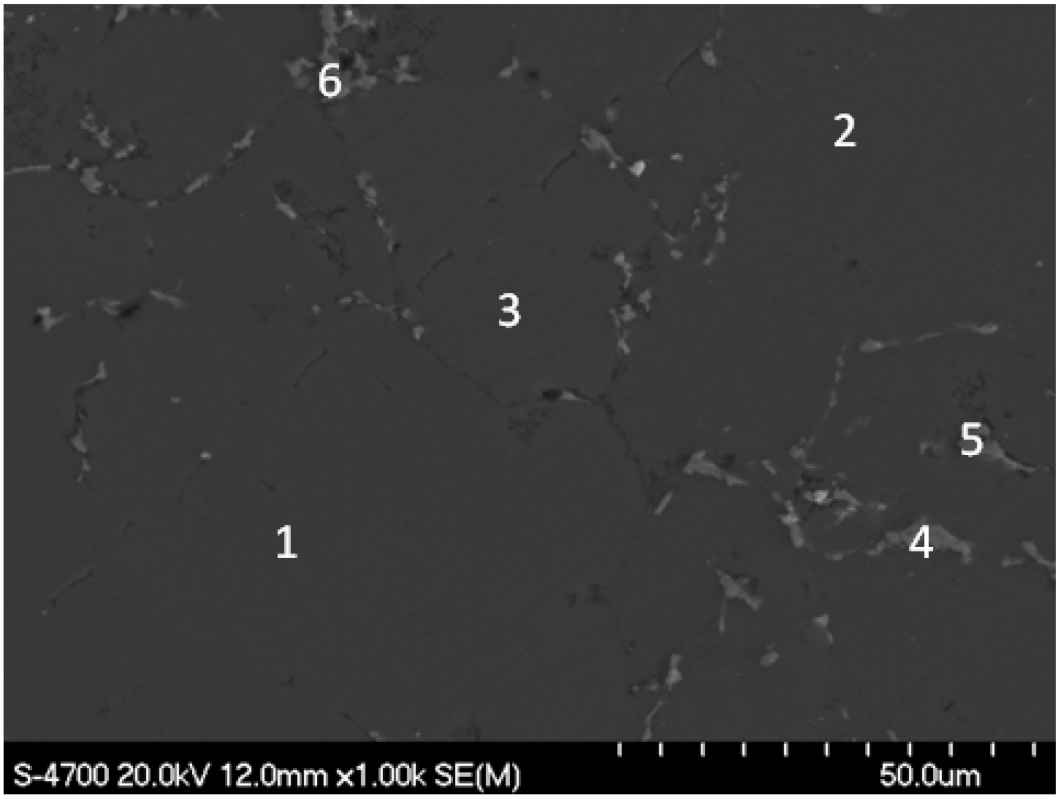

Figure 39 –SEM image of P/M 2324 T6 in the as sintered condition.

Table XX – EDS measurements recorded at the point locations shown in Figure 39 (w/o).

Phase	Location	Al	Cu	Mg	Sn
Aluminum Matrix	1	93.94	4.65	1.41	--
	2	94.18	4.48	1.34	--
	3	95.20	3.57	1.23	--
Al-Cu-Mg Phase	4	52.22	43.60	4.18	--
	5	68.38	27.26	4.37	--
	6	56.73	38.64	4.26	0.36

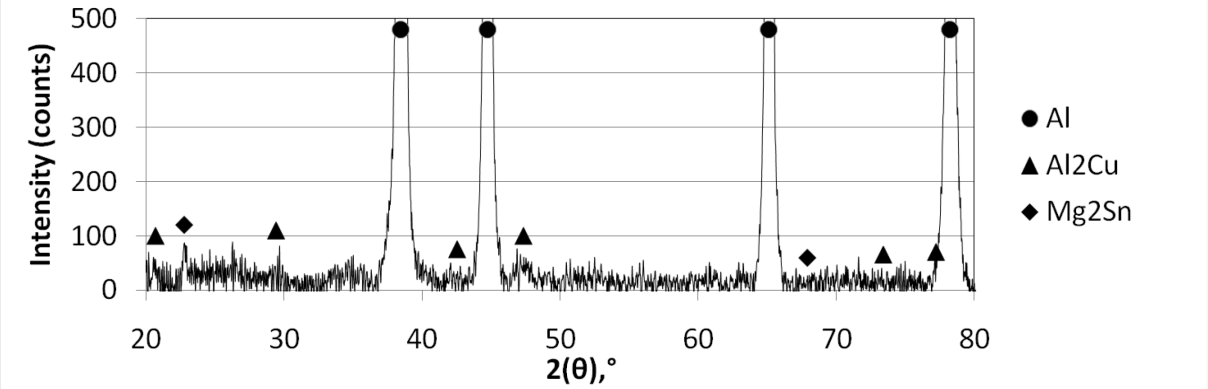

Figure 40 – XRD spectrum acquired from P/M 2324 T6 in the as sintered condition.

An SEM micrograph of hot swaged 2324 T6 is shown in Figure 41 with the corresponding EDS point compositions given in Table XXI. The effects of swaging on the microstructure of the alloy that can be seen in the micrograph include texture in grain orientation and the elimination of porosity. The dominant phases present in the swaged alloy were the same as those observed in the sintered alloy, α-aluminum Al_2Cu and Mg_2Sn, based on XRD data (Figure 42). The occasional presence of impurities was also noted with varying amounts of iron, nickel and silicon observed in select features.

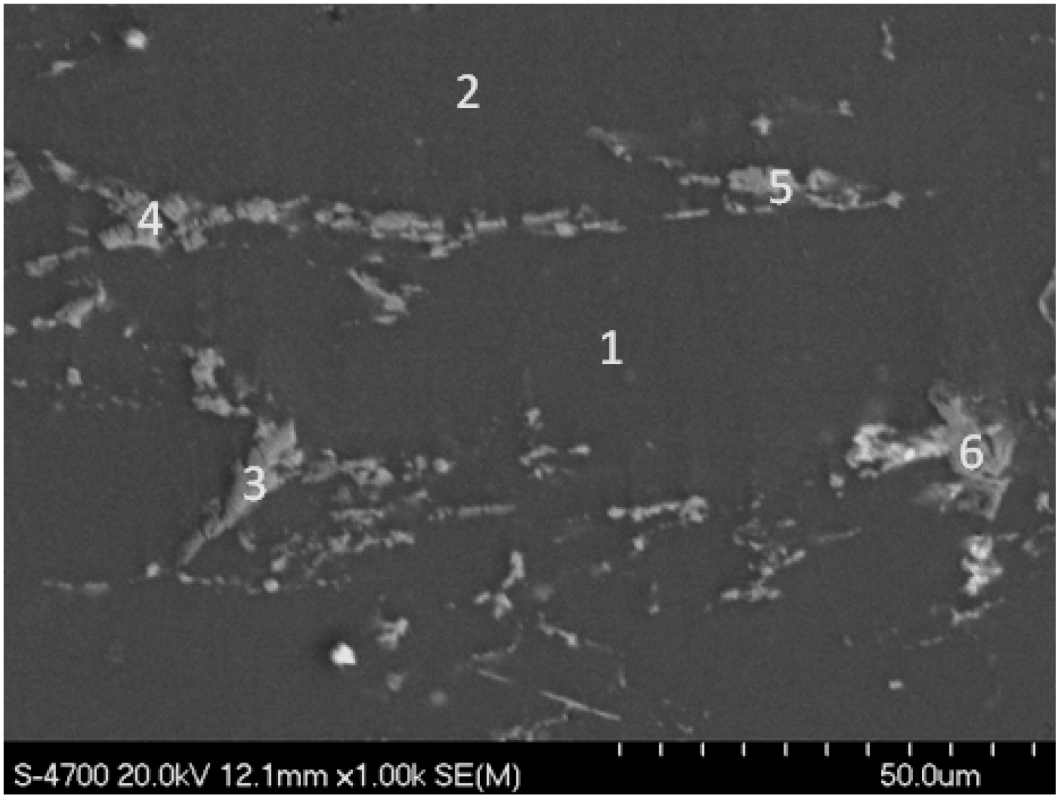

Figure 41 –SEM image of P/M 2324 T6 in the swaged condition

Table XXI – EDS measurements recorded at the point locations shown in Figure 41 (w/o).

Phase	Location	Al	Cu	Mg	Fe	Sn	Ni	Si
Aluminum Matix	1	94.53	4.52	0.95	--	--	--	--
	2	94.65	4.31	1.04	--	--	--	--
Al-Cu-Mg Phase	3	83.41	11.15	5.07	--	0.37	--	--
	4	66.53	23.94	3.88	4.61	--	0.36	0.68
	5	70.22	19.24	2.55	7.63	--		0.36
	6	49.22	33.10	1.14	15.46	0.54	0.54	--

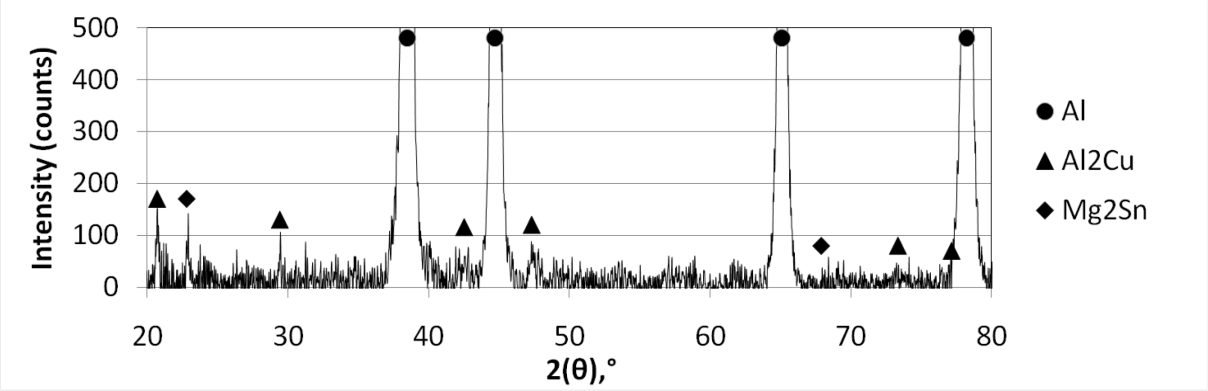

Figure 42 – XRD spectrum acquired from 2324 T6 in the swaged condition.

The microstructure of AA2024 T6 is shown in Figure 43. This alloy appeared to have two distinct secondary phases. The larger more irregular phase shown in the micrograph (points 3 and 4) contained manganese, iron, aluminum, and copper (Table XXII). This phase coincided with Al_7Cu_2Fe with some iron replaced by manganese. Iron and manganese are close chemically which leads one to believe that $Al_7Cu_2(Fe,Mn)$ could be the phase identified. The smaller more rounded phase (points 5 and 6) contained aluminum, copper, and magnesium. This phase appeared be the S phase based on the chemical assay. From the XRD plot in Figure 43, the presence of Al_7Cu_2Fe and the S phase (Al_2CuMg) were confirmed. Theta (Al_2Cu) was also found to be present in the alloy via XRD. $Cu_2Mn_3Al_{20}$ is known to be a dispersoid phase generally present in the AA2024 alloy but was not found in this material [44]. This could have been caused by the higher iron content which promoted the preferential formation of $Al_7Cu_2(Fe,Mn)$ instead.

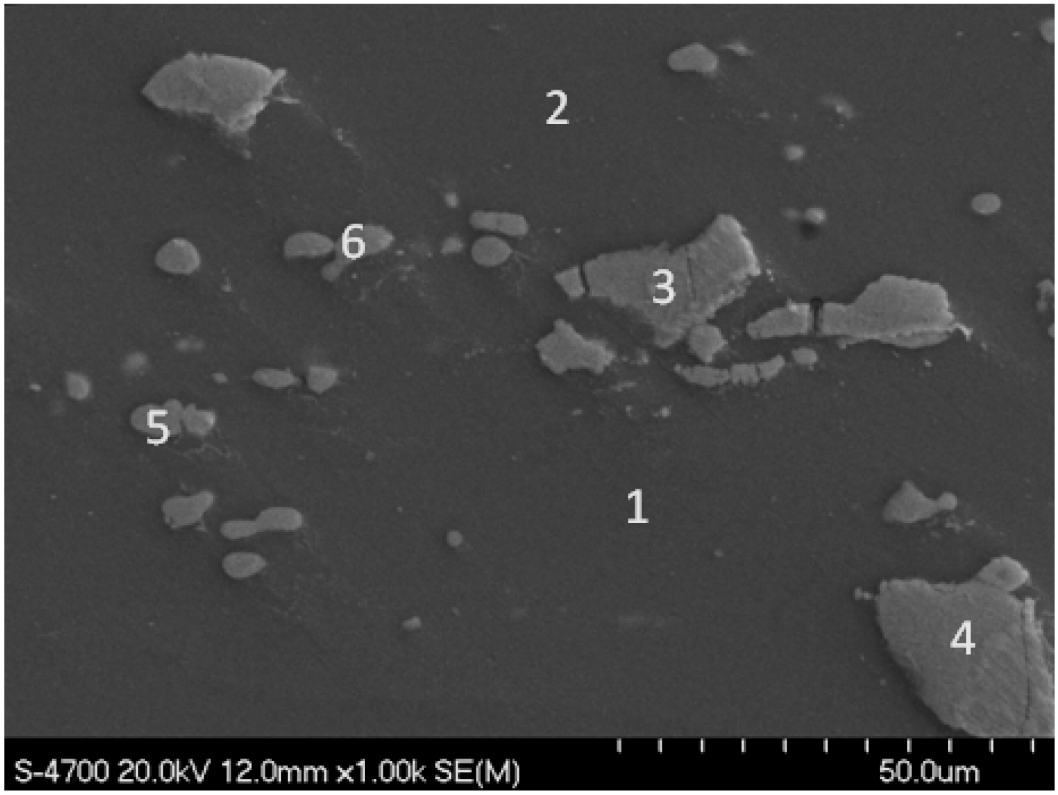

Figure 43 – SEM image of wrought AA2024 T6.

Table XXII – EDS measurements recorded at the point locations shown in Figure 43 (w/o).

Phase	Location	Al	Cu	Mg	Mn	Fe
Aluminum Matrix	1	93.50	4.47	1.54	0.50	--
	2	93.61	4.35	1.45	0.59	0.55
Al-Cu-Fe-Mn Phase	3	46.83	34.83	--	4.63	13.70
	4	45.12	36.17	--	4.17	14.54
Al-Cu-Mg Phase	5	44.43	41.46	14.11	--	--
	6	46.32	40.23	13.45	--	--

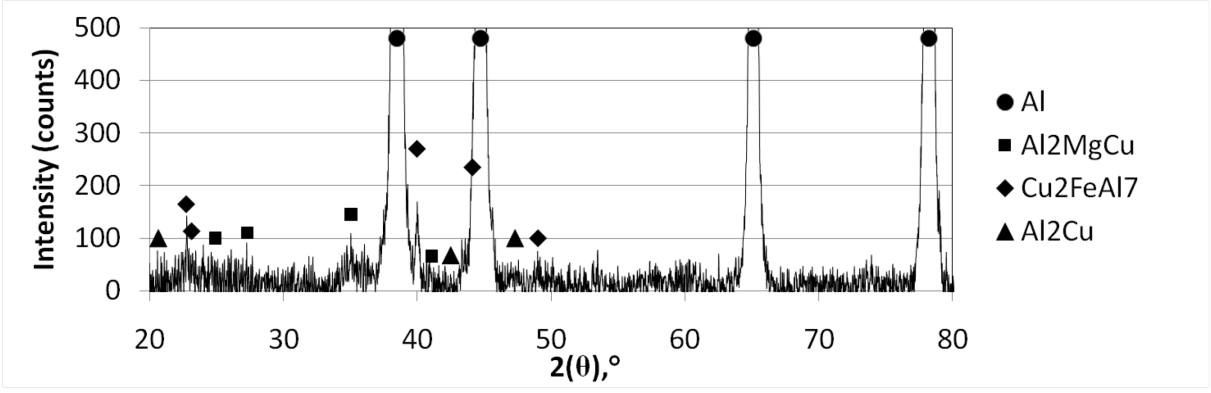

Figure 44 – XRD spectrum acquired from wrought AA2024 T6.

6.5 Conclusions

Through the work completed in this study the following conclusions have been reached:

1) Peak flow stress modelling of the P/M and wrought alloys studied yielded similar results with both adhering to a standard Zener-Hollomon curve fitting approach.

2) It was confirmed that full density could be achieved in P/M 2324 by hot deformation (100% of theoretical density). This process increased the mechanical properties of the alloy, with a ~ 25% increase in UTS and YS and 3-fold increase in elongation due to the reduction of porosity and breakup of the remnant oxide network that would have existed in the as-sintered alloy.

3) The highest values for yield strength and UTS were observed in hot swaged P/M 2324. It is postulated that this resulted from the elimination of porosity and the strengthening effect imparted from the oxide phase(s) that would have remained in the alloy after sintering.

4) Certain microstructural differences existed between P/M 2324 and AA2024. The major secondary phase in the P/M alloy was the θ phase (Al_2Cu) yet a combination of the S-phase (Al_2MgCu) and θ existed in the wrought system. The wrought alloy also contained a measureable presence of $Al_7Cu_2(Fe,Mn)$; a phase that was not detected in P/M 2324.

Chapter 7.0 Effects of Silicon Carbide on the Hot Deformation of P/M 2324

The second phase of research completed involved the addition of five volume percent addition of SiC to P/M 2324. The sintering practices were studied to assess the effects of SiC on the densification of the alloy. The mechanical properties of the addition were also studied in the form of tensile testing. The hot deformation characteristics of the alloy were studied in the form of Gleeble thermo-mechanical test and subsequent Zenner-Hollomon modeling of the peak flow stress. The microstructure was also characterized in both the as sintered and hot deformed states via optical microscopy, SEM, EDS, and XRD.

7.1 Processing of P/M 2324 with admixed SiC

In this work, 800 grit Silicon Carbide powder from Electro Abrasives was added to the powder blend of P/M 2324 in the amount of five volume percent. An SEM image of the powders is shown Figure 45 demonstrating the angular nature of the powders. To assess the effectiveness of the sintering procedure on P/M 2324 with an addition of 5v/o SiC, the sinter density, dimensional change and microstructure of the as-sintered materials were considered. As in the previous section, cylinders of the powder blend were uni-axially pressed at 400 MPa and subsequently sintered in an industrial continuous mesh belt furnace at 610°C for 20 minutes under an atmosphere of flowing nitrogen. The resulting cylinders achieved an average sinter density of 2.73 g/cc (97.9% of the full theoretical), and experienced dimensional changes as shown in Table XXIII. The alloy did not achieve the same high sinter density that was achieved in P/M 2324 without the SiC addition (%). This indicated that SiC had a moderately negative effect on densification, although a good sinter density for a P/M MMC was still achieved.

Table XXIII – Average dimensional change in sintered cylinders of P/M 2324+5%SiC.

OAL %	Diameter %
-1.89 +/- 0.35	-1.86 +/- 0.14

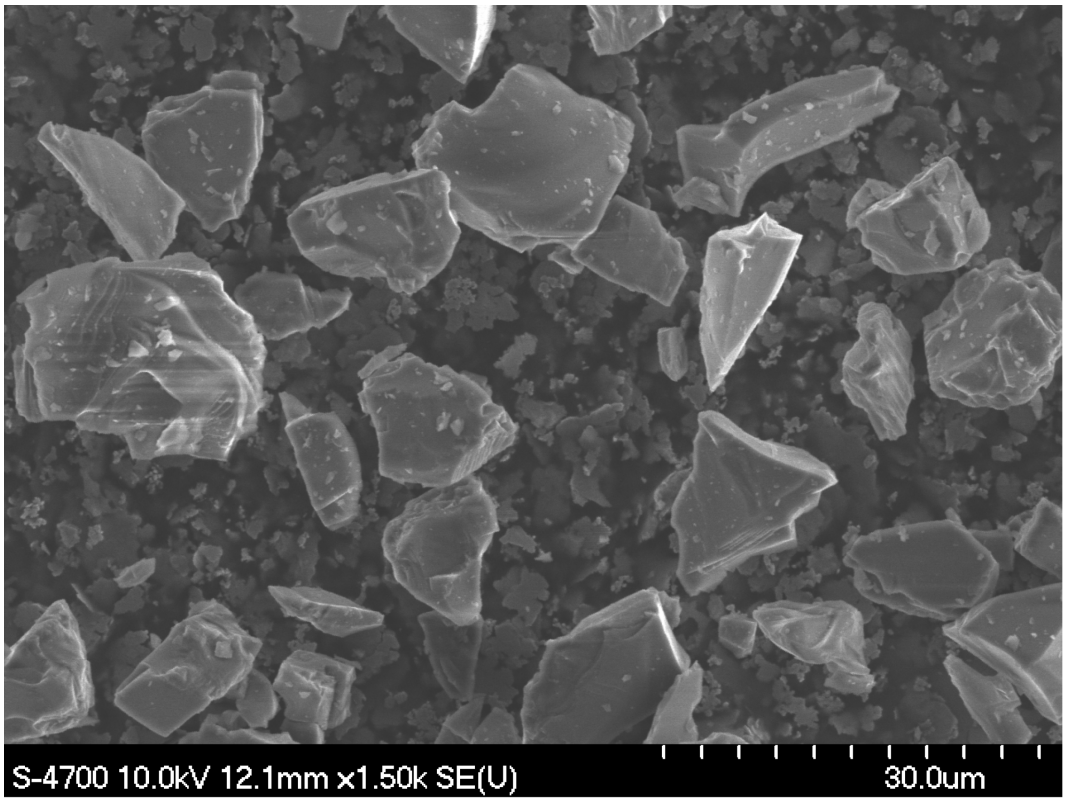

Figure 45 – SEM micrograph of 800 grit SiC from Electro Abrasives.

7.2 Hot Deformation of P/M 2324 + 5v/o SiC

Hot compression tests were performed on P/M 2324+5v/o SiC for numerous combinations of temperature and strain rate. Examples of the resultant plots are shown in Figure 46 for the MMC upset forged at a temperature of 450°C. These data showed that during compression, the material exhibited a maximum true compressive stress at a low strain followed by dynamic flow softening, as was found in P/M 2324 and wrought AA2024.

The peak flow stresses measured for all temperature/strain rate combinations are summarized in Table XXIV. The peak flow stress values for P/M 2324+5v/o SiC followed the same trends as found in P/M 2324 but were all slightly lower. This indicated that less force was required to deform the alloy with the SiC addition. This may have been caused by the lower sinter density of

the alloy. In this sense, the increased porosity would give the alloy a weaker structure and in turn mandate a lower peak flow stress.

As previously noted, the elimination of residual porosity in P/M 2324 and P/M 2324+5v/o SiC was a key goal of this forging study. As such, the densities of forged P/M cylinders were measured. In all cases, it was found that a density of 2.77 g/cc was achieved, corresponding to 99.0% the full theoretical density of the alloy. This was a promising result as it showed that densification of the alloy was achieved upon hot compression at all of the strain rates and temperatures considered. However, greater density was achieved in the material without the SiC addition. This leads one to believe that SiC had a negative effect on densification.

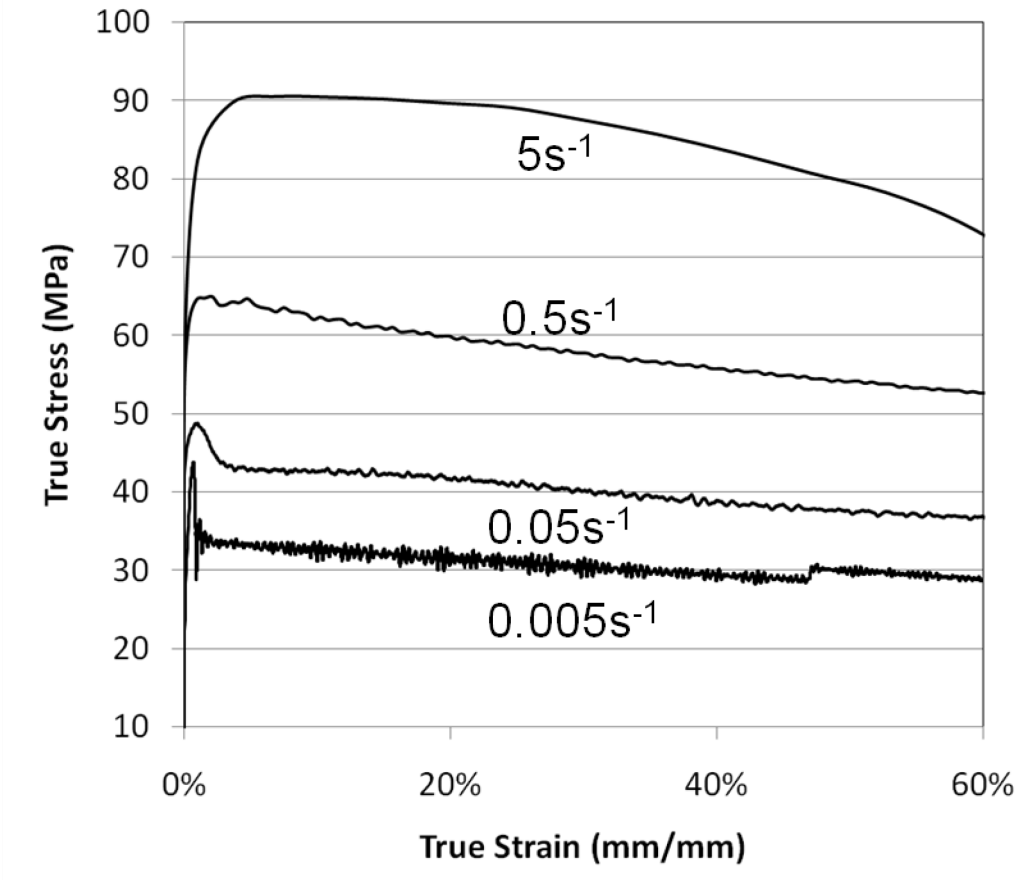

Figure 46 - True compressive stress/strain curves completed at 450°C for P/M 2324 + 5v/o SiC.

Table XXIV – Gleeble peak flow stress (MPa) data for P/M 2324+5v/o SiC as related to deformation temperature and strain rate.

	True strain rate (s^{-1})			
Temperature (°C)	0.005	0.05	0.5	5
350	99.9	120.7	147.3	170.3
400	65.2	73.5	103.1	121.6
425	50.1	66.7	82.9	104.8
450	46.2	48.8	64.9	90.5
475	33.0	36.4	53.6	70.1

7.3 Flow Stress Analysis (Zenner-Hollomon)

As in the previous chapter, experimental data were used to model the peak flow stress of 2324+5v/o SiC as a function of strain rate and temperature. Initially, values of α were solved using a computer program. The average slope of the trend lines for log(έ) vs. log(sinh(ασ)) were then taken as the material constant *n* while the average slope of the trend lines in log(sinh(ασ)) vs. T^{-1} was taken as the numeric value of *s*. Next, the activation energy of deformation, *Q*, was solved using Equation 5. With values for *Q*, α, s, and *n* identified for each alloy, an average value for ln(A)was determined using Equation 4. Finalized values for the wrought and P/M alloys studied are compared in Table XXV.

For P/M 2324 + 5v/o SiC, the value for α was lower than that of the other alloys although N was higher and ln(A) was in between. Given the variations in the values, the peak flow stress trends may be quite similar as the values tend to cancel each other out.

Table XXV – Comparison of the Zener-Hollomon parameters calculated for wrought AA2024, P/M 2324, and P/M 2324 + 5v/o SiC.

	AA2024	P/M 2324	P/M 2324 + 5v/o SiC
α	0.0125	0.0165	0.0115
N	6.75	7.28	7.61
S	5412	6030	5021
Q	304	365	318
ln(A)	49.7	57.0	53.3

Having identified suitable values for all constants, these data were then inserted into Equation 4 enabling a direct comparison between calculated and experimental findings as shown in Figure 47, with the points being experimental values and the lines calculated trends. It was noted that the values fit the modeled plots well validating the approach. A similar quality of fit was achieved in the alloy without the SiC addition. This implies that SiC did not have an appreciable effect on the validity of this modeling method or the deviation in the flow stress behaviour.

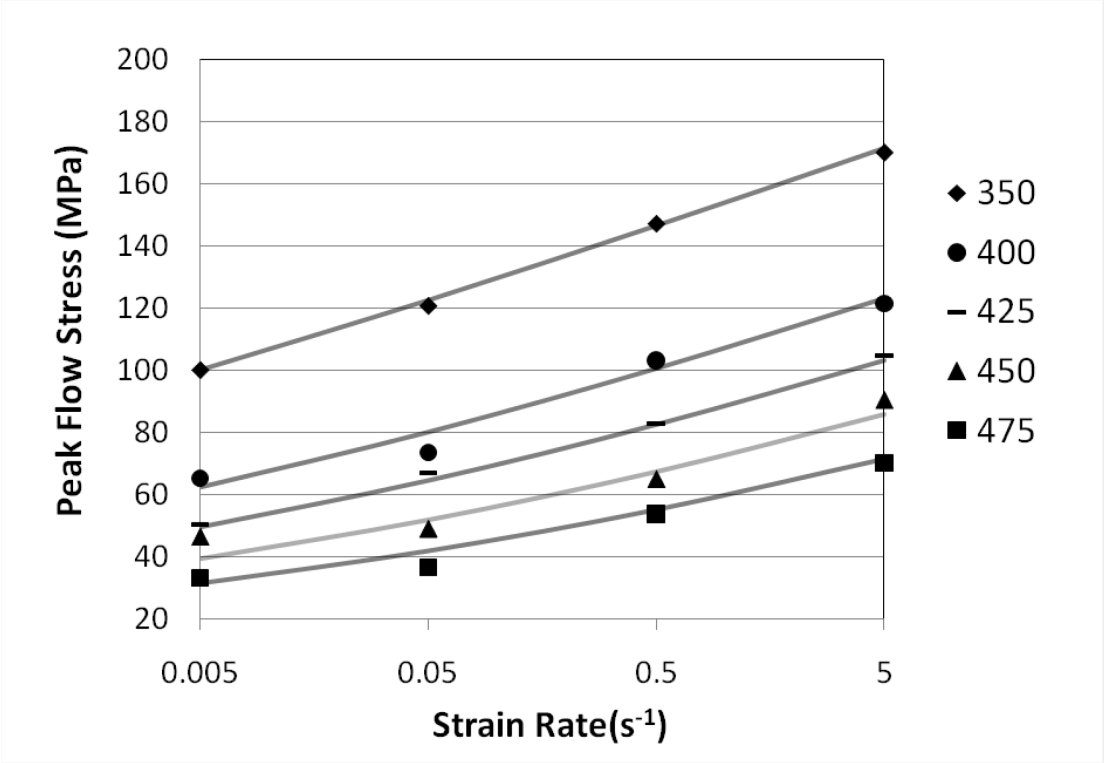

Figure 47 – Comparison of experimental and calculated peak flow stress data for P/M 2324+5v/o SiC.

7.4 Effects of Hot Deformation

As in section 6.4.4, rotary Swaging of P/M 2324+5v/o SiC was then performed to simulate hot forging procedures on bars large enough to extract tensile specimens. As with P/M 2324, swaging was completed at 495°C, the solutionizing temperature of the material. Based on thermal mechanical test data, temperature and strain rate had no measurable effect on densification. Conversely, these parameters had an acute affect on values with higher temperatures and lower strain rates favouring a reduced peak flow stress. In this sense, it was desirable to swage bars at the highest temperature possible. This temperature was chosen as less force is required to deform the material at higher temperature, and the solutionizing temperature is generally as hot as the alloy can get without forming a liquid. The possibility of cracking is greatly increased when a liquid phase is present in the alloy and should be avoided. The final swaged density resulted in a fully dense material matching prior measurements on the test cylinders upset forged in the gleeble.

Tensile test results of P/M 2324 with and without SiC addition are shown in the T6 temper in Figure 48. A ~25% increase in UTS and YS was observed as was a 3-fold increase in elongation between the sintered and swaged conditions of both alloys. These improved mechanical properties can be explained by the removal of porosity and the breakup of the oxide layer that was present on the aluminum powders from which the material was produced. [42] The YS and UTS of swaged P/M 2324 +5 v/o SiC were higher than that of P/M 2324 although the elongation was inferior. The SiC addition increased the strength but had a negative effect on the ductility of the alloy.

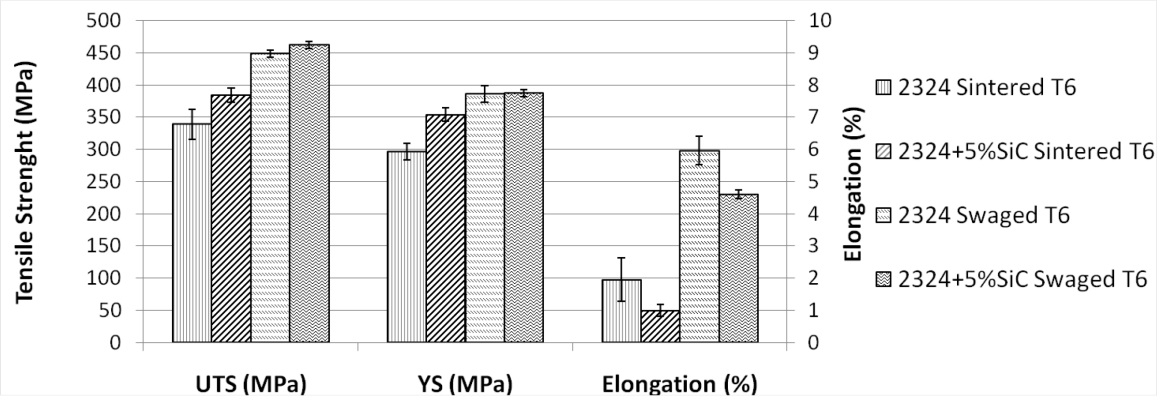

Figure 48 – Tensile data of P/M 2324 and P/M 2324 + 5 v/o siC in the sintered and swaged conditions. All materials heat treated to the T6 temper.

Optical micrographs of P/M 2324 + 5v/o SiC T6 in both the as sintered and swaged conditions are shown in Figure 49. The presence of SiC particles and porosity can be seen in both images. These SiC particles appeared to be present in clusters at the aluminum grain boundaries. A greater amount of porosity was seen in the as sintered condition, which is consistent with the density of the materials. The porosity in the sintered structure appeared to be mainly present around clusters of SiC. This suggests that the SiC particles may have been grouped together, limiting the densification of the alloy during sintering. This can explain why a higher percent of the theoretical density was achieved in the alloy without the SiC addition.

No breaking of the SiC particles was found in the swaged material. This was viewed as a positive result given that the fracture of a secondary phase can cause an increase in porosity as in the work by Mosher et. al. where silicon particles shattered in a swaged aluminum silicon P/M alloy [31].

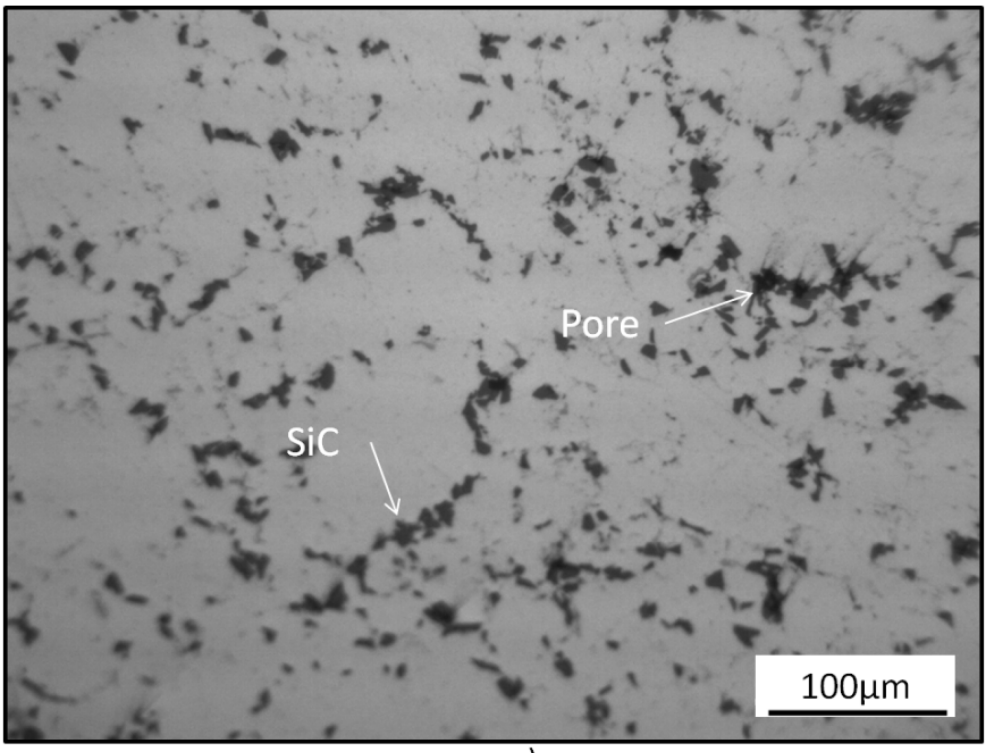

a)

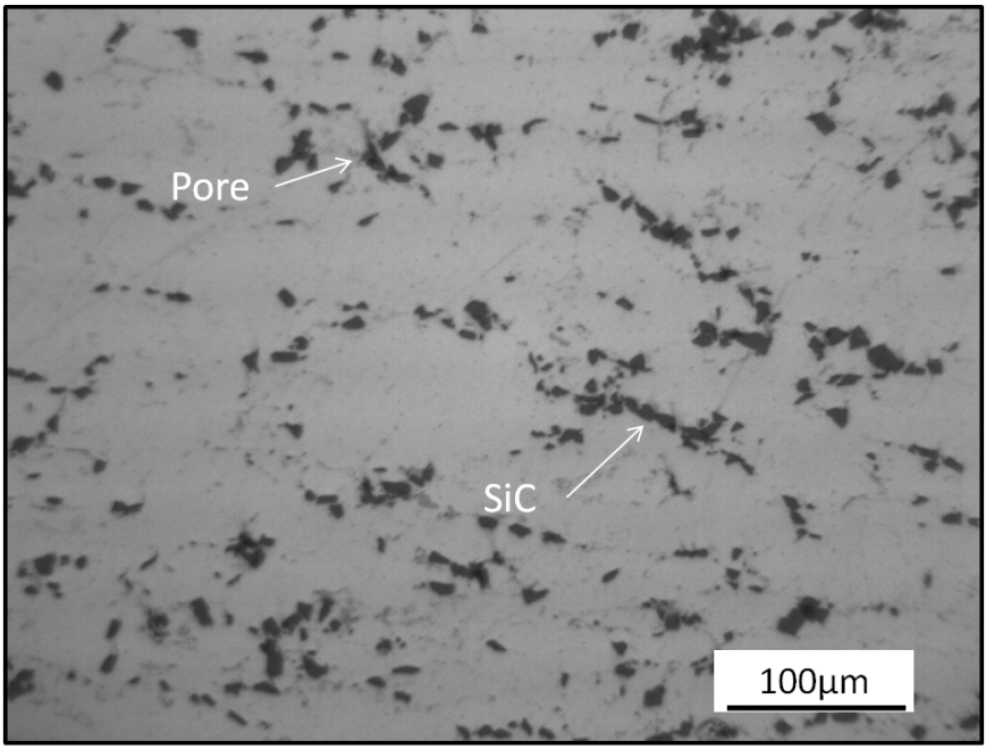

b)

Figure 49 – Optical Micrographs of P/M 2324+5v/o SiC T6 in the (a) as sintered and (b) hot swaged condition.

Fracture surfaces of P/M 2324+5v/o SiC T6 in both the as sintered and swaged conditions are shown in low magnification in Figure 50 and in high magnification in Figure 51. The low magnification images show the general fracture surface with a greater degree of microvoid coalescence evident in the hot swaged material, consistent the observation of an increased ductility (Figure 51). The presence of SiC is shown in the images as well. SiC was more evident in the sintered material. This may be caused by SiC acting as more of a crack propagation site on the sintered material over the hot swaged. This could be caused by a greater degree of bonding in the swaged material.

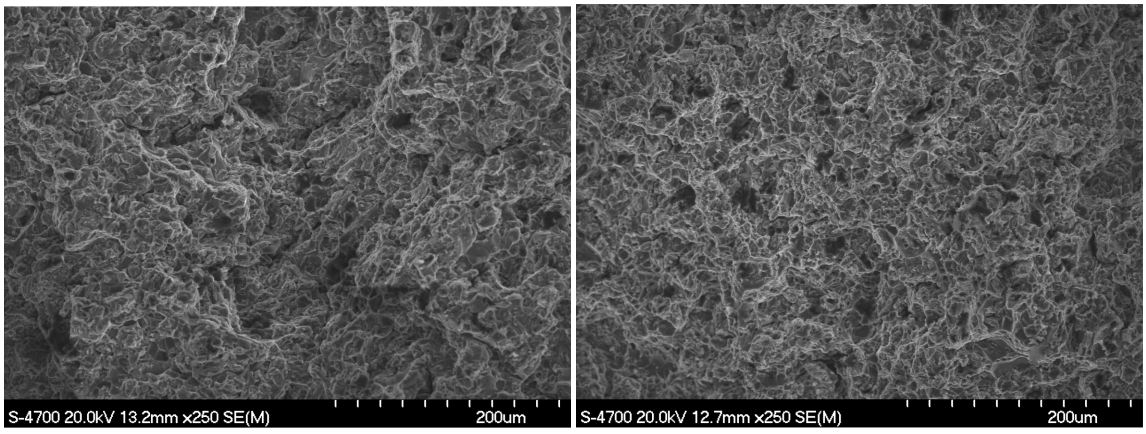

(a) **(b)**

Figure 50 – Fracture surface of (a) P/M 2324+5%SiC T6 in the as sintered condition and (b) the swaged condition at 250x magnification.

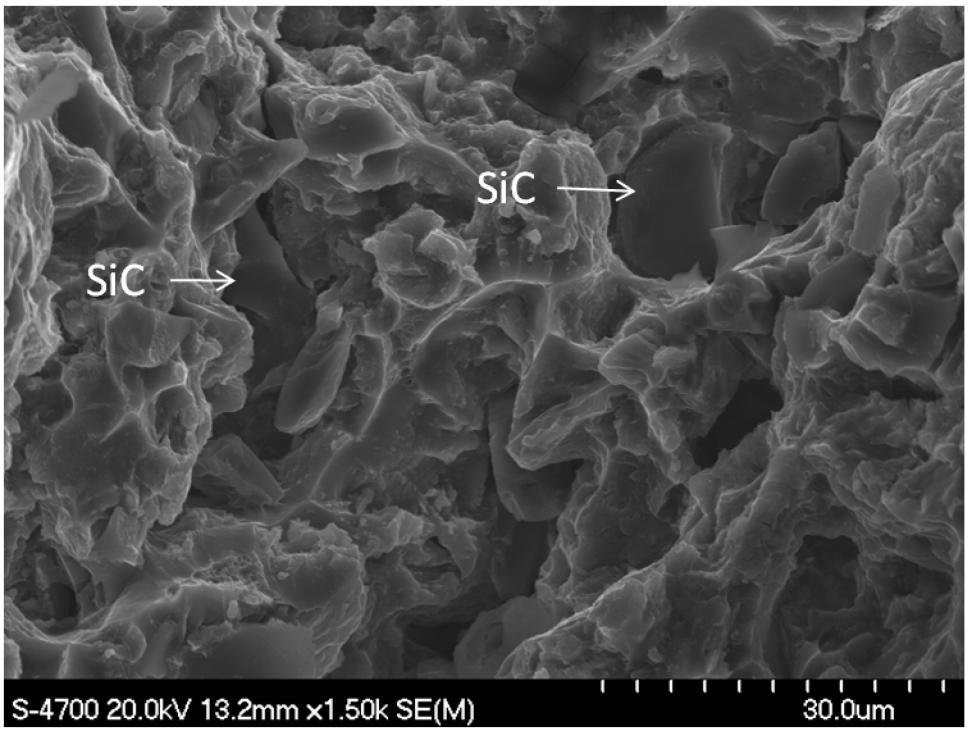

(a)

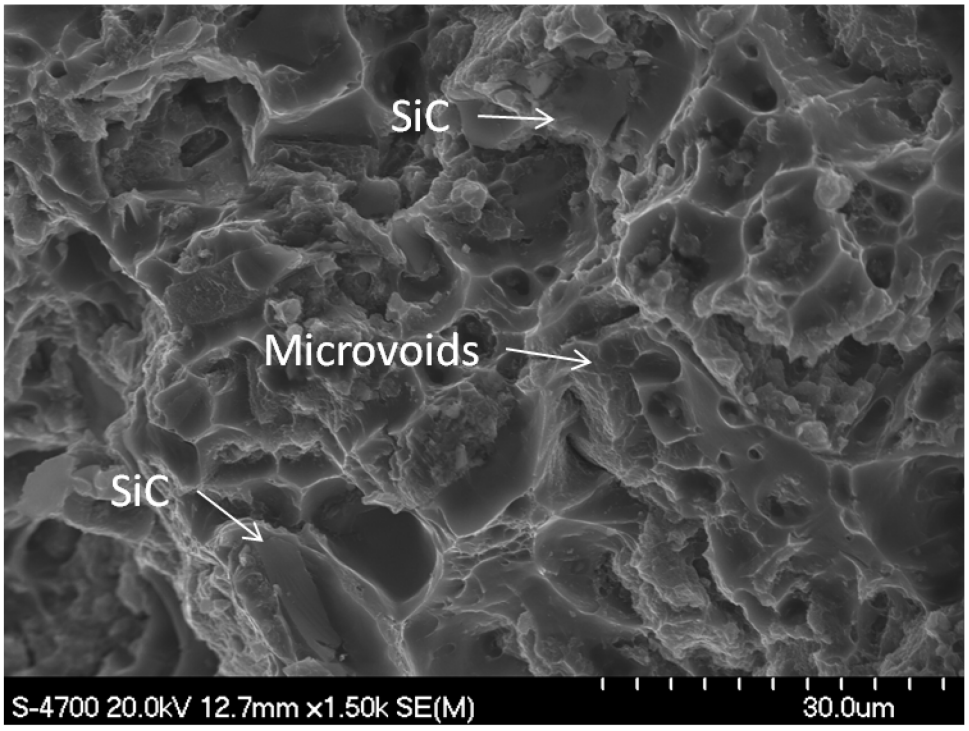

(b)

Figure 51 – Fracture surface of P/M 2324+5v/o SiC T6 (a) as sintered and (b) hot swaged at 1.50kx magnification

7.5 Microstructure Characterization

In the final phase of research, detailed microstructural analyses were completed on the MMC materials. An SEM micrograph of P/M 2324+5v/o SiC T6 in the as sintered condition is shown in Figure 52. The chemical compositions of the marked points on the image as measured by EDS techniques are presented in Table XXVI. There was found to be an aluminum rich matrix and a secondary phase(s) present at the aluminum grain boundaries. From EDS, the latter was found to contain high concentrations of aluminum and copper and iron with smaller amounts of magnesium. From XRD (Figure 53) it was confirmed that θ ($CuAl_2$) was present in the alloy and that tin had reacted with magnesium to form Mg_2Sn. Silicon carbide was also apparent in the structure and confirmed through EDS and XRD.

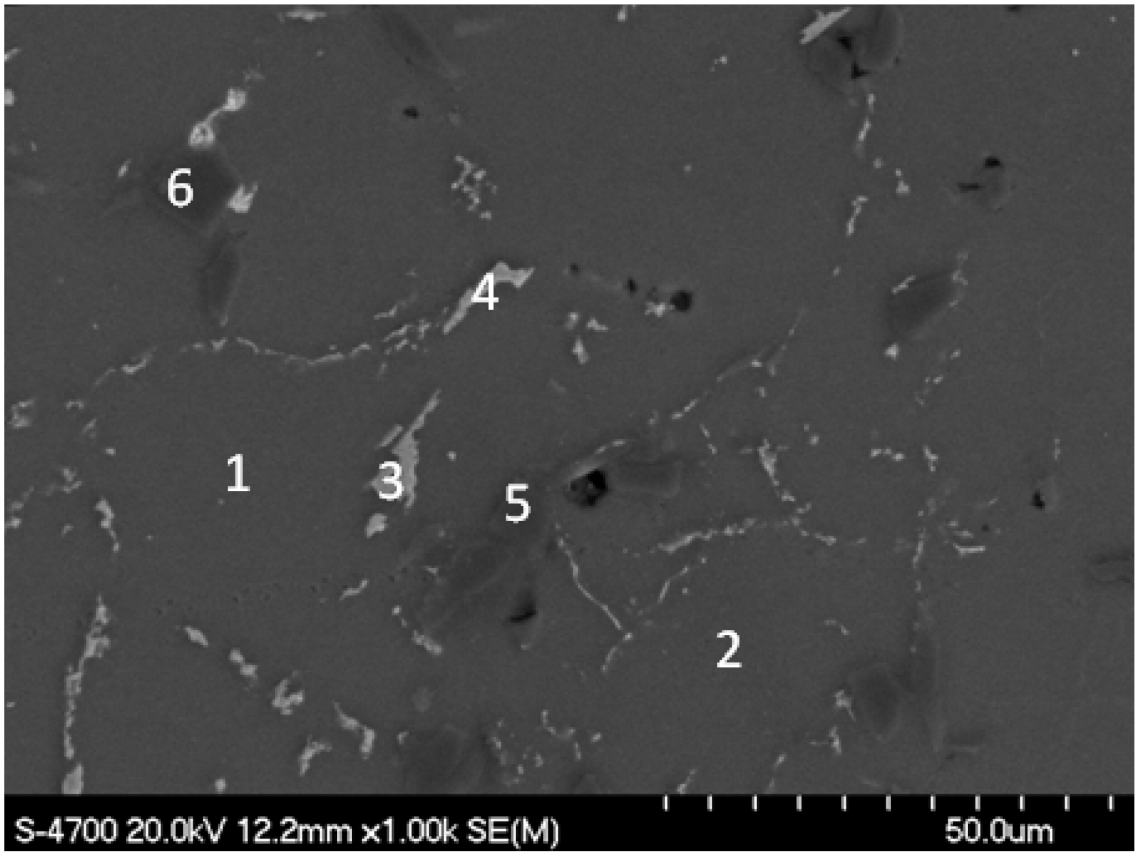

Figure 52 – SEM image of P/M 2324+5v/o SiC T6 in the as sintered condition.

Table XXVI - EDS measurements recorded at the point locations shown in Figure 52 (w/o).

Phase	Location	Al	Cu	Mg	Fe	Sn	Si	C
Aluminum Matrix	1	93.76	5.25	1.00				
	2	93.86	4.94	1.20				
Al-Cu-Fe-Mg Phase	3	57.70	27.93	1.67	12.71			
	4	55.81	28.17	2.46	13.34			
Silicon Carbide	5	3.21	0.05				60.26	36.49
	6	1.79	0.09			0.35	67.77	30.00

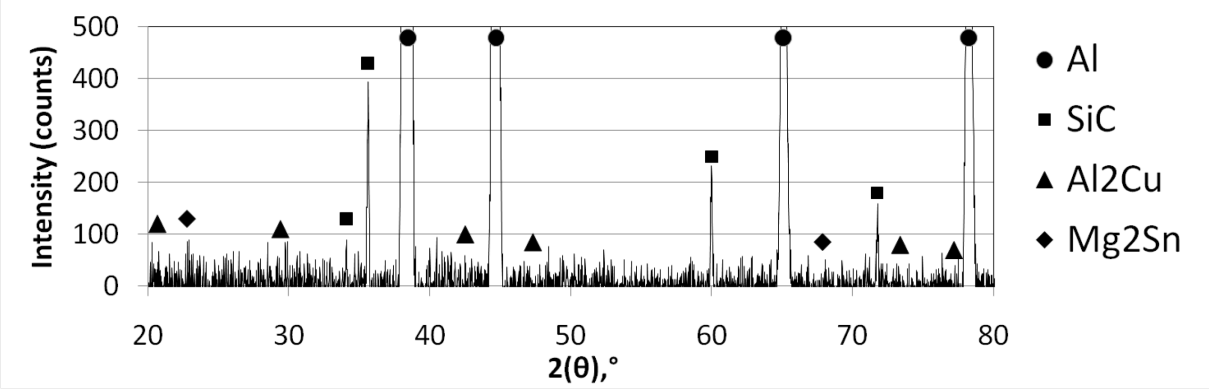

Figure 53 – XRD spectrum acquired from 2324+5v/o SiC T6 in the as sintered condition.

An SEM micrograph of hot swaged P/M 2324+5v/o SiC T6 is shown in Figure 54 with the corresponding EDS point compositions given in Table XXVII. The effects of swaging on the microstructure of the alloy that can be seen in the micrograph include texture in the grain orientation and the reduction of porosity. The remaining porosity was found mainly around clusters of SiC. The dominant phases present in the swaged alloy were the same as those observed in the sintered alloy, Al_2Cu and Mg_2Sn, based on XRD data (Figure 55). The occasional presence of impurities was also noted with varying amounts of iron, nickel and silicon observed in select features.

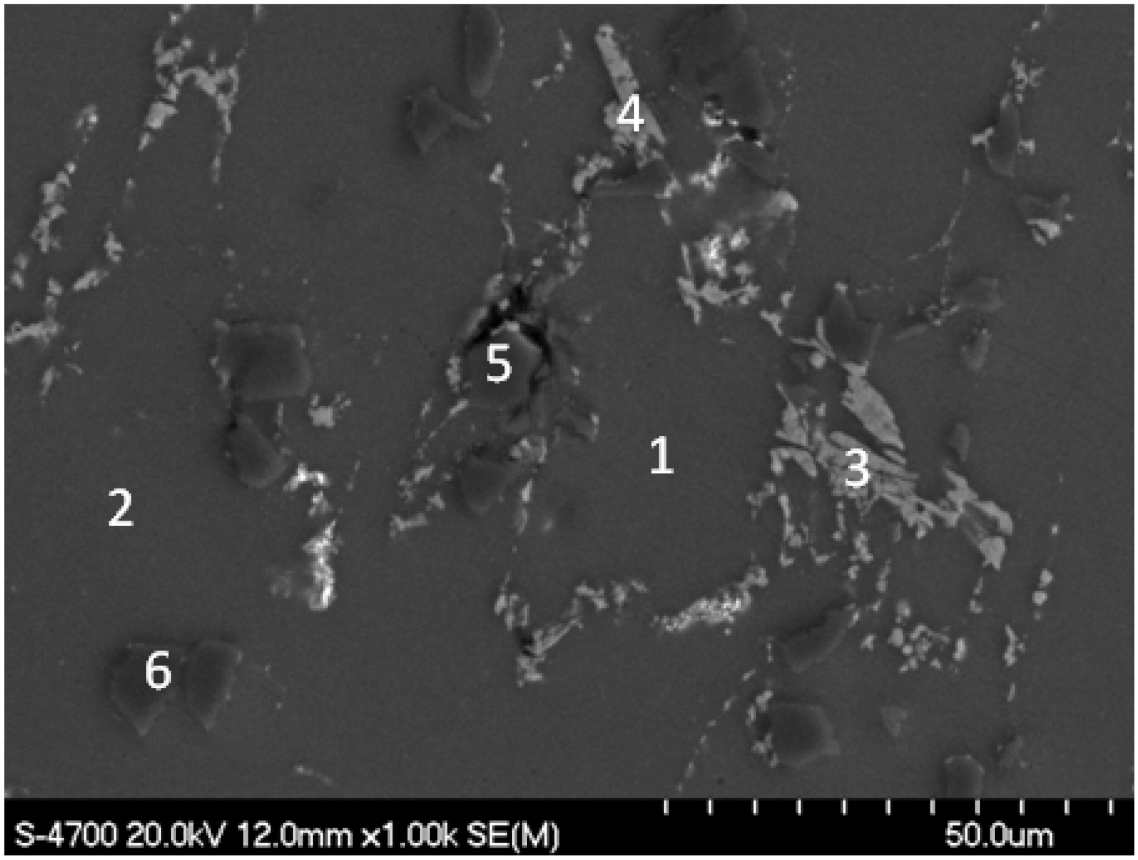

Figure 54 – SEM image of P/M 2324+5v/o SiC T6 in the swaged condition.

Table XXVII – EDS measurements recorded at the point locations shown in Figure 54 (w/o)

Phase	Location	Al	Cu	Mg	Fe	Si	C
Aluminum Matrix	1	94.26	4.55	1.18			
	2	94.16	4.66	1.17			
Al-Cu-Mg-Fe Phase	3	49.06	33.57	1.29	16.08		
	4	48.93	32.52	5.08	8.53	4.93	
Silicon Carbide	5	1.42				69.11	29.47
	6	0.96				69.08	29.96

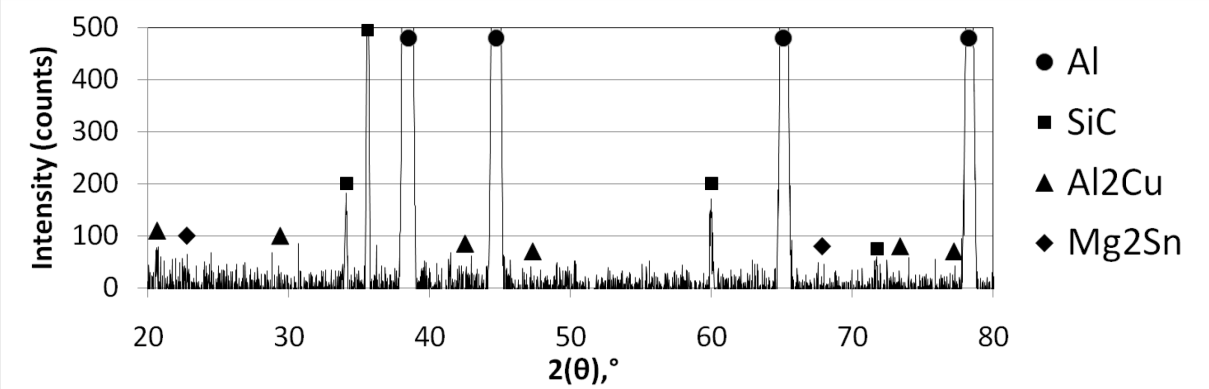

Figure 55 – XRD spectrum acquired from 2324+5v/o SiC T6 in the swaged condition

The microstructure of P/M 2324 was quite similar to that of P/M 2324+5v/o SiC except for the presence of SiC. The same precipitate phases appeared to be present in both the as sintered and hot swaged conditions. This implied that the increase in yield strength and UTS between P/M 2324 T6 and P/M 2324+5v/o SiC T6 and the reduced elongation can be directly linked to the strengthening effect of the SiC addition. The same level increased properties was not found in the between the alloys in the hot swaged condition as the same amount of densification was not achieved due to the clustering of SiC particles.

Chapter 8.0 Future Work

Following the research performed in this study, there are some areas where future work may be beneficial:

1) Further study on the optimization of the SiC addition should be completed, using different volume percents and particle sizes.
2) Study on the properties of wear and fatigue on the alloy with and without SiC to further quantify the effectiveness of this addition.
3) Properties of industrially forged parts should be studied.

Chapter 9.0 Conclusions

Through the work completed in this study the following conclusions have been reached:

1) P/M 2324 achieved a sintered density of 2.75 g/cc (99.5% of the full theoretical), while P/M 2324 + 5 v/o SiC achieved a sinter density of 2.73 g/cc (97.9% of the full theoretical). This suggests that the addition of 5 v/o SiC had a mildly negative effect on the densification during sintering.

2) Peak flow stress modelling of the P/M and wrought alloys studied yielded similar results with both adhering to a standard Zener-Hollomon curve fitting approach. The peak flow stress values for P/M 2324 + 5 v/o SiC followed the same trends as found in P/M 2324 but were all slightly lower. This may have been caused by the lower sinter density of the starting sintered preform.

3) It was confirmed that full density could be achieved in P/M 2324 by hot deformation (100% of theoretical density). This process increased the mechanical properties of the alloy, with a ~ 25% gain in UTS and YS and 3-fold rise in elongation due to the reduction of porosity and breakup of the remnant oxide network that would have existed in the as-sintered alloy.

4) It was confirmed that P/M 2324 + 5v/o SiC achieved a density of 2.77 g/cc by hot deformation (99.0% the full theoretical density). This process increased the mechanical properties of the alloy, with a UTS of 448 MPa, a YS of 386 MPa, and an elongation of 5.6% due to the reduction of porosity and breakup of the remnant oxide network that would have existed in the as-sintered alloy.

5) The highest values for yield strength and UTS were observed in hot swaged P/M 2324. It is postulated that this resulted from the elimination of porosity and the strengthening

effect imparted from the oxide phase(s) that would have remained in the alloy after sintering.

6) Certain microstructural differences existed between P/M 2324 and AA2024. The major secondary phase in the P/M alloy was the θ phase (Al_2Cu) yet a combination of the S-phase (Al_2MgCu) and θ existed in the wrought system. The wrought alloy also contained a measureable presence of $Al_7Cu_2(Fe,Mn)$; a phase that was not detected in P/M 2324.

7) Hot Deformation of P/M 2324 is an effective method to increase mechanical properties.

References

[1] Boland, C. D., Hexemer Jr. R. L., Donaldson, I. W., Bishop, D. P. (2010). *On the development of an aluminum P/M alloy for "press-sinter-size" technology.* Proceedings of the 2010 International Conference on Powder Metallurgy and Particulate Materials, 7, 64-77.

[2] Bishop, D. P. (2008) *Aluminum alloy bulk chemistry formulation*. U.S.A.: Patent 61104572.

[3] Rajesh, P., Rakesh, S. (2002) *Modeling and Simulation of Press Forming of Aluminum-5 Weight % SiCp Composites.* Powder Metallurgy in Automotive Applications-II. Ed. Ramakrishnan Mohan. USA: Science Publishers, Inc., 159-176.

[4] Narayanasamy, R., Senthilkumar, V., Pandey, K. S. (2006) *Some aspects on hot forging features of P/M sintered iron performs under various stress state conditions.* Mechanics of Materials 38, 367–386

[5] Pease, L. F., West, W. G. (2002). *Fundamentals of powder metallurgy*. Princeton, N.J.: Metal Powder Industries Federation.

[6] German, M. R. (2005). *Powder metallurgy & particulate materials processing*. New Jersey: Metal Powder Industries Federation.

[7] German, R. M., (1994) *Powder Metallurgy science*, Metal Powder Industries Federation, Princeton, N.J. Second edition.

[8] Ecka-Granules, Powder-Metallurgy-Technologies (2009) Retrieved Feb/1 2009, from http://www.ecka-granules.com/index.php?id=153&typ=15&anwendung=3&L=2

[9] Khoei, A. R. (2005) *Computational Plasticity in Powder Forming Processes*, Elsevier.

[10] Turkish Powder Metallurgy Association (2002), "Powder manufacturing techniques", www.turktoz.gazi.edu.tr/en_tozmetal.htm, August 15 2003.

[11] Bishop, D.P., Hofmann, B., Couchman, K.R., (2000) *Properties and Attributes of Commercially Available AC2014-Type Aluminum P/M Alloys,* Advances in Powder Metallurgy and Particulate Materials, MPIF, 1 (12) 87-100.

[13] German, R. M., Suri, P., Park, S. J. (2008) *Review: liquid phase sintering*, Springer Science Business Media, LLC

[13] Schaffer, G. B., Sercombe, T. B., Lumley, R. N. (2001) *Liquid Phase Sintering of Aluminium Alloys*, Elsevier, Materials Chemistry and Physics 67, 85–91

[13] Smith, W. F. (1993) *Structure and properties of engineering alloys.* Materials Science and Engineering Series. Second Edition, 176-229.

[14] ASM (1998) ASM Handbook, Powder Metal Technologies and Applications, Volume 7.

[15] Bishop, D. P., Couchman, K. R., Geiman, T. E. (2002) *Effects of Thermal Exposure on the Mechanical Properties of Aluminum P/M Alloy AC2014*. Advances in Powder Metallurgy and Particulate Materials, MPIF, 7(1) 1-13.

[16] Mathers, G. (2002) *Material Standards, Designations and Alloys in The Welding of Aluminum and Its Alloys*, Woodhead Publishing Limited, Cambridge England, 35-49.

[17] Kalpakjian, S., Schmid, S. (2008) *Manufacturing Processes for Engineering Materials*. Fifth Edition. Prentice Hall.

[18] ASM (1996), *ASM Handbook, Forming and Forging,* Conventional Hot Extrusion, ASM Committee on Rotary Swaging, Volume 14.

[19] Rajesh, P., Rakesh, S. (2002) *Modeling and Simulation of Press Forming of Aluminum-5 Weight % SiCp Composites.* Powder Metallurgy in Automotive Applications-II. Ed. Ramakrishnan Mohan. USA: Science Publishers, Inc., 159-176.

[20] ASM (1996) *ASM Handbook, Forming and Forging*, Rotary Swaging of Bars and Tubes, ASM Committee on Rotary Swaging, Volume 14.

[21] LaDelpha, A. D. P., Mosher, M. P., Caley, W. F., Kipouros, G. J., Bishop, D. P. (2008) *On the simulation of wrought AA4032 via P/M processing*, Materials Science and Engineering A 479(1), 1–9.

[22] MacAskill,I. A., LaDepha, A. D. P., Milligan, J. H., Fulton, J. J., Bishop, D. P. (2009) *Effects of cold and hot densification on the mechanical properties of a 7XXX series powder metallurgy alloy,* Powder Metallurgy, 52(4).

[23] Chawla, N., Chawla, K. K. (2006) *Metal Matrix Composites*. Springer, 2006.

[25] ASM (2001) *ASM Handbook, Composites*, Volume 21.

[26] Kainer, K. (2006) *Metal Matrix Composites - Custom-made Materials for Automotive and Aerospace Engineering.* Ed. K. Kainer. Wiley-VCH.

[27] Broutman, L., Krock, H. (1974) *Composite Materials*. Ed. A. Metacalfe. Vols. Volume 1 - Interfaces in Metal Matrix Composites. San Diego: Academic Press.

[28] Mazen, A., Emara, M. (2004) Effect of Particle Cracking on the Strength and Ductility of Al-SiCp Powder Metallurgy Metal Matrix Composites. Journal of Materials Engineering and Performance, 13(1).

[29] Eksi, A., Veltl, G., Petzoldt, F., Lipp, K., Sonsino, C. M. (2004) *Tensile and fatigue properties of cold and warm compacted Alumix 431 alloy*, IoM Communications Ltd. Published by Maney for the Institute of Materials, Minerals and Mining.

[30] Mosher, M. P. (2009) Effects of Cr addition on the metallurgy and P/M processing response of alumix 431D, Dalhousie University.

[31] Mosher, W. G. E. Kipouros, G.J., Caley, W. F., Donaldson, I. W., Bishop, D. P. (2010) *On the deformation of Aluminum-Silicon powder metallurgy alloys.* Journal of Powder Metallurgy. DOI 10.1179/003258910X12678035166773.

[32] ASM (2004) *ASM Handbook, Properties and Selection: Non-Ferrous Alloys and Special Purpose Materials*, American Society for Metals, Metals Park, OH, Volume 2, 435-463.

[33] MPIF (2008) *Standard test methods for powders and powder metallurgy products*. Princton, New Jersy: Metal Powder Industries Federation.

[34] ASTM International (2005) *Standard practice for compression tests of metallic materials at elevated temperatures with conventional or rapid heating rates and strain rates*, E209–00, Philadelphia, PA, USA.

[35] McQueen, H. J., R. N. D. (2002) *Constitutive analysis in hot working.* Materials Science and Engineering: A(322) 43-52.

[36] Bardi, F., Cabibbo, M., Evangelista, E., Spigarelli, S., Vukcevic, M. (2002). *An analysis of hot deformation of an al-cu-mg alloy produced by powder metallurgy. Materials Science and Engineering: A, 339*(1), 43-52.

[37] Zhang, H., Li, L., Yuan, D., Peng, D. (2006). *Hot deformation behavior of new al-mg-si-cu aluminum alloy during compression at elevated temperatures*. Materials Characterization, 2007(58), 168-173.

[32] Dashwood, R. J., Schaffer, G. B. (2002). *Powder forging of a sintered al-3.8Cu-1Mg-0.8Si-0.1Sn alloy*. Materials Science and Engineering: A(323), 206-212

[39] Zhang, H., Lin, G.Y., Peng, D.S., Yang, L.B., Lin, Q.Q. (2003) *Dynamic and static softening behaviors of aluminum alloys during multistage hot deformation.* Materials Processing Technology 148 (2003) 245-249.

[40] Charpentier, P.L., Stone, B.C., Stone, S.C., Thomas Jr, J.F. (1986) *Characterization and modeling of the high temperature flow behaviour of aluminum alloy 2024.* Metallurgical transactions, physical metallurgy and materials science. A 17.12 (1986): 2227-2237.

[41] Dwivedi, S. N., Balakrishnan, R. (1990) *Development of constitutive equations and processing maps for Al 2024*. Computer modeling and simulation of manufacturing processes: presented at the winter annual meeting of the american society of mechanical engineers. Dallas, TX: American society of mechanical engineers, United Engineering center, 303-312.

[42] Laugée, C., Querbes, J.L., Grazzini, H., Lasne, P., Levaillant, C. (1988) *Forging of an aluminum P/M connecting rod: experimental results and computational preform design*. Proceeding of the 1988 international powder metallurgy conference. Orlando, Florida, 1988. 565-577.

[43] Kim, Y. W. (1985) *Surface oxides in P/M aluminum alloys.* Journal of Metals, 8(37) 27-33.

[44] Hatch, J. E. (1984) *Aluminum: properties and physical metallurgy*. American society for metals.

.

Appendix A: Peak Flow Curves

This section contains additional information on the hot deformation of P/M 2324, P/M2324+5%SiC and AA2024, including peak flow stress models produced for each alloy.

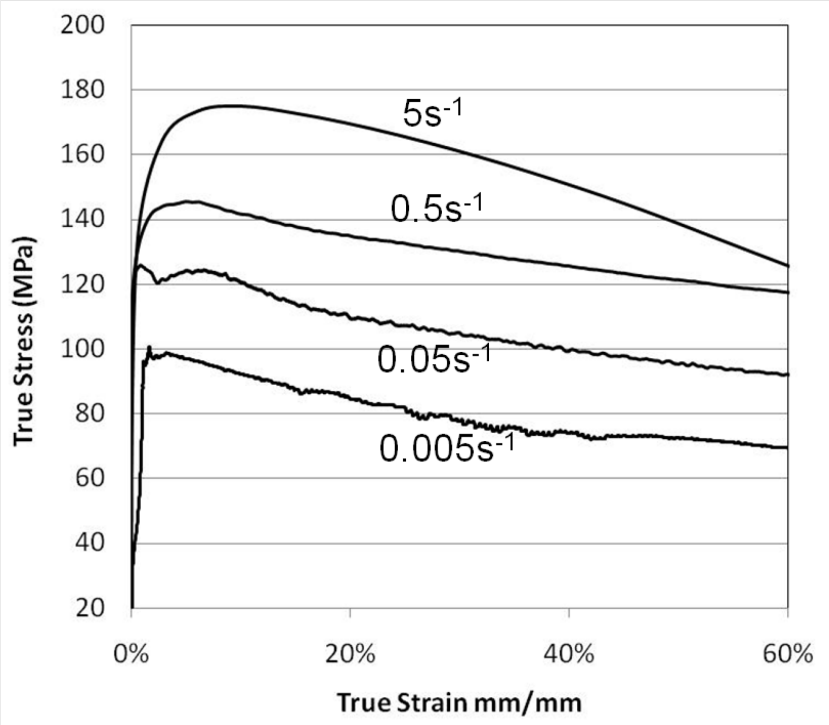

Figure A-1 – True compressive stress/strain curves completed at 350°C for P/M 2324.

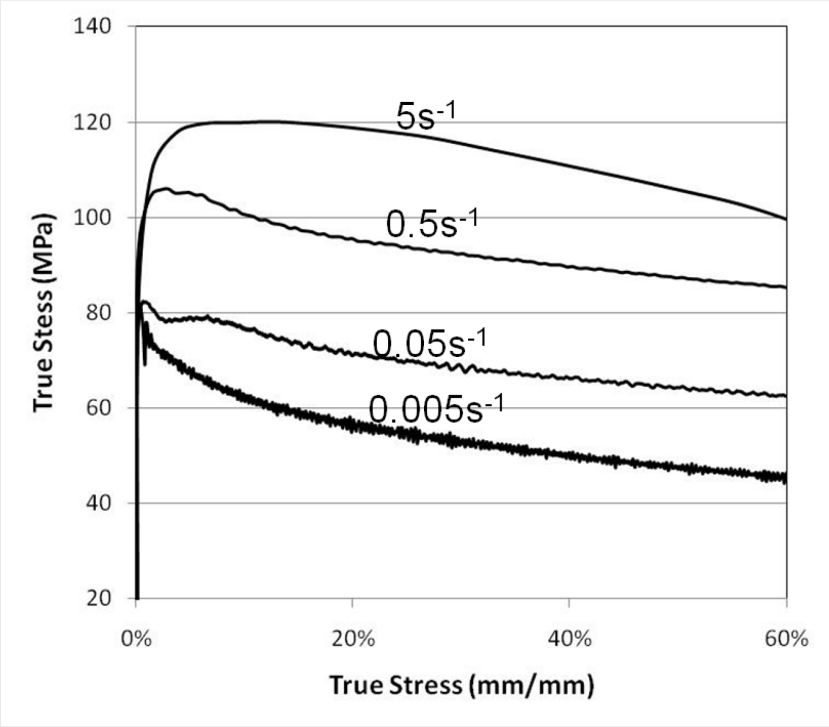

Figure A-2 – True compressive stress/strain curves completed at 400°C for P/M 2324.

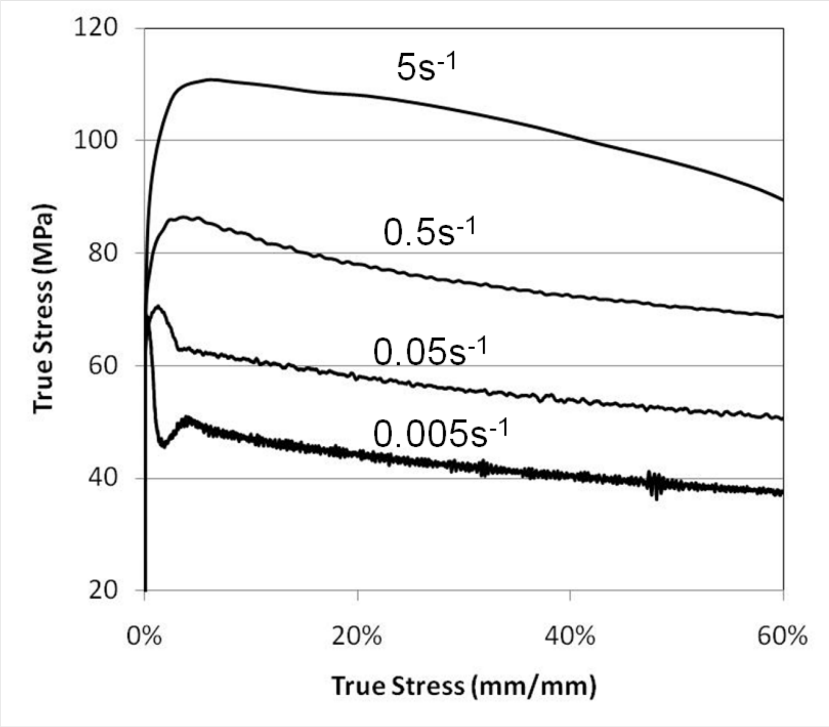

Figure A-3 – True compressive stress/strain curve of P/M 2324 completed at 425°C.

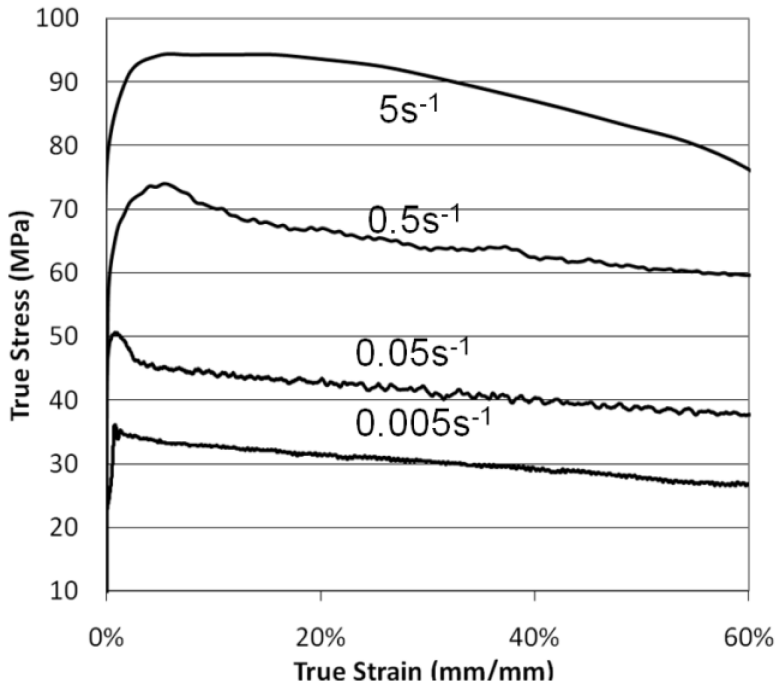

Figure A-4 – True compressive stress/strain curve of P/M 2324 completed at 450°C.

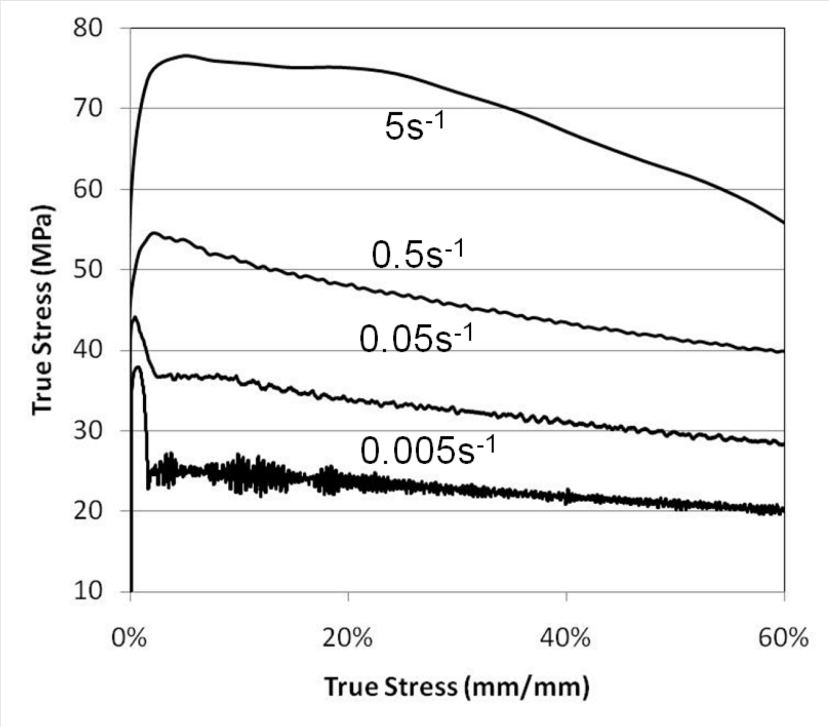

Figure A-5 – True compressive stress/strain curve of P/M 2324 completed at 475°C.

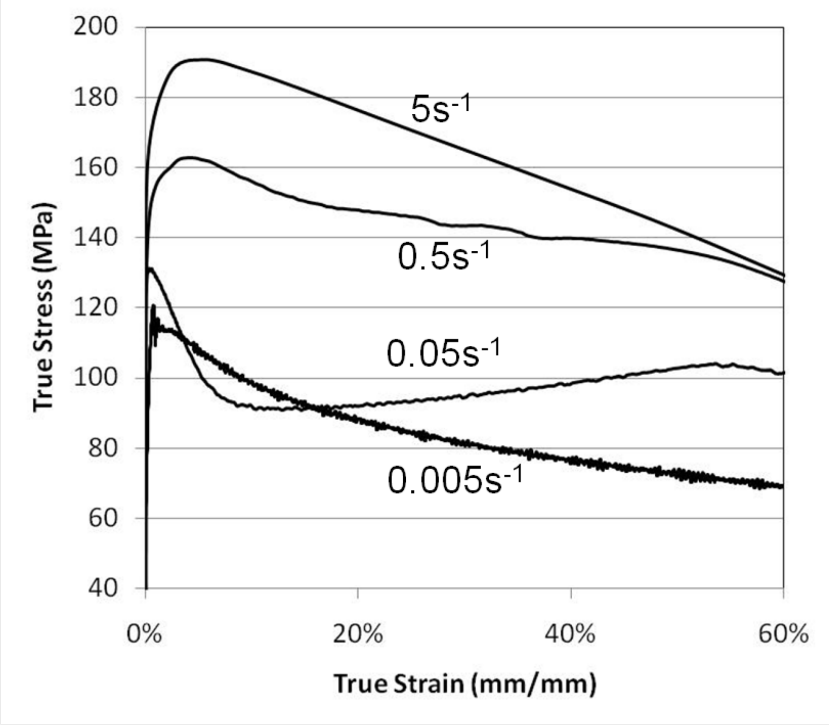

Figure A-6 – True compressive stress/strain curves of wrought AA2024 completed at 350°C.

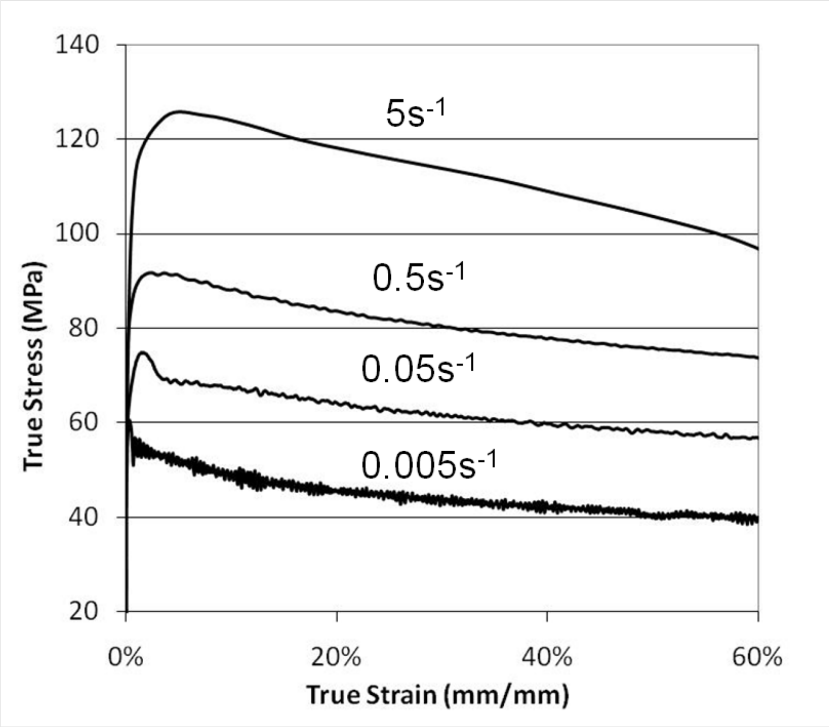

Figure A-7 – True compressive stress/strain curves of wrought AA2024 completed at 400°C.

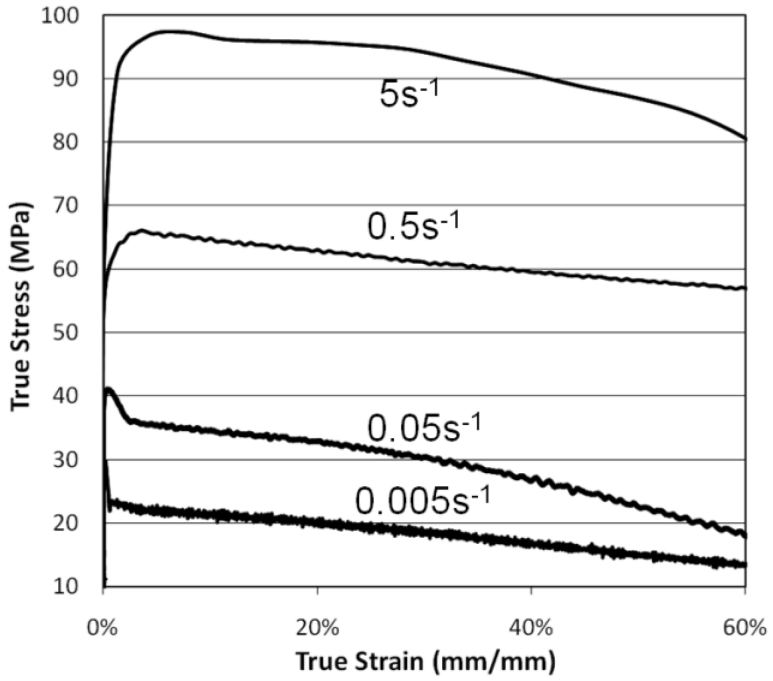

Figure A-8 – True compressive stress/strain curves of wrought AA2024 completed at 450°C.

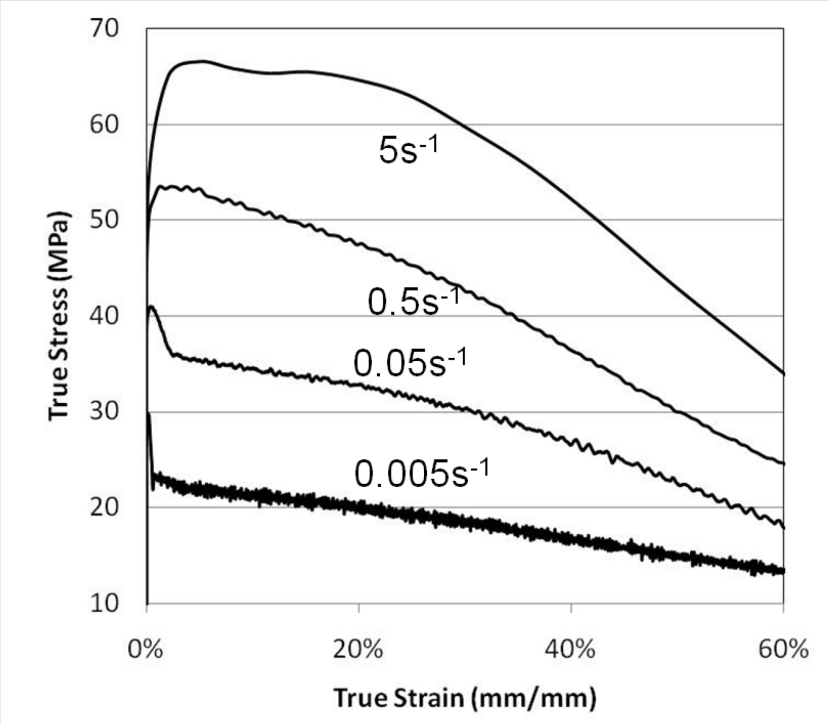

Figure A-9 – True compressive stress/strain curves of wrought AA2024 completed at 500°C.

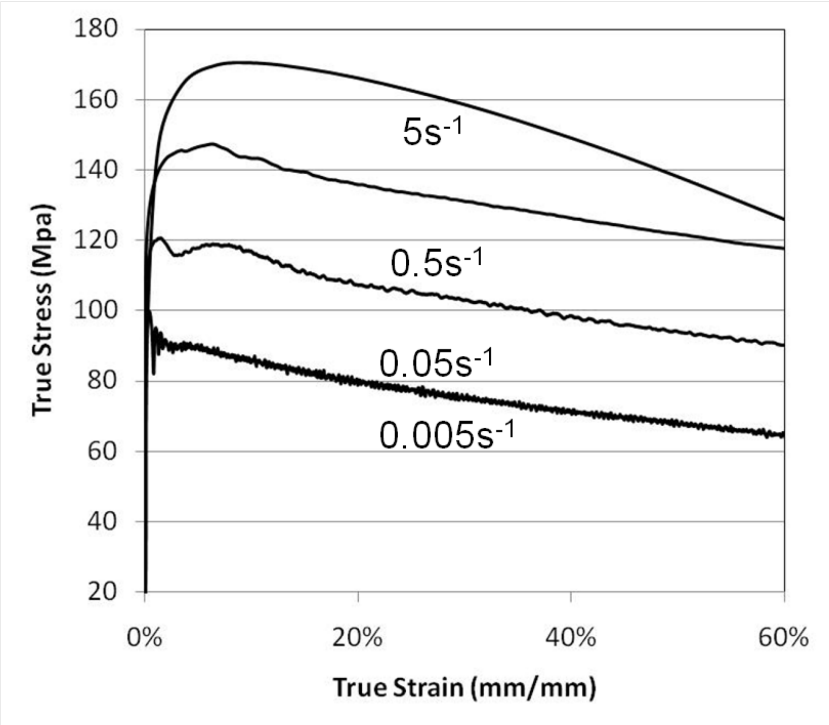

Figure A-10 – True compressive stress/strain curves completed at 350°C for P/M 2324 + 5v/o SiC.

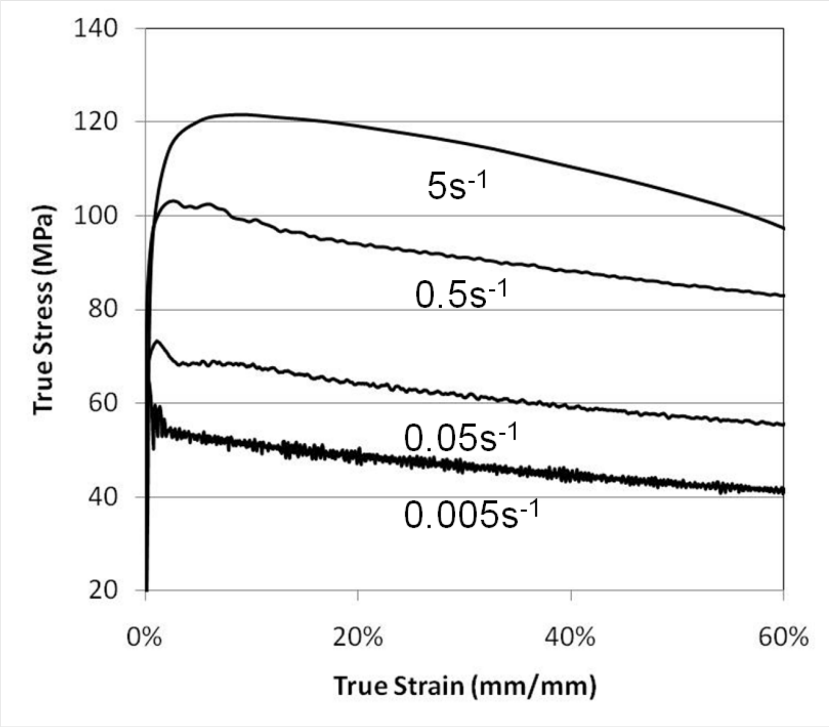

Figure A-11– True compressive stress/strain curves completed at 400°C for P/M 2324 + 5v/o SiC.

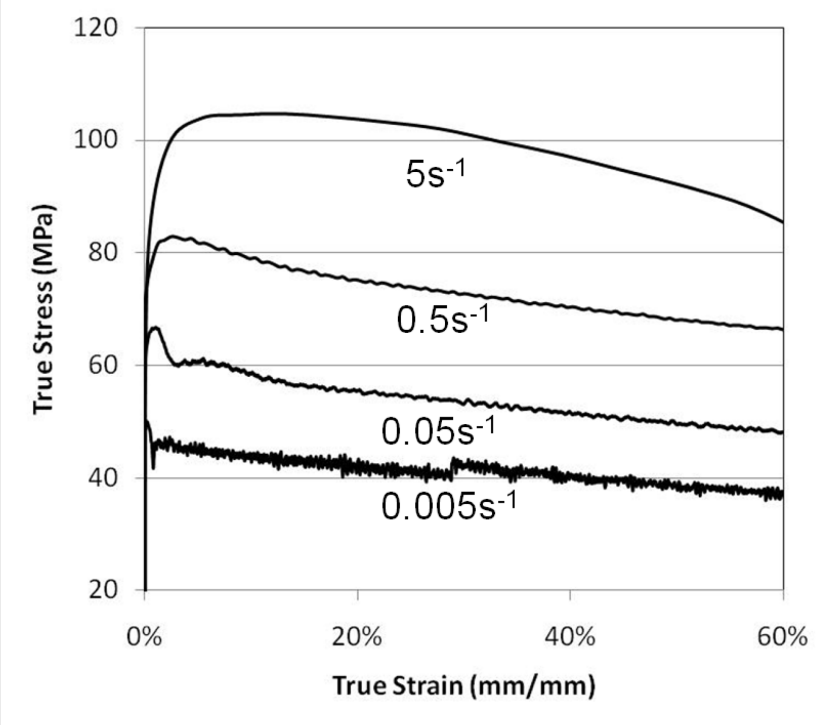

Figure A-12 – True compressive stress/strain curves completed at 425°C for P/M 2324 + 5v/o SiC.

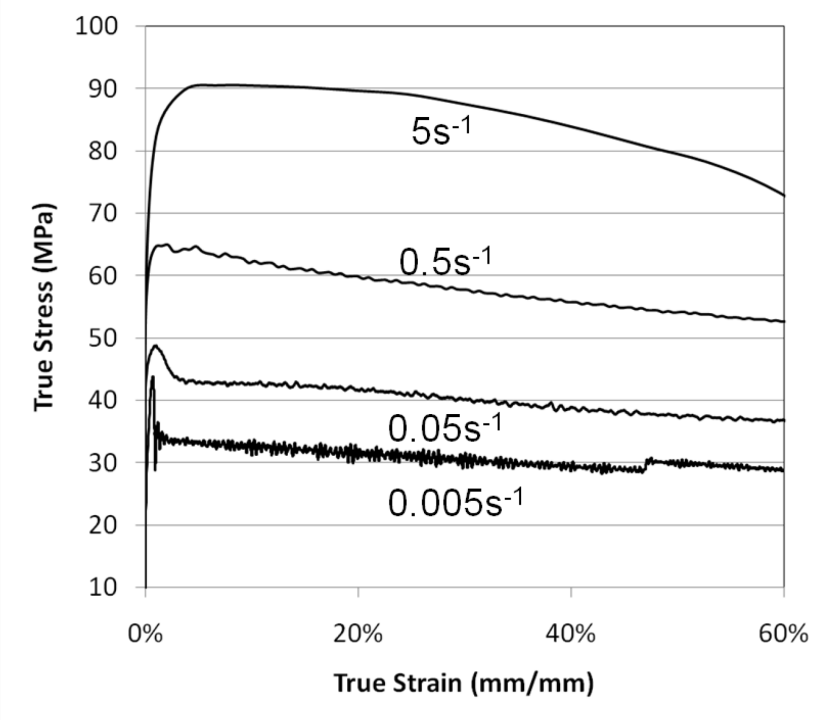

Figure A-13 – True compressive stress/strain curves completed at 450°C for P/M 2324 + 5v/o SiC.

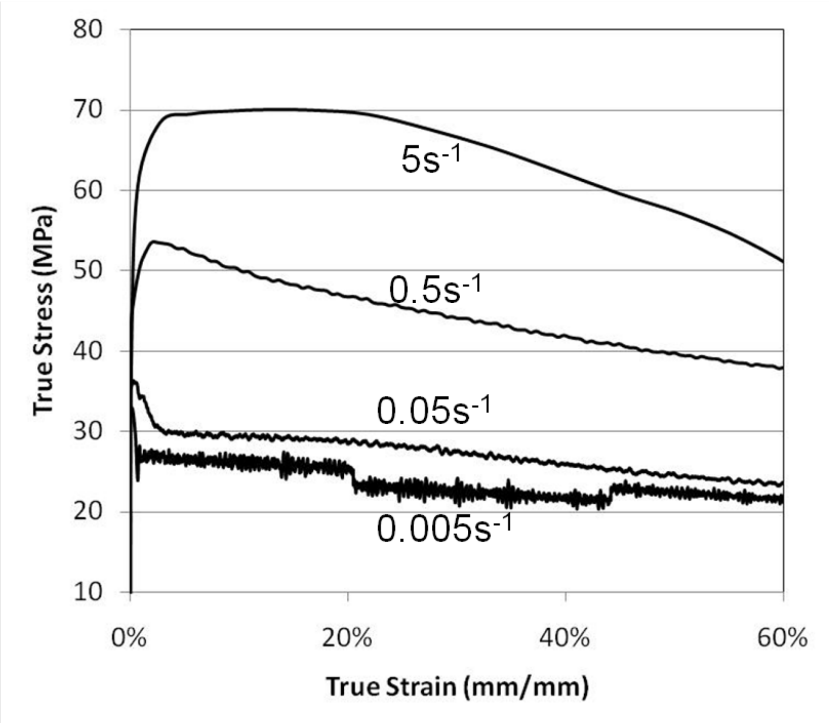

Figure A-14 – True compressive stress/strain curves completed at 475°C for P/M 2324 + 5v/o SiC.

Appendix B: Tensile Property Measurements

This section contains additional information on the tensile properties of P/M 2324, P/M2324+5%SiC and AA2024, including UTS, yield strength, percent elongation, and young's modulus for all the tensile tests and the averages and standard deviations.

Table B-1– Tensile results for AA2024 T6, P/M 2324 T6, P/M 2324+5%SiC T6, P/M 2324 Swaged T6, and P/M 2324+5%SiC Swaged T6.

Alloy	Sample	UTS (MPa)	YS (MPa)	Elongation (%)	Young's Modulus (E)
AA2024 T6	1	418	327	11.1	74
AA2024 T6	2	411	323	10.1	69
AA2024 T6	3	412	321	11.8	67
AA2024 T6	4	428	337	9.6	70
Average		417	327	10.7	70
Stdev		8.0	7.0	1.0	2.8
2324 Sintered T6	1	366	311	2.7	61
2324 Sintered T6	2	322	287	1.7	74
2324 Sintered T6	3	328	291	1.4	64
Average		339	296	2.0	66
Stdev		23.7	12.9	0.7	6.9
2324 Swaged T6	1	458	393	6.1	74
2324 Swaged T6	2	437	383	4.0	72
2324 Swaged T6	3	446	382	5.7	71
2324 Swaged T6	4	452	386	6.5	73
Average		448	386	5.6	72
Stdev		9.0	5.1	1.1	1.5
2324+5 v/o SiC Sintered T6	1	382	342	1.0	90
2324+5 v/o SiC Sintered T6	2	387	365	0.9	78
2324+5 v/o SiC Sintered T6	3	396	362	1.2	74
2324+5 v/o SiC Sintered T6	4	390	355	1.2	84
2324+5 v/o SiC Sintered T6	5	366	345	0.8	79
Average		384	354	1.0	81
Stdev		11.1	10.1	0.2	6.2
2324+5 v/o SiC Swaged T6	1	462	382	4.6	94
2324+5 v/o SiC Swaged T6	2	455	383	4.8	79
2324+5 v/o SiC Swaged T6	3	462	387	4.5	72
2324+5 v/o SiC Swaged T6	4	469	394	4.5	88
Average		462	387	4.6	83
Stdev		5.7	5.7	0.1	9.7